Oil & Natural Gas Technology

DOE Award No.: DE-FE0001243

Clean and Secure Energy from Domestic Oil Shale and Oil Sands Resources

Quarterly Progress Report (July - September 2012)

Submitted by:
University of Utah
Institute for Clean and Secure Energy
155 South 1452 East, Room 380
Salt Lake City, Utah 84112

Prepared for:
United States Department of Energy
National Energy Technology Laboratory

November 13, 2012

Office of Fossil Energy

Clean and Secure Energy from Domestic Oil Shale and Oil Sands Resources

DOE Award No.: DE-FE0001243

Quarterly Progress Report

July 2012 to September 2012

Submitted by:
Institute for Clean and Secure Energy
155 S. 1452 E. Room 380
Salt Lake City, UT 84112

Principal Investigator: Philip J. Smith
Project Period: October 1, 2010 to September 30, 2013

Prepared for:
U.S. Department of Energy
National Energy Technology Laboratory

Acknowledgment: "This material is based upon work supported by the Department of Energy under Award Number DE-FE0001243."

EXECUTIVE SUMMARY

The Clean and Secure Energy from Domestic Oil Shale and Oil Sands Resources program is part of the research agenda of the Institute for Clean and Secure Energy (ICSE) at the University of Utah. In its outreach efforts this quarter, ICSE finalized materials for a short course on kerogen liquefaction (e.g. oil shale thermal treatment) to Statoil in Trondheim, Norway, on October 8-10, 2012.

In Task 3.0, the Subtask 3.1 team gathered data related to fuel consumption associated with well drilling in the Uinta Basin. The data will be used to estimate costs and greenhouse gases associated with well drilling. A preliminary report was completed by Subtask 3.2 researchers and is included as an appendix to this report. For Subtasks 3.3 and 3.4, the project team is developing an overall framework for a Matlab-based systems dynamics model with the objective of predicting drilling frequency and production levels from oil and gas wells in the Uinta Basin given the forecast price for oil and gas, the marginal cost of producing, and other constraints such as the availability of permits, transportation, etc.

The Task 4.0 projects focused on the Skyline 16 core (GR-1, GR-2, and GR-3) are synthesizing the data collected into a publication. Subtask 4.9 researchers are leading this effort. Subtask 4.3 researchers completed two project milestones related to analysis of products from Skyline 16 core samples and demineralized kerogen pyrolysis. The Subtask 4.7 team completed the first mechanical properties tests on White River oil shale samples. The testing included unconfined compression at ambient temperatures and thermal conductivity measurements. Tests on Skyline 16 core samples will follow. Subtask 4.9 researchers completed the final experimental work on this project, solution NMR on the tar sample from the pyrolysis of the GR-3 kerogen and solid state NMR on several additional chars from the GR-3 sample. The small angle X-ray scattering and the atomic pairwise distribution function data is currently being analyzed.

In other Task 4.0 projects, the Subtask 4.1 team continues to develop their Star-CCM+ simulation tool with the addition of a properties model that accounts for spatial and temperature variability in density, thermal conductivity, and specific heat of oil shale at large (formation) or small (piece of shale) scales. The graduate student working on Subtask 4.2 (reservoir simulation) has accepted a position at Los Alamos National Laboratory and is working with the project PI to complete the final report. Researchers in Subtask 4.8 will be describing their last two cores in the next quarter.

In the area of policy and legal analysis, Subtask 5.3 researchers performed the foundational research on the legal and policy framework for utilizing simulation science in the context of assessing environmental risks or harms. The final report for Subtask 6.2 will be submitted next quarter.

The Market Assessment (Subtask 6.3) was finalized in this quarter in preparation for sending it out to reviewers in October 2012. Subtask 6.1, which provided much of the engineering analysis for the assessment, will be completed once the process models and data have been uploaded to a webpage on the ICSE website.

All Task 7.0 projects were reviewed by a team from American Shale Oil (AMSO), Genie Energy, and TOTAL at a meeting in late September. Based on feedback from this meeting, Subtask 7.2 will be discontinued and its funds reallocated to Subtasks 7.1 and 7.3. The Subtask 7.1 team continued its development of methods for representing the matrix of experimental data that has been generated by AMSO. Additional data from Metarock triaxial testing has been fitted. The Subtask 7.3 team improved the computational representation of the AMSO process in their simulations and created a simulation tool that accounts for the depth- and temperature-varying properties of oil shale in the AMSO test bed.

PROGRESS, RESULTS, AND DISCUSSION

Task 1.0 - Project Management and Planning

During this quarter, there were no schedule/cost variances or other situations requiring updating/amending of the Project Management Plan (PMP). A no cost time extension will be submitted in the next quarter which, if accepted, will require updating the PMP.

Task 2.0 -Technology Transfer and Outreach

Task 2.0 focuses on outreach and education efforts and the implementation of External Advisory Board (EAB) recommendations. The next EAB meeting would likely not be held until the first quarter of 2013. Other industrial interactions this quarter include (1) the finalization of a short course to be given by Professors Philip Smith, John McLennan, Milind Deo (all of the University of Utah), and Tom Fletcher (Brigham Young University) to a team of Statoil employees in Trondheim, Norway, on October 8-10, 2012 and (2) a review of the Strategic Alliance Reserve program (see Task 7.0) by American Shale Oil, Total, and Genie.

Work was completed this quarter on the Marriott Library's ICSE Collection, and all documents missing from the initial document migration from ICSE's DSpace repository to the Marriott's ICSE Collection have been identified. Additionally, a submission framework for future ICSE reports and documents has been developed and agreed to with the Marriott Library. Efforts have begun to add the missing documents, as well as newly collected ICSE documents, to the Marriott Library's ICSE Collection, such that all ICSE scholarship and supporting research documents are maintained in a single collection. Work on this task has been slower than anticipated, but Task 2.0 researchers anticipate that these efforts will be completed next quarter.

Task 3.0 - Clean Oil Shale and Oil Sands Utilization with CO_2 Management

The Subtask 3.0 team made the decision to develop a system dynamics model in Matlab rather than continue code development on the AnyLogic platform. This decision was made for several reasons: (1) Familiarity of team members with coding in Matlab, (2) Matlab code can be more easily linked to existing tools for validation/uncertainty quantification, and (3) the cost of upgrading AnyLogic licenses is prohibitive.

Subtask 3.1 (Phase I) – Macroscale CO_2 Analysis (PI: Kerry Kelly, David Pershing)

The completion of the Phase I deliverable will be delayed until November 2012. In September, the Subtask 3.1 team received updated assessment results (Subtask 6.3) for in situ and ex situ development scenarios of Utah oil sands and oil shale. Based on these results, team members performed supplemental analyses to yield carbon footprints for each of the scenarios. Figure 1 shows the well-to-pump greenhouse gas (GHG) footprints for the ex situ oil shale, ex situ oil sands, and in situ oil shale scenarios without the use of oxyfiring for CO_2 capture and compares these to literature values. The Utah ex situ oil sands GHG emissions are in the same range as those reported for ex situ production of Canadian oil sands (McKellar et al., 2009), but the in situ oil shale numbers are higher than other reported values (Brandt, 2008). The team is currently ensuring that the reasons behind these differences are understood and is refining these estimates based on feedback from reviewers on the assessment results. During the upcoming quarter, they plan to finalize the GHG footprint analysis and accompanying publication.

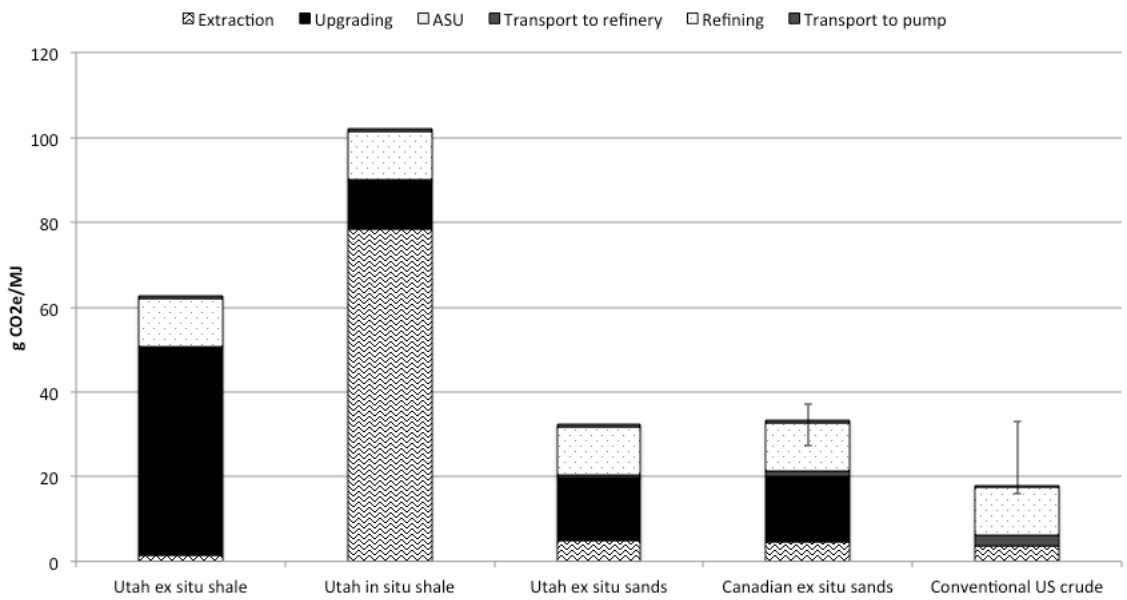

Figure 1: Comparison of well-to-pump GHG emissions for production of gasoline from in situ and ex situ production of Utah oil shale, ex situ production of Utah and Canadian oil sands (ANL, 2012), and conventional crude oil (EPA, 2009). The error bars on the Canadian ex situ sands show the range of values reported in McKellar et al. (2009) while those for conventional US crude show the range of values reported by the US Department of Energy (2009).

Subtask 3.1 (Phase II) – Lifecycle Greenhouse Gas Analysis of Conventional Oil and Gas Development in the Uinta Basin (PI: Kerry Kelly, David Pershing)

During this quarter, the Subtask 3.1 team gathered data related to fuel consumption associated with well drilling in the Uinta Basin. The fuel-consumption information will be used to estimate GHG associated with well drilling and by the rest of the team to estimate costs. The team has also continued to monitor several potentially useful sources for validation data of GHG emissions. Their release has been delayed but is expected in the coming months, including the Bureau of Land Management's air emissions inventory and the Uinta Basin air emissions inventory update being developed by Utah State University.

The investigators collected fuel-consumption data for 303 wells from three companies who drilled in the Uinta Basin and provided fuel-consumption data as part of their well-drilling reports. These companies include Berry Petroleum (83 wells in Brundage Canyon), EOG Resources (153 wells in Natural Buttes), and Gasco (67 wells in Natural Buttes). Figure 2 suggests a positive correlation between fuel consumption and depth. From the available data, fuel consumption can be represented by the following relationship:

$$Fuel\_consumption = 1.00026513(1.00027178)^{Depth} \quad (1)$$

This relationship is more likely to represent fuel consumption in the Uinta Basin than the average of 1.5 gal/ft drilled used in other studies (Advanced Resources, Int., 2008). Team members also determined that they did not have sufficient data to identify the effects of drilling direction (horizontal, directional, or vertical) on fuel consumption.

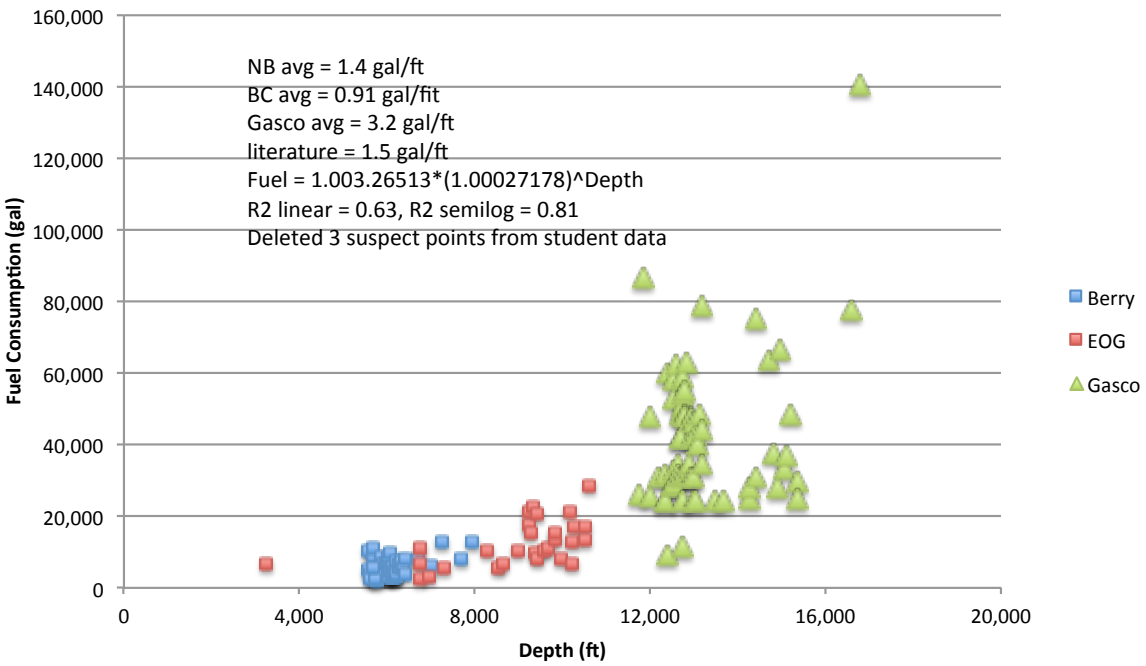

Figure 2: Fuel consumption vs. depth for 303 wells in the Uinta Basin. The data includes Berry Petroleum (83 wells in Brundage Canyon), EOG Resources (153 wells in Natural Buttes), and Gasco (53 wells in Natural Buttes).

Finally, researchers investigated the number of days versus fuel consumption (Figure 3) and identified a positive linear correlation ($R^2 = 0.9$). It is likely that the fuel-consumption vs. depth relationship will be more useful to the other researchers in Task 3. During the coming quarter, they plan to look for additional data at well depths greater than 16,000 feet to determine if the high fuel consumption data point in Figure 2 is an anomaly or is typical of that well depth.

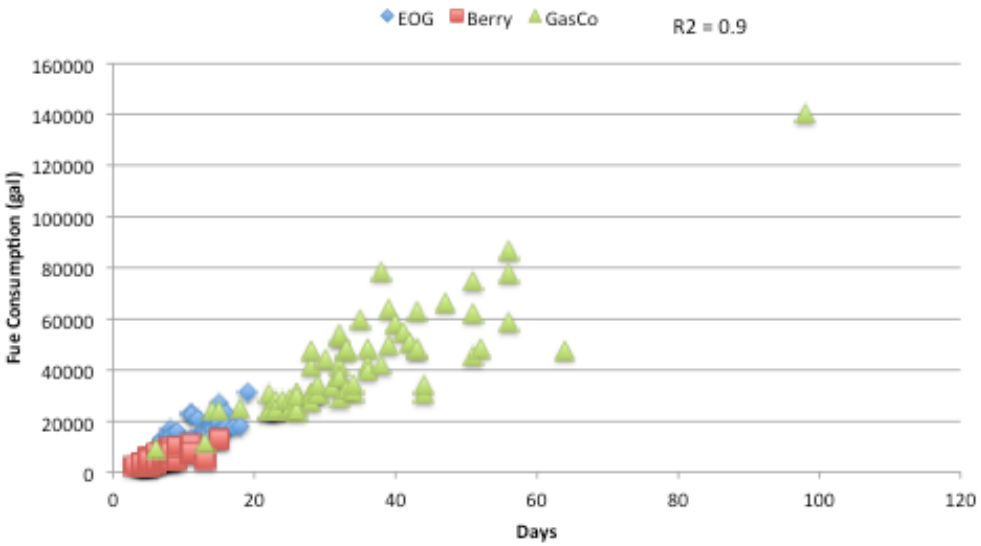

Figure 3: Fuel-consumption vs. drilling days.

Subtask 3.2 - Flameless Oxy-gas Process Heaters for Efficient CO_2 Capture (PI: Jennifer Spinti)

The Subtask 3.2 team has prepared a preliminary report detailing results of a skeletal validation analysis of the IFRF's oxy-gas experiments (Coraggio and Laiola, 2009). The report is attached as Appendix A.

Subtask 3.3 - Development of Oil and Gas Production Modules for $CLEAR_{uff}$ (PI: Terry Ring)

The project team has focused its efforts on translating the $CLEAR_{uff}$ model developed on the AnyLogic platform into MatLab code so that it can be more flexibly manipulated. Additionally, Subtask 3.3 members have initiated efforts to build consensus within all of Task 3.0 as to the overall framework for the model. The objective of the model will be to predict how many oil and gas wells are drilled in a given year and the production from those wells based on the historical decline curves for various fields in the Uinta Basin, the forecast price for oil and gas, the marginal cost of producing, and other constraints such as the availability of permits, transportation, etc. and then compare that predicted number to how many were actually drilled for Subtask 3.4. It is thought that this approach most closely parallels unconventional fuel development where various system constraints coupled with projected revenues and costs will determine which projects move forward.

Subtask 3.4 - V/UQ Analysis of Basin Scale $CLEAR_{uff}$ Assessment Tool (PI: Jennifer Spinti)

The systems-based approach for the model is pictorially developed in Figure 4. It shows the major components of the MatLab model and how the model will be used for validation and uncertainty quantification. The well cost and forecast price coupled with system constraints determine the number of wells drilled as a function of time. Each well is then drilled, fracked, and completed. These completed wells are hooked to pipelines, localized product storage, or gathering plants. Decline curves for oil, gas and natural gas liquids (NGLs) are applied to each well that is drilled to obtain per well production as a function of time. Aggregated production from the Basin will be used for validation and uncertainty quantification using historical production data obtained from Utah's Division of Oil, Gas, and Mining. Another aspect of the proposed model is that it will predict the various emissions produced in aggregate for the oil and gas developments in the basin.

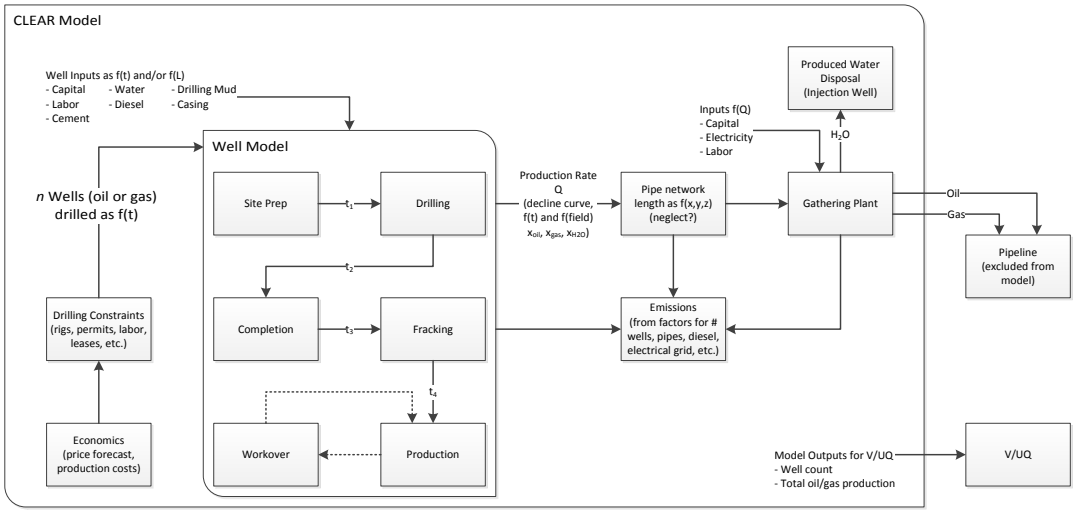

Figure 4: CLEAR model overview.

Task 4.0 - Liquid Fuel Production by In-situ Thermal Processing of Oil Shale/Sands

Subtask 4.1 (Phase II) - Development of CFD-based Simulation Tools for In-situ Thermal Processing of Oil Shale/Sands (PI: Philip Smith)

The project team is using the commercial software Star-CCM+ to develop a high performance computing (HPC) computational fluid dynamics (CFD)-based simulation tool to study thermal heating of oil shale inside the ECOSHALE capsule developed by Red Leaf Resources. In the past quarter they have continued to increase the fidelity of the simulation tool by incorporating properties of oil shale that are both temperature and spatially/directionally dependent.

In the previous quarter, team members began analyzing preliminary results from their implementation of a kerogen conversion model in Star-CCM+. They described difficulties in replicating published studies in terms of exact boundary conditions, which have a significant effect on simulation results. Another important parameter in accurately predicting oil yield is the temperature distribution of individual pieces of shale, not just the temperature distribution in the fluid phase of the capsule. Therefore, work this quarter was focused on incorporating models which account for spatial variability and temperature dependence inside pieces of oil shale.

Star-CCM+ has some built-in capabilities to prescribe property variations due to temperature but has limited options for prescribing properties based on spatial variability. To implement spatial variation and couple it with temperature dependence required the project team to explore User Code capabilities of Star-CCM+. Star-CCM+ allows coupling of user coded subroutines with the main solver. While this coupling is not as efficient or capable as built-in options, it does allow for extending the capabilities of Star-CCM+.

Team members have created a suite of user codes that include both temperature and spatial variations for density, specific heat, and thermal conductivity. These additions required slight modification of the solution quantities solved by Star-CCM+. Star-CCM+, by default, allows for property variations in density and thermal conductivity but is rather prohibitive in specific heat property variations. To implement the variability in specific heat, the project team lumped the properties into density and prescribed a value of unity to the specific heat property. This change was possible due to the way Star-CCM+ solves the solid conduction equation:

$$\frac{d}{dt}\int_V \rho C_p T dV + \oint_A \rho C_p T \mathbf{v}_s \cdot d\mathbf{a} = -\oint_A \mathbf{q}'' \cdot d\mathbf{a} + \int_V s dV \quad (2)$$

In Equation (2), both density, ρ, and specific heat, c_p, are always grouped together. Therefore, using the User Code capability, the project team prescribed the spatial and temperature dependence of the product of density and specific heat into the density term and assigned a value of one to the actual specific heat property inside the Star-CCM+ solver settings.

The results from employing this technique can be seen in Figure 5. Each color represents a different layer inside a single piece of oil shale. This figure shows arbitrary spatial variability to test the feasibility of the team's approach for a realistic scenario. The edges of Figure 4 appear somewhat smeared because of the increased size of the computational cells toward the edges of the piece of shale.

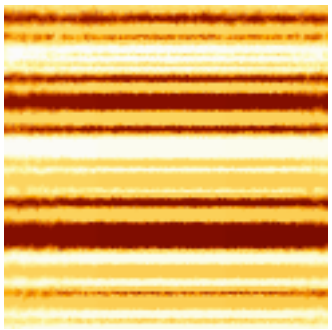

Figure 5: Layers representing spatial and temperature variability of properties for a single piece of oil shale.

This technique of spatial and temperature dependence can be extrapolated to a larger domain representing and entire shale formation, such as the one for the capstone project, Subtask 7.3.

Subtask 4.2 - Reservoir Simulation of Reactive Transport Processes (PI: Milind Deo)

The graduate student working on the Subtask 4.2 team finished up his thesis and left the university to accept a position at a national laboratory. The project's PI, Professor Milind Deo, is working with this former student to write a topical report, which is the final deliverable for this project.

Subtask 4.3 – Multiscale Thermal Processes (PI: Milind Deo, Eric Eddings)

Two project milestones were completed during this quarter as reported below: (1) complete core sample pyrolysis at various pressures and analyze product bulk properties and composition and (2) collect and analyze condensable pyrolysis products from demineralized kerogen.

1. Completed the high pressure TGA pyrolysis experiments.
2. Repaired and calibrated the GC/MS machine.
3. Analyzed tars from samples 1.9, 2.9 and 3.9 using the GC/MS.
4. Analyzed the methane, carbon dioxide and carbon monoxide components of the light gas effluent.

Pyrolysis Kinetics (Milestone 1)

All pressurized and atmospheric thermogravimetric analysis (TGA) experiments on the three Green River pulverized oil shale samples were completed, despite several delays with the higher pressure runs due to malfunctions of the electronic balance. These samples had a mass mean diameter of 60 µm. The kinetic coefficients from all TGA experiments were determined for both the first-order model and the distributed activation energy model. Figure 6 shows sample TGA data along with the corresponding curve fits for a sample at 5 K/min at both atmospheric pressure and 40 bar. The kinetic coefficients were determined by fitting data from three heating rates (1, 5, and 10 K/min). Table 1 shows the resulting kinetic coefficients from this study for all three GR samples.

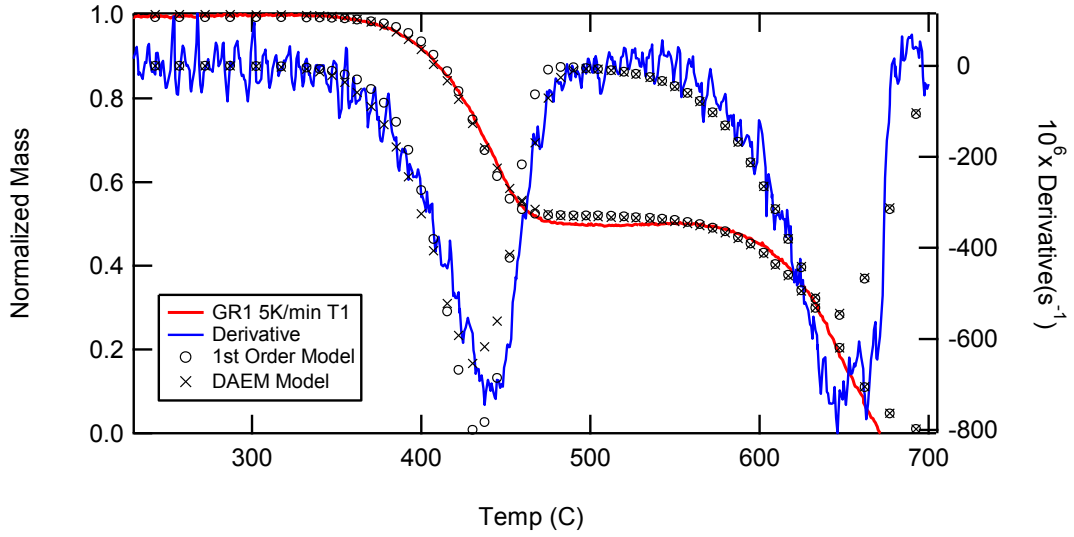

(a) Atmospheric pressure

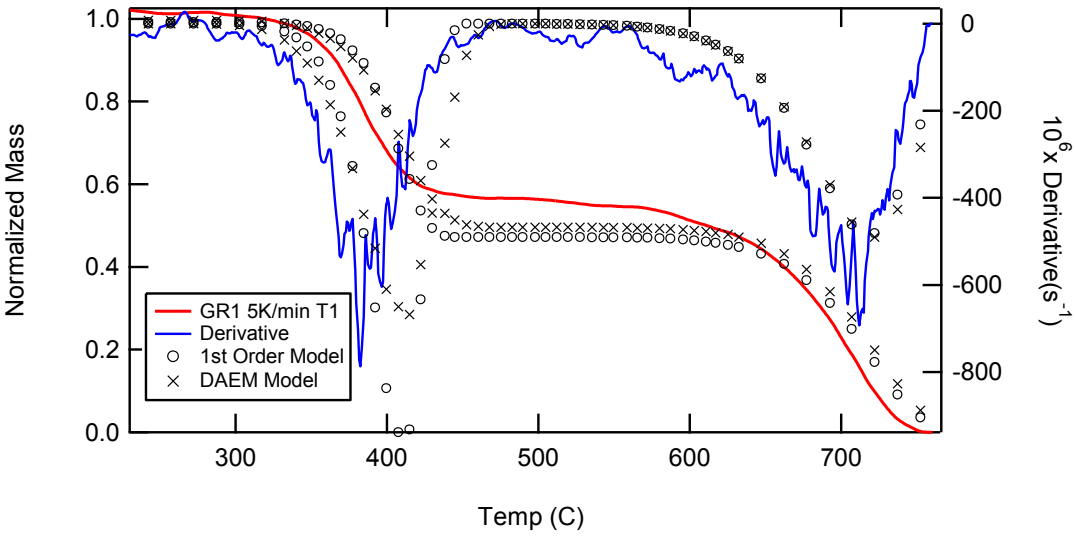

(b) 40 bar

Figure 6: TGA pyrolysis data and best-fit model calculations for GR-1 oil shale crushed and sieved to 60 µm mass mean diameter, heated at 5 K/min.

Table 1. Kinetic coefficients determined from TGA pyrolysis of GR oil shale samples.

Sample		First-Order		DAEM	
		1 atm	40 bar	1atm	40 bar
GR1	A (1/s)	8.90E+13	2.80E+14	9.20E+13	1.00E+14
	E (kJ/mol)	221	219	223	215
	σ (kJ)	--	--	4	2.6
GR2	A (1/s)	4.50E+13	8.00E+13	2.60E+14	3.00E+14
	E (kJ/mol)	216.9	210	228.1	219.4
	σ (kJ)	--	--	2.6	6.7
GR3	A (1/s)	9.50E+13	1.50E+14	9.40E+13	3.50E+14
	E (kJ/mol)	220	217	222	225
	σ (kJ)	--	--	4.6	5.3

The kinetic coefficients shown in Table 1 indicate that the activation energy of all three samples is approximately 220 kJ/mol, and the increase with elevated temperature is only about 3 kJ/mol. This result indicates a negligible effect of pressure on the pyrolysis kinetics.

Tar/Char Analysis (Milestone 2)

Tars gathered from previously performed retort pyrolysis experiments on demineralized kerogen were dissolved in minimal amounts of dimethyl chloride in preparation for analysis in the gas chromatograph/mass spectrometer (GC/MS). Each tar corresponded to a specific sample at a specific temperature in the reaction. For example, the GR-2.9 tar had samples gathered at 425°, 445°, 475°, 480°, 525°, and 575°C. Each of these tars was run three times through the GC/MS, allowing the identification of the major components of the tar at each temperature. The results are displayed in Figure 7 and Table 2, which together show the identity and relative concentrations of the components of the tar samples at each temperature.

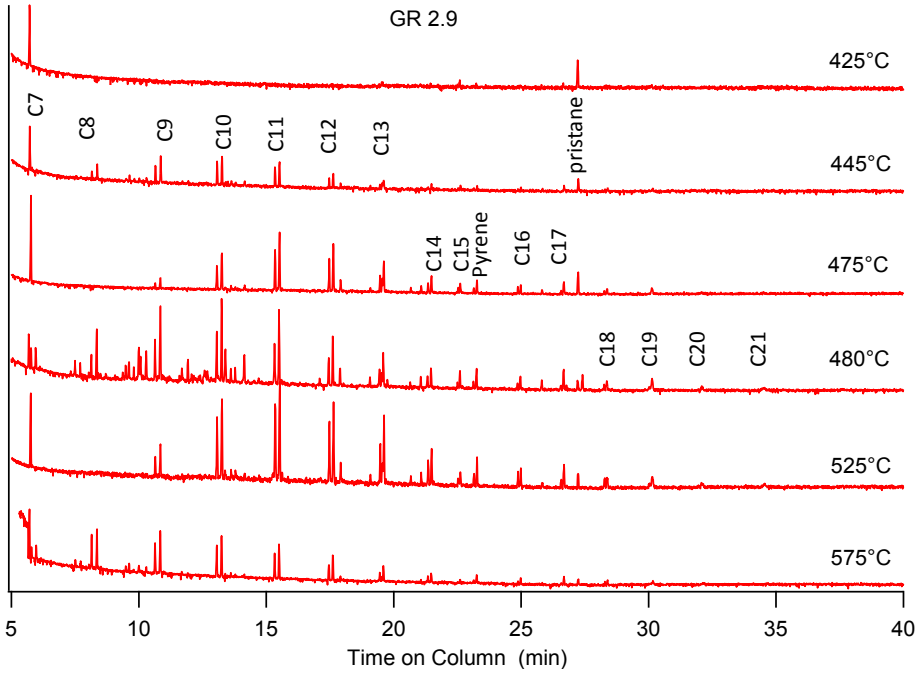

Figure 7: Gas chromatography chart showing the relative composition of the tars at each temperature (for which compounds correspond to which temperatures, see Table 2).

Table 2. List of compounds detected in tars from kerogen pyrolysis using GC/MS, along with the time of the GC peak.

Time (min)	Compound	Time (min)	Compound
5.78	1-Heptene	21.7	Tetradecane
5.96	Heptane	22.84	2-Pentadecanone
8.21	1-Octene	23.41	1-Pentadecene
8.41	Octane	23.53	Pentadecane
10.71	1-Nonene	24.61	Pyrene
10.92	Nonane	25.19	1-Hexadecene
13.15	1-Decene	25.3	Hexadecane
13.35	Decane	26.12	2-Heptadecanone
15.47	1-Undecene	26.93	1-Heptadecene
15.63	Undecane	27.04	Heptadecane
17.61	1-Dodecene	27.58	Pristane
17.77	Dodecane	28.67	1-Octadecene
18.05	2-Tridecanol	28.79	Octadecane
19.22	Dodecanone	30.62	Nonadecane
19.65	1-Tridencene	32.64	Eicosane
19.72	2-Tridecanone	35.25	Heneicosane
19.79	Tridecane	38.39	Docosane
21.32	2-Tetradecanone	42.68	Tricosane
21.57	1-Tetradecene	48.4	Tetracosane

Light Gas Analysis (Milestone 2)

The light gas effluent of the kerogen retort experiments was quantitatively analyzed to find the concentration of the major components, namely methane (CH_4), carbon dioxide (CO_2) and carbon monoxide (CO). This was done by comparing the peak areas for each of these compounds in Fourier transform infrared (FTIR) spectrums of known reference gases and in the FTIR spectra of collected unknown gases. This analysis yielded the concentrations of CH_4, CO_2 and CO over the range of pyrolysis reaction temperatures. Figure 8 shows the gas analysis for two different samples, separated by the temperature achieved in the kerogen retort. Substantial amounts of CO_2 were released early. Possible "other" gases include hydrogen and light hydrocarbons.

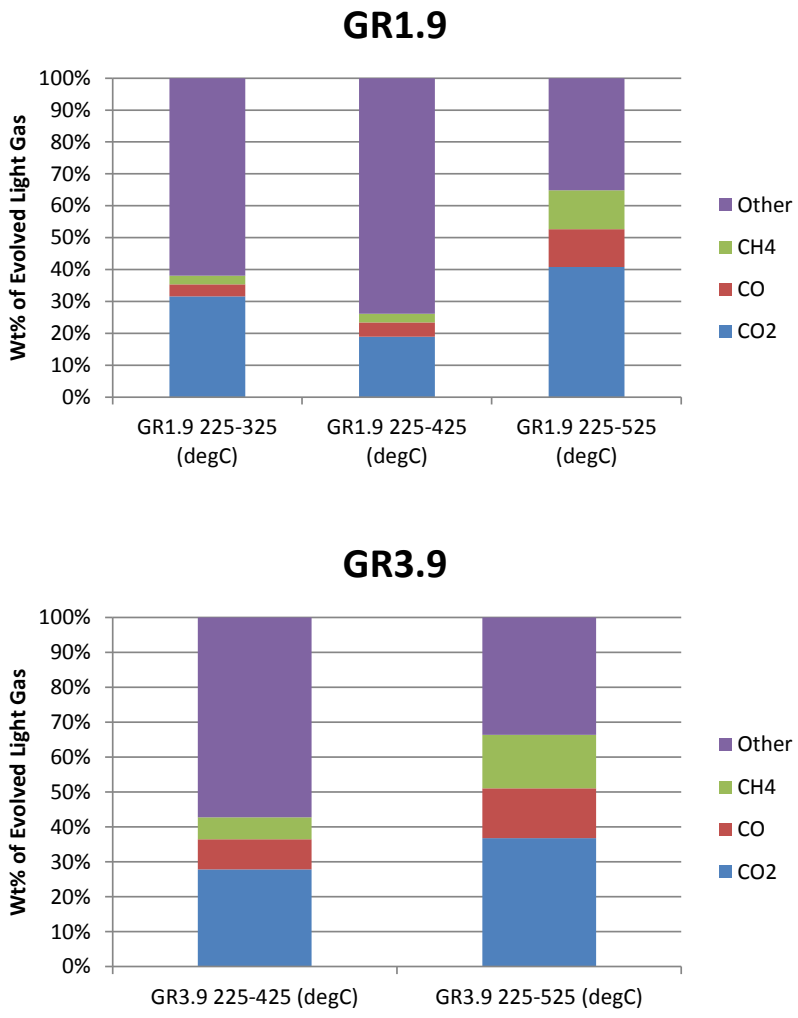

Figure 8: The composition of the light gas effluent from the kerogen retort, measured by FTIR analysis.

Subtask 4.4 - Effect of Oil Shale Processing on Water Compositions (PI: Milind Deo)

This project has been completed.

Subtask 4.5 - In Situ Pore Physics (PI: Jan Miller, Chen-Luh Lin)

The Subtask 4.5 team is still waiting on samples from Subtask 4.7 to complete one milestone and one deliverable. It is proposed the milestone and the final deliverable (listed below) be completed by December 31, 2012.

- Complete pore network structures & permeability calculations of Skyline 16 core directional/anisotropic, mineral zones) for various loading conditions, pyrolysis temperatures, & heating rates
- Topical report summarizing results of pore network structures & permeability calculations on Skyline 16 cores

Subtask 4.6 - Atomistic Modeling of Oil Shale Kerogens and Oil Sand Asphaltenes (PI: Julio Facelli)

The project team has completed their final deliverable for this project, a paper on kerogen modeling entitled “Three-Dimensional Structure of the Siskin Green River Oil Shale Kerogen Model: A Comparison Between Calculated and Observed Properties.” The paper has been submitted to Energy & Fuels. A copy of the submitted manuscript was previously sent to R. Vagnetti but is also attached to this report as Appendix B.

Subtask 4.7 - Geomechanical Reservoir State (PI: John McLennan)

The milestone to complete the experimental matrix is again delayed. A new completion date of December 31, 2012, has been proposed. The Subtask 4.7 team is completing the first mechanical properties tests on White River oil shale samples prepared by the Utah Geological Survey’s core laboratory. The purpose of these tests is two-fold: (1) debugging and calibration of experimental equipment and (2) generation of reliable data. Thermal conductivity measurements are also being made and are described below.

Mechanical Properties

The complete testing fixture (using the hydraulic jack for the four-inch diameter samples) is shown in Figure 9. The team is using a smaller jack, has added radial LVDTs, and is finalizing the separation system. The testing is unconfined compression at ambient temperatures. The tests are being run outside of the pressure vessel that was described in the previous quarterly report. All that is required is resistance to axial movement of the jack so that an axial load could be transferred to the sample. This resistance is provided by a structural loading frame in the Civil Engineering Department at the University of Utah. The nominal (subject to change) testing matrix is shown in Table 3.

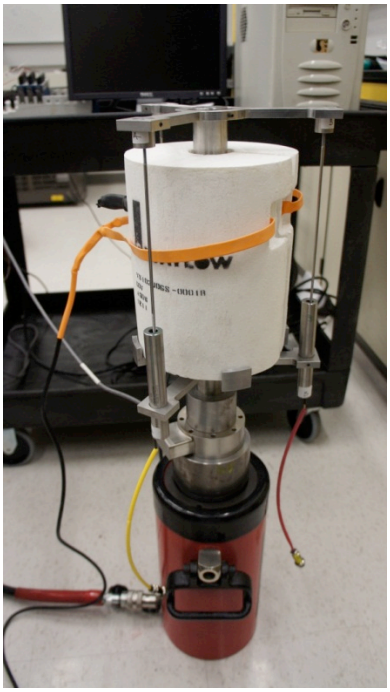

Figure 9: Complete sample configuration for shakedown testing.

Table 3. Revised test matrix

Test	Temperature (°C)	Confining Pressure (psi)	Comments
1	Ambient	0	Designed to determine any design modifications required, to ensure calibration of LVDTs and load cell (both already independently calibrated and to generate information on a White River oil shale sample. Measure the yield and other properties independently.
2	50	0	Duplication of AMSO testing on a White River oil shale sample, at a low temperature. Hook up the nitrogen lines to flow through the sample although no effluent is expected.
3	100	0	Idem. A separation system is being fabricated. This will be connected and debugged. We need to determine if there needs to be an external Plexiglas collection system purged with nitrogen around the sample.
4	200	0	Idem
5	400	0	Idem – precise temperature to be determined.
6	400	0	Idem - Using Skyline 16 parallel to bedding sample
7	400	0	Idem - Using Skyline 16 perpendicular to bedding sample
8			TBD – could be creep testing
9			TBD – could be undrained testing

Figures 10 and 11 are stress-strain data from the first oil shale sample tested.

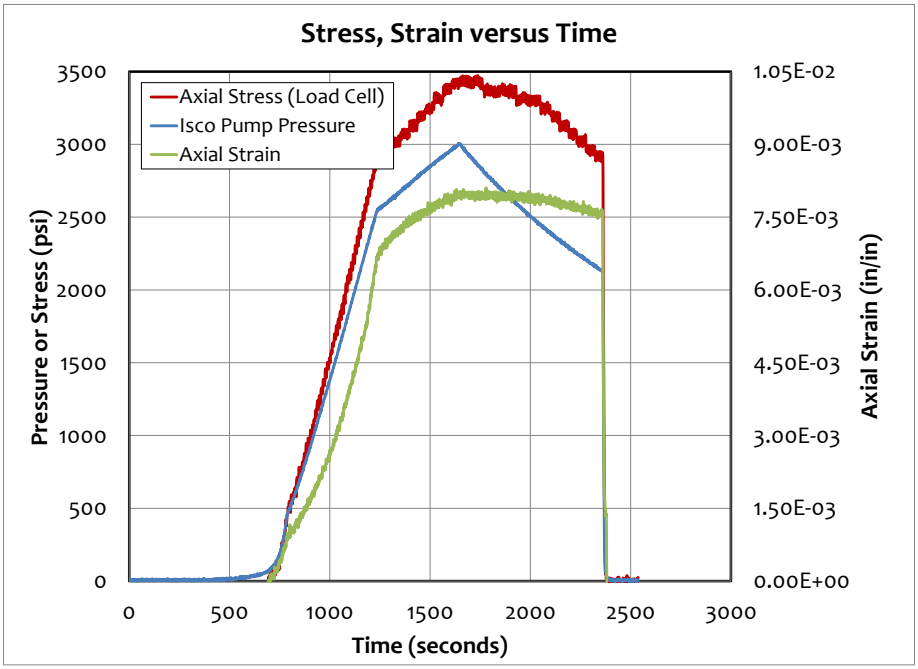

Figure 10: Stress-strain data acquired in testing the first sample. The sample was not failed; the variations in modulus are reflections of changing the axial stress rate and unloading.

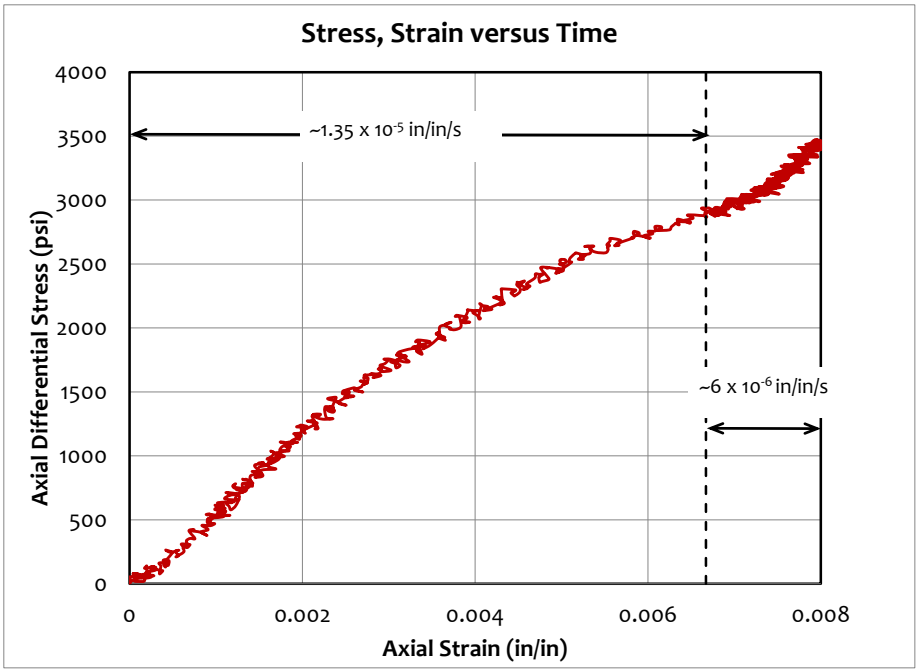

Figure 11: Stress-strain data acquired in testing the first sample. The sample was not failed; the variations in modulus are reflections of changing the axial stress rate and unloading.

After the unconfined measurements are completed (axial stress only), measurements at confining pressure will be performed using the pressure vessel shown in Figure 12.

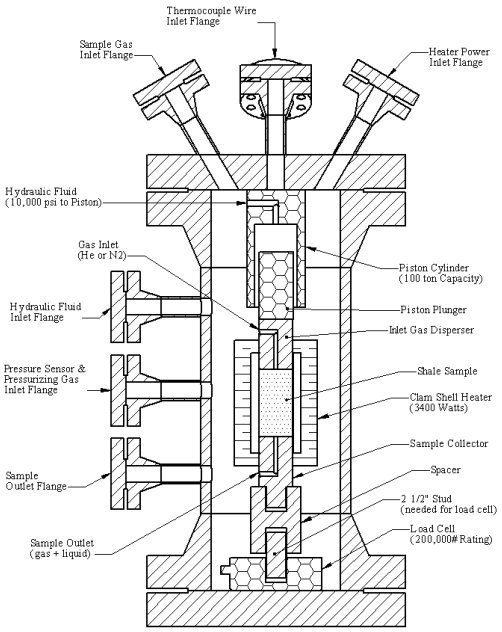

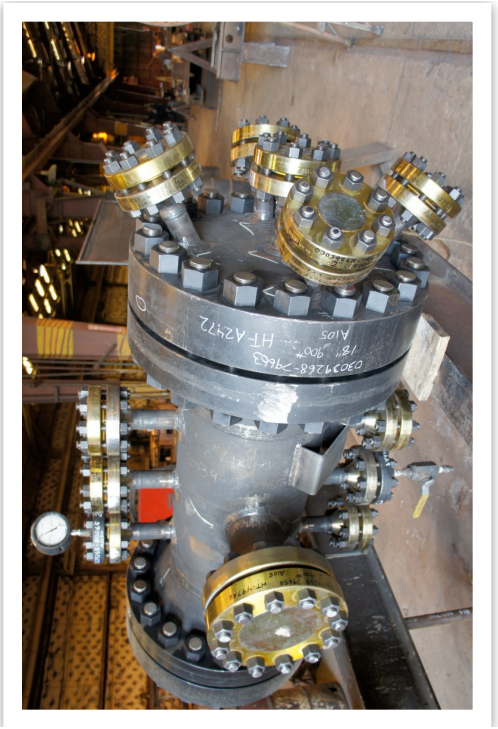

Figure 12: Schematic cross-sectional view and photograph of pressure vessel to be used for applying confining pressure.

Thermal Conductivity

In order to understand the thermal conductivity of the samples and to resolve convection issues between the heater and the sample, baseline tests have been carried out on a sample with a thermocouple installed in a concentrically-drilled hole. Typical data are shown in Figure 13.

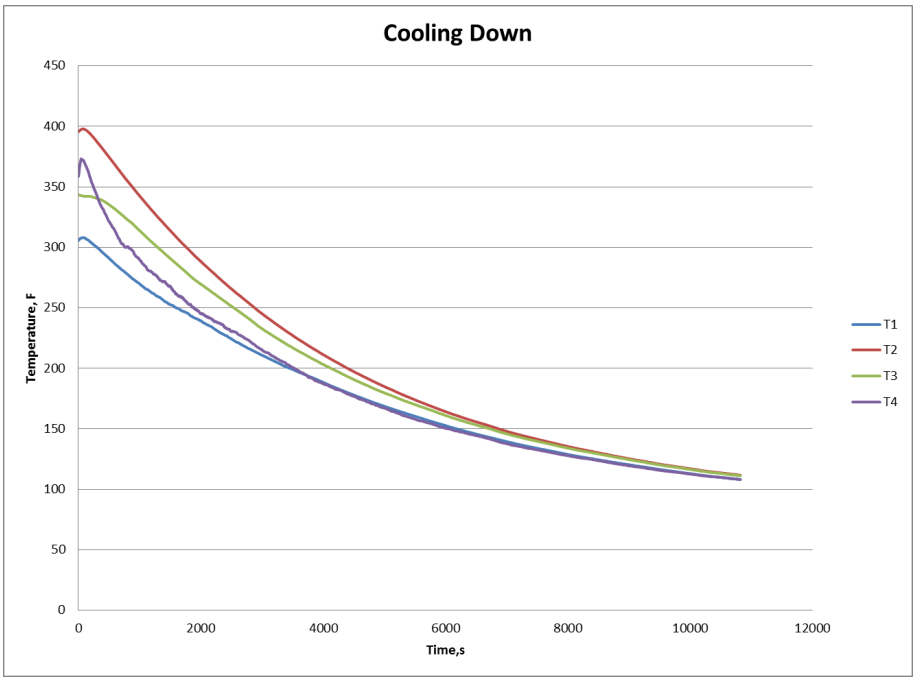

Figure 13: Behavior of thermocouples (thermocouple controlling the heater, the thermocouple in the drilled hole in the center of the oil shale sample and two thermocouples in the annular space between the sample and the heater) during cooling of a sample. Convection issues are being dealt with and these data will be interpreted for thermal conductivity assessments.

Subtask 4.8 - Developing a Predictive Geologic Model of the Green River Oil Shale, Uinta Basin (PI: Lauren Birgenheier)

Subtask 4.8 researchers presented a poster at the American Association of Petroleum Geologists - Rocky Mountain Section meeting in September. They have plans to describe the last two cores for their north-south cross section in the next quarter.

Subtask 4.9 - Experimental Characterization of Oil Shales and Kerogens (PI: Julio Facelli)

The final experimental work on this project was completed at the start of this quarter, specifically the solution nuclear magnetic resonance (NMR) spectroscopy on the tar sample from the pyrolysis of the GR-3 kerogen and solid state NMR on several additional chars from the GR-3 sample. The data from these NMR experiments was sent to Professor Tom Fletcher of BYU (Subtask 4.3).

The solution NMR of the three bitumen samples and the solid state NMR of the shale and kerogen, along with the analysis of this data, was gathered together as the start of a manuscript on the chemical characterization of oil shale, isolated kerogen, and bitumen from the three segments of the Skyline 16 core. The current draft contains the solution NMR of the bitumen and the solid state NMR of the shale and the kerogen. The small angle X-ray scattering (SAXS) and the atomic pairwise distribution function (PDF) data is currently being analyzed. As this is a new analytical tool to all on this project, time has been spent learning how to use the analysis software. To this end, Dr. Anita Orendt attended a workshop on SAXS data analysis that was held at the Advanced Photon Source at Argonne National Laboratory in September 2012.

The manuscript "*Three-Dimensional Structure of the Siskin Green River Oil Shale Kerogen Model: A Comparison between Calculated and Observed Properties*" by Orendt, Pimenta, Badu, Solum, Pugmire, Facelli, Locke, Winans, Chapman and Chupas, submitted to *Energy & Fuels* (a deliverable of the related subtask 4.6), synthesizes the work of both this subtask and Subtask 4.6. This manuscript includes comparisons between experimental solid state ^{13}C NMR and PDF data obtained using kerogen isolated from the GR-1 segment (this subtask) and simulation data of these three observables obtained using the 3D kerogen model (Subtask 4.6).

Task 5.0 - Environmental, Legal, Economic and Policy Framework

Subtask 5.1 – Models for Addressing Cross-Jurisdictional Resource Management (PI: Robert Keiter, John Ruple)

This project has been completed.

Subtask 5.2 - Conjunctive Management of Surface and Groundwater Resources (PI: Robert Keiter, John Ruple)

This project has been completed.

Subtask 5.3 - Police and Economic Issues Associated with Using Simulation to Assess Environmental Impacts (PI: Robert Keiter, Kirsten Uchitel)

Subtask 5.3 researchers focused this quarter on completing the foundational research on the legal and policy framework for utilizing simulation science in the context of assessing environmental risks or harms. Good progress has been made on identifying relevant case law and law review analyses of the policy challenges inherent in judicial and agency assessments of simulation science, as well as relevant agency guidance.

6.0 – Economic and Policy Assessment of Domestic Unconventional Fuels Industry

Subtask 6.1 Engineering Process Models for Economic Impact Analysis (PI: Terry Ring)

All engineering process models were completed during this quarter, so the project team is now working on the final milestone. The milestone is to upload all models used and data collected to the repository or alternatively, to the ICSE website. Team members are working with the web site manager to complete this milestone in the next quarter. The deliverable is a written report describing the process models used and the parameters analyzed. Because all of this information is contained within Sections 5-9 of the Market Assessment (Subtask 6.3), the submission of those sections to R. Vagnetti in the next quarter will be considered the completion of this deliverable.

Subtask 6.2 - Policy analysis of the Canadian oil sands experience (PI: Kirsten Uchitel)

The topical report for this subtask is being finalized for delivery next quarter. It is proposed that the revised deliverable date for the topical report be November 30, 2012.

Subtask 6.3 – Market Assessment Report (PI: Jennifer Spinti)

The report was finalized during this quarter with draft copies being sent to a small group of reviewers after the quarter had ended. Comments from reviewers are due by November 16. Any changes will be incorporated into a final report. This version of the report will then be sent for review to companies who provided information for the report including Red Leaf Resources, Enefit American Oil, Gary Aho (formerly of Sage GeoTech), Headwaters Economics, Glen Vawters (National Oil Shale Association), and U.S. Oil Sands.

7.0 – Strategic Alliance Reserve

The Task 7.0 project team is continuing to meet with its industrial partner, AMSO, on a regular basis. Additionally, a two-day, first-year project review meeting was held on the University of Utah campus at the end of September. A panel of scientists and representatives of AMSO, Genie Energy, and TOTAL reviewed all three subtasks (7.1, 7.2, and 7.3). Feedback from this meeting is being used to realign tasks and budgets to better meet the overall objectives of the program.

Subtask 7.1 – Geomechanical Model (PI: John McLennan)

The focus of Subtask 7.1 researchers continues to be on methods for reasonably representing the matrix of experimental data that has been generated by AMSO. The tactics are to:

- Use hyperbolic relationships between stress and deformation to fit various constitutive behaviors – adopted from soil mechanics protocols. The MetaRock data have been evaluated to complement the NER (New England Research) stress-strain data that had previously been fit.
- Use neural networking protocols to interrelate constitutive (stress-strain) behavior to the governing independent variables. No additional developments have occurred in this area although team members anticipate appraising it in the upcoming quarter.

All of New England Research's triaxial testing information has been fitted in three generic regions. The Metarock triaxial testing information have been fitted in this quarter. A summary of analysis protocols referred to Table 4 can be found in the March-June 2012 quarterly report.

Table 4. Loading regimes.

Region	Identifier	Description
Loading - 1	Elastic	During loading, there are finite loading regimes that have characteristics of linearity that we are labeling as elastic (linear elastic). Candidly, the linearity is no guarantee of elastic behavior.
Loading - 2	Hyperbolic	After the so-called elastic behavior, a hyperbolic fit was carried out
Loading - 3	Post-Hyperbolic	Behavior after the hyperbolic zone was variable – covering strain hardening, perfect plasticity, and strain softening. At this time a linear fit, with no constitutive interpretation, is carried out.
Unloading - 4	Hyperbolic	The difficulty with the unloading portion is that it was not necessarily done at a constant, controlled rate.

Subtask 7.2 – Kinetic Compositional Models and Thermal Reservoir Simulators (PI: Milind Deo)

As noted last quarter, this project has been in transition due to the graduation of three students and the hiring of a new post-doctoral fellow. This post-doctoral fellow spent a month learning about the project before beginning to make contributions. However, in the same time frame, the project was reviewed by representatives of AMSO, Total, and Genie as noted previously. The feedback from the reviewers was that they did not see a lot of promise in using STARS for their application. Consequently, the management team is working on reallocating resources from this project to Subtasks 7.1 and 7.3. Follow-up documentation will be provided for a revised Project Management Plan.

Subtask 7.3 – Rubblized Bed High Performance Computing Simulations (PI: Philip Smith)

In this quarter, the milestone to perform a generation 1 simulation that includes the Discrete Element Method (DEM), Computational Fluid Dynamics (CFD), and thermal analysis of characteristic section of AMSO rubblized bed was completed. Under the current experimental operating conditions, there is no thermal rubblization occurring. Therefore, after discussions with AMSO, the Subtask 7.3 team expanded the characteristic section to include the entire heater test experimental section. With the generation 1 simulations described below, the team has computed the heat distribution inside the test section and compared the results to experimental data. Results from this milestone completion will be presented at the 32nd Oil Shale Symposium in Golden, CO.

To complete this milestone, Subtask 7.3 researchers have improved the geometric representation of the process used by their industrial partner AMSO based on the latest field geometric data and on previous simulations of the AMSO heater experiment dating from January of this year. The simulation model has been further improved by incorporating depth- and temperature-varying properties that closely describe the shale formation at the AMSO site. The research team continues to work closely with AMSO scientists during each step of the simulation process and receives continuous feedback through frequent teleconferences and visits by AMSO team to the University of Utah.

The computational domain created by the project team in the previous quarter is shown in Figure 14. This geometry was used initially to simulate the heater test conducted by AMSO. While the geometry of the production well and of the lower and upper laterals (all blue in color) were created from actual gyro surveys, locations and shapes of the tomography wells (vertical wells in light gray color) used to measure temperature data during the test were estimated from field locations available at the time.

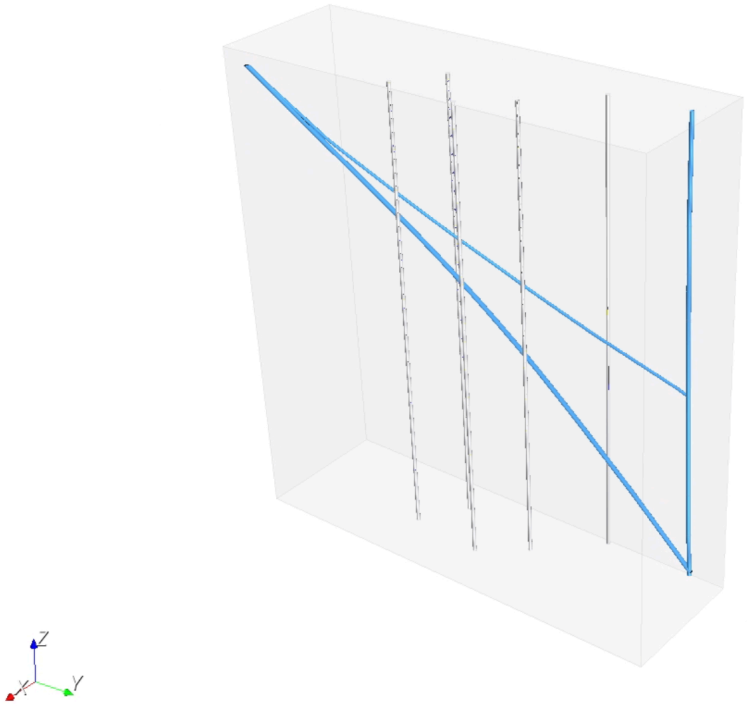

Figure 14: Computational geometry created previous quarter representing the AMSO heater test; production well and lower and upper laterals are in blue, the tomography wells in gray.

During this quarter, team members refined the shape and locations of the tomography wells to match the actual field gyro surveys. The updated geometry is shown in Figure 15. Both the side and top views show the irregular length and shapes of the tomography wells. Locations of all tomography wells with respect to the convection loop (which comprises the lower and upper laterals and the production well) are extremely important for comparison to experimental results.

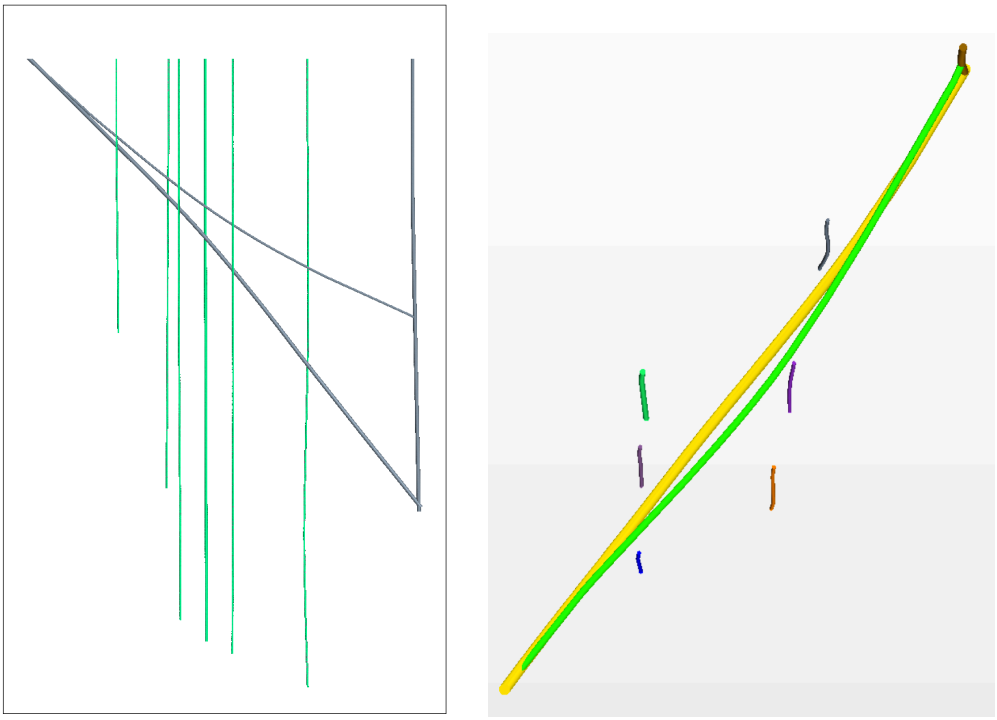

Figure 15: (Left) Side view of the updated AMSO heater test geometry. All wells, including the tomography wells, were constructed using the latest field gyro surveys. (Right) Top view of the AMSO heater test geometry, which clearly shows the updated, irregular shape of the vertical tomography wells.

AMSO heated the shale formation using a heater placed in the lower lateral well. In January 2012, this heater was brought up to a temperature of about 700 K over a period of few days. After that, the heater was turned off. Since the start of heating, AMSO has continuously monitored and measured the temperature response of the shale formation at each of the tomography wells to the original heat introduced in the lower lateral. The project team is trying to replicate this experiment with simulations and, thus help AMSO scientists gain further insight into their process.

In this quarter, team members went through two iterations of simulations using the new geometry. In the first iteration, they incorporated shale properties initially provided by AMSO scientists. After reviewing the results and receiving feedback from AMSO, it was clear that Star-CCM+ capabilities needed to be extended to include property variations not only based on temperature, but also on depth. This task was accomplished by using tools developed in conjunction with work from Subtask 4.1, which incorporated the temperature and spatial variability in properties such as density, thermal conductivity, and specific heat over the entire computational domain. This enhancement greatly improved the applicability of Star-CCM+ to both the Red Leaf and AMSO processes. Furthermore, AMSO provided researchers with more detailed properties of the shale formation at their experimental site.
For the second simulation iteration, the project team incorporated AMSO data for density, thermal conductivity, and specific heat as functions of both depth and temperature. Using these highly variable properties, team members obtained temperature profiles at each tomography well which compare well to the experimental temperature measurements conducted by AMSO. One such comparison of temperatures from the simulation with the experimental measurements is shown in Figure 16. The two red lines, which represent the simulation results, show the

temperatures at the near and far locations of the respective tomography well, while the blue markers show the experimental results. While there are some discrepancies between the simulation and experimental results, the simulation does predict the correct behavior of the temperature distribution over time surprisingly well.

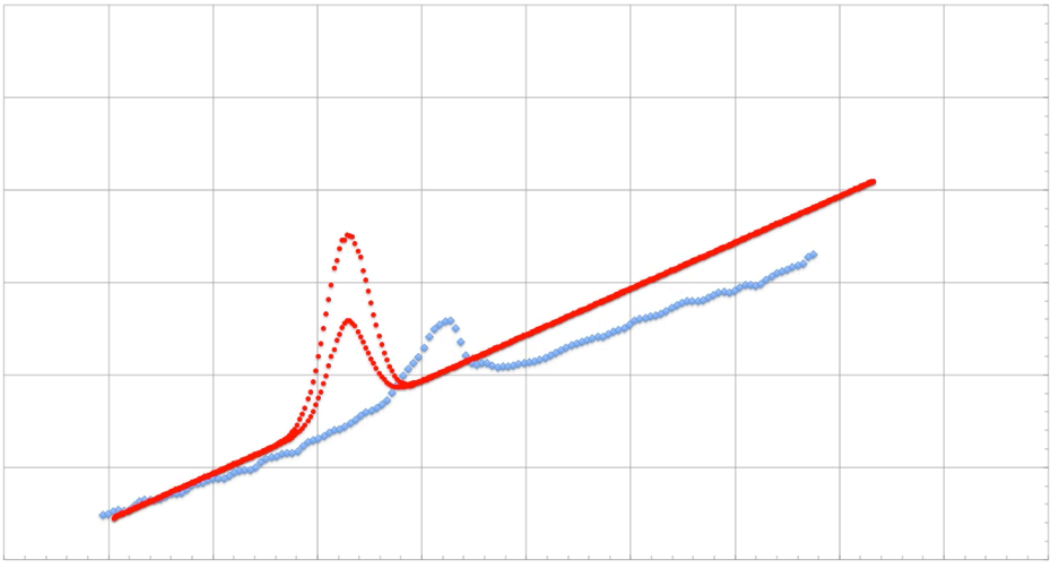

Figure 16: Comparison of temperature distribution in one of the tomography wells for simulation (red markers) and experimental results (blue markers). Horizontal axis represents depth, while the vertical axis represents the temperature.

These results were presented at the project review meeting held at the University of Utah at the end of September. The feedback from the review panel (AMSO, Genie Energy, and TOTAL) is that these results show great promise in providing further understanding of the AMSO process. AMSO scientist Len Switzer also presented this work at the 32nd Oil Shale Symposium in Golden, CO.

The Subtask 7.3 team will continue to work with AMSO to expand their set of HPC-based simulation tools so that they can further improve representation of the actual AMSO heater test in their simulations. They also plan to conduct V/UQ studies that better understand sensitivities and effects associated with the experimental boundary conditions as well simulation parameters on the overall temperature distribution for the AMSO heater test.

CONCLUSIONS

In this quarter, Subtask 4.6 was completed and a first-year review meeting of all Task 7.0 projects was conducted. Several projects are preparing final reports for delivery next quarter, including Subtasks 3.1, 6.1, 6.2, and 6.3. A group of four ICSE researchers (Professors Philip Smith, John McLennan, Milind Deo, and Tom Fletcher) made preparations to teach a two-day short course on kerogen liquefaction to a group of Statoil employees in Trondheim, Norway.

COST PLAN/STATUS

Baseline Reporting Quarter - PHASE I	Yr. 1								Yr. 2			
	Q1		Q2		Q3		Q4		Q5		Q6	
	7/1/09 - 12/31/09		1/1/10 - 3/31/10		4/1/10 - 6/30/10		7/1/10 - 9/30/10		10/1/10 - 12/31/10		1/1/11 - 3/31/11	
	Q1	**Total**	Q2	**Total**	Q3	**Total**	Q4	**Total**	Q5	**Total**	Q6	**Total**
Baseline Cost Plan												
Federal Share	484,728	**484,728**	484,728	**969,456**	484,728	**1,454,184**	484,726	**1,938,910**	323,403	**2,262,313**	798,328	**3,060,641**
Non-Federal Share	121,252	**121,252**	121,252	**242,504**	121,252	**363,756**	121,254	**485,010**	80,835	**565,845**	199,564	**765,409**
Total Planned	605,980	**605,980**	605,980	**1,211,960**	605,980	**1,817,940**	605,980	**2,423,920**	404,238	**2,828,158**	997,892	**3,826,050**
Actual Incurred Cost												
Federal Share	420,153	**420,153**	331,481	**751,634**	547,545	**1,299,179**	428,937	**1,728,116**	593,386	**2,321,502**	307,768	**2,629,270**
Non-Federal Share	29,456	**29,456**	131,875	**161,332**	151,972	**313,304**	100,629	**413,933**	191,601	**605,534**	45,101	**650,635**
Total Incurred Costs	449,609	**449,609**	463,356	**912,966**	699,517	**1,612,483**	529,566	**2,142,049**	784,987	**2,927,036**	352,869	**3,279,905**
Variance												
Federal Share	64,575	**64,575**	153,247	**217,822**	-62,817	**155,005**	55,789	**210,794**	-269,983	**-59,189**	490,560	**431,371**
Non-Federal Share	91,796	**91,796**	-10,623	**81,172**	-30,720	**50,452**	20,625	**71,077**	-110,766	**-39,689**	154,463	**114,774**
Total Variance	156,371	**156,371**	142,624	**298,994**	-93,537	**205,457**	76,414	**281,871**	-380,749	**-98,878**	645,023	**546,145**

Note: Q5 and Q6 reflect both CDP 2009 and CDP 2010 SF424a projections as the award periods overlap.

Baseline Reporting Quarter - PHASE II	Yr. 2				Yr. 3							
	Q7		Q8		Q9		Q10		Q11		Q12	
	04/01/11 - 06/30/11		07/01/11 - 09/30/11		10/01/11 - 12/31/11		01/1/12 - 03/31/12		04/01/12 - 06/30/12		07/01/12 - 09/30/12	
	Q7	**Total**	Q8	**Total**	Q9	**Total**	Q10	**Total**	Q11	**Total**	Q12	**Total**
Baseline Cost Plan												
Federal Share	712,385	**3,773,026**	627,423	**4,400,449**	147,451	**4,547,900**	147,451	**4,695,351**	147,451	**4,842,802**	245,447	**5,088,249**
Non-Federal Share	178,100	**943,509**	156,854	**1,100,363**	36,863	**1,137,226**	36,863	**1,174,089**	36,863	**1,210,952**	58,906	**1,269,858**
Total Planned	890,485	**4,716,535**	784,277	**5,500,812**	184,314	**5,685,126**	184,314	**5,869,440**	184,314	**6,053,754**	304,353	**6,358,107**
Actual Incurred Cost												
Federal Share	449,459	**3,078,729**	314,813	**3,393,542**	271,897	**3,665,439**	267,784	**3,933,223**	191,438	**4,124,661**	232,367	**4,357,028**
Non-Federal Share	48,902	**699,537**	48,835	**748,372**	105,695	**854,067**	40,652	**894,719**	33,092	**927,811**	44,294	**972,105**
Total Incurred Costs	498,361	**3,778,266**	363,648	**4,141,914**	377,592	**4,519,506**	308,436	**4,827,942**	224,530	**5,052,472**	276,661	**5,329,133**
Variance												
Federal Share	262,926	**694,297**	312,610	**1,006,907**	-124,446	**882,461**	-120,333	**762,128**	-43,987	**718,141**	13,080	**731,221**
Non-Federal Share	129,198	**243,972**	108,019	**351,991**	-68,832	**283,159**	-3,789	**279,370**	3,771	**283,141**	14,612	**297,753**
Total Variance	392,124	**938,269**	420,629	**1,358,898**	-193,278	**1,165,620**	-124,122	**1,041,498**	-40,216	**1,001,282**	27,692	**1,028,974**

Baseline Reporting Quarter - PHASE II	Yr. 4											
	Q13		Q14		Q15		Q16					
	10/01/12 - 12/31/12		01/01/13 - 03/31/13		04/01/13 - 06/30/13		07/01/13 - 09/30/13					
	Q13	**Total**	Q14	**Total**	Q15	**Total**	Q16	**Total**		**Total**		**Total**
Baseline Cost Plan												
Federal Share	146,824	**5,235,073**	146,824	**5,381,897**	146,824	**5,528,721**	133,794	**5,662,515**				
Non-Federal Share	36,705	**1,306,563**	36,705	**1,343,268**	36,705	**1,379,973**	35,906	**1,415,879**				
Total Planned	183,529	**6,541,636**	183,529	**6,725,165**	183,529	**6,908,694**	169,700	**7,078,394**				
Actual Incurred Cost												
Federal Share		**4,357,028**		**4,357,028**		**4,357,028**		**4,357,028**				
Non-Federal Share		**972,105**		**972,105**		**972,105**		**972,105**				
Total Incurred Costs		**5,329,133**		**5,329,133**		**5,329,133**		**5,329,133**				
Variance												
Federal Share		**878,045**		**1,024,869**		**1,171,693**		**1,305,487**				
Non-Federal Share		**334,458**		**371,163**		**407,868**		**443,774**				
Total Variance		**1,212,503**		**1,396,032**		**1,579,561**		**1,749,261**				

MILESTONE STATUS

ID	Title/Description	Planned Completion Date	Actual Completion Date	Milestone Status
1.0	Project Management			
2.0	Technology Transfer and Outreach			
	Advisory board meeting	Jun-12		
	Hold final project review meeting in format determined jointly by DOE/NETL and ICSE	Jun-13		
3.0	Clean Oil Shale & Oil Sands Utilization with CO2 Management			
3.1	Lifecycle greenhouse gas analysis of conventional oil & gas development in the Uinta Basin			
	Complete modules in $CLEAR_{uff}$ for life-cycle CO2 emissions from conventional oil & gas development in the Uinta Basin	Jun-12		Project on hold pending completion of Subtask 6.3
3.2	Flameless oxy-gas process heaters for efficient CO2 capture			
	Preliminary report detailing results of skeletal validation/uncertainty quantification analysis of oxy-gas combustion system	Sep-12	Oct-12	Report attached as appendix to this quarterly report
3.3	Development of oil & gas production modules for $CLEAR_{uff}$			
	Develop preliminary modules in $CLEAR_{uff}$ for conventional oil & gas development & produced water management in Uinta Basin	Oct-11	Dec-11	Discussed in Jan. 2012 quarterly report
3.4	V/UQ analysis of basin scale $CLEAR_{uff}$ assessment tool			
	Develop a first generation methodology for doing V/UQ analysis	Oct-11	Nov-11	Discussed in Jan. 2012 quarterly report
	Demonstrate full functionality (integration of all modules) of V/UQ methodology for conventional oil & gas development in Uinta Basin	Apr-12		Project on hold pending completion of Subtask 6.3
4.0	Liquid Fuel Production by In-Situ Thermal Processing of Oil Shale/Sands			
4.1	Development of CFD-based simulation tool for in-situ thermal processing of oil shale/ sands			

ID	Title/Description	Planned Completion Date	Actual Completion Date	Milestone Status
	Expand modeling to include reaction chemistry & study product yield as a function of operating conditions	Feb-12	Mar-12	
4.2	Reservoir simulation of reactive transport processes			
	Incorporate kinetic & composition models into both commercial & new reactive transport models	Dec-11	Dec-11	Discussed in this quarterly report
	Complete examination of pore-level change models & their impact on production processes in both commercial & new reactive transport models	Jun-12	Jun-12	Discussed in July 2012 quarterly report
4.3	Multiscale thermal processes			
	Complete thermogravimetric analyses experiments of oil shale utilizing fresh “standard” core	Sep-11	Sep-11	Discussed in Oct. 2011 quarterly report
	Complete core sample pyrolysis at various pressures & analyze product bulk properties & composition	Dec-11	Sep-12	Discussed in this quarterly report
	Collection & chemical analysis of condensable pyrolysis products from demineralized kerogen	May-12	Sep-12	Discussed in this quarterly report
	Complete model to account for heat & mass transfer effects in predicting product yields & compositions	Jun-12	Jun-12	Discussed in this quarterly report
4.5	In situ pore physics			
	Complete pore network structures & permeability calculations of Skyline 16 core (directional/anisotropic, mineral zones) for various loading conditions, pyrolysis temperatures, & heating rates	Mar-12	Mar-12	Discussed in April 2012 quarterly report for 1 loading condition; add’l loading condition by Dec. 2012
4.6	Atomistic modeling of oil shale kerogens & oil sand asphaltenes			
	Complete web-based repository of 3D models of Uinta Basin kerogens, asphaltenes, & complete systems (organic & inorganic materials)	Dec-11	Dec-11	Discussed in Jan. 2012 quarterly report
4.7	Geomechanical reservoir state			
	Complete high-pressure, high-temperature vessel & ancillary flow system design & fabrication	Sep-11	Sep-11	Discussed in Oct. 2011 quarterly report
	Complete experimental matrix	Feb-12		Revised test matrix presented in this report
	Complete thermophysical & geomechanical property data analysis & validation	Apr-12		Experimental apparatus still undergoing final testing

ID	Title/Description	Planned Completion Date	Actual Completion Date	Milestone Status
4.8	Developing a predictive geologic model of the Green River oil shale, Uinta Basin			
	Detailed sedimentologic & stratigraphic analysis of three cores &, if time permits, a fourth core	Dec-12		
	Detailed mineralogic & geochemical analysis of same cores	Dec-12		
4.9	Experimental characterization of oil shales & kerogens			
	Characterization of bitumen and kerogen samples from standard core	Jan-12	Feb-12	Email sent to R. Vagnetti
	Development of a structural model of kerogen & bitumen	Jun-12	Jun-12	Discussed in July 2012 quarterly report
5.0	Environmental, legal, economic, & policy framework			
5.1	Models for addressing cross-jurisdictional resource management			
	Identify case studies for assessment of multi-jurisdictional resource management models & evaluation of utility of models in context of oil shale & sands development	Jun-11	Jul-11	Discussed in Oct. 2011 quarterly report
5.2	Conjunctive management of surface & groundwater resources			
	Complete research on conjunctive surface water & groundwater management in Utah, gaps in its regulation, & lessons that can be learned from existing conjunctive water management programs in other states	Aug-11	Aug-11	Discussed in Oct. 2011 quarterly report
5.3	Policy & economic issues associated with using simulation to assess environmental impacts			
	White paper describing existing judicial & agency approaches for estimating error in simulation methodologies used in context of environmental risk assessment and impacts analysis	Dec-12		
6.0	Economic & policy assessment of domestic unconventional fuels industry			
6.1	Engineering process models for economic impact analysis			
	Upload all models used & data collected to repository	Oct-11		New completion data of Sept. 2012

ID	Title/Description	Planned Completion Date	Actual Completion Date	Milestone Status
7.0	Strategic Alliance Reserve			
	Conduct initial screening of proposed Strategic Alliance applications	Mar-11	Mar-11	
	Complete review and selection of Strategic Alliance applications	Jun-11	Jul-11	Discussed in Oct. 2011 quarterly report
	Implement new Strategic Alliance research tasks	Sep-11	Sep-11	Discussed in Oct. 2011 quarterly report
7.1	Geomechanical model			
	Infer permeability-porosity-temperature relationships, develop model that can be used by other subtasks	Dec-12		
	Make experimental recommendations	Aug-13		
7.2	Kinetic compositional models & thermal reservoir simulators			
	Incorporate chemical kinetics into thermal reservoir simulators	Jun-12	Jun-12	Discussed in July 2012 quarterly report
	Demonstrate reservoir simulation of AMSO process	Sep-12		Project being phased out based on first-year review
	Incorporate poroelastic & geomechanical models into reservoir simulator	Jun-13		
7.3	Rubblized bed HPC simulations			
	Collect background knowledge from AMSO about characteristics & operation of heated wells	Jun-12	Jun-12	Discussed in July 2102 quarterly report
	Perform generation 1 simulation - DEM, CFD & thermal analysis of characteristic section of AMSO rubblized bed	Sep-12	Sep-12	Discussed in this quarterly report
	Perform generation 2 simulation that incorporates kinetic compositional models from subtask 7.2 and/or AMSO	Jun-13		

NOTEWORTHY ACCOMPLISHMENTS

The Subtask 4.7 team performed unconfined compression measurements and thermal conductivity measurements. They successfully measured axial strains and stress, with and without copper jacketing.

PROBLEMS OR DELAYS

The Market Assessment (Subtask 6.3) was sent to reviewers after this quarter ended. With its completion, Subtask 6.1 is now being wrapped up as well. All models and data will be uploaded to a project page on the ICSE website in the next quarter. Because researchers involved in the assessment are also responsible for Task 3.0 projects, the work that was previously on hold has now been restarted as noted in the above work summaries. In Subtask 4.3, the computer holding the experimental data for samples GR-3.9 and GR-1.9 failed and is unreachable at this time. Luckily the computer problem seems resolvable and within a few weeks should be resolved. Researchers for Subtask 4.7 had additional equipment design modifications in this quarter, including the preparation of a new heater design. For Subtask 4.9, the time needed to properly understand and interpret the SAXS and PDF data has resulted in the delay of the completion of the manuscript on the kerogen structure (from information obtained from the experimental characterization). Team members are working on this deliverable and will provide a copy to DOE when the manuscript is ready for submission.

During the next quarter, a revised PMP will be submitted in order to re-baseline some of the projects.

RECENT AND UPCOMING PRESENTATIONS/PUBLICATIONS

List of publications/presentations

Wilkey, J. (2011, December). Evaluation of the economic feasibility of heavy oil production processes for West Sak Field. MS Thesis, University of Utah, Salt Lake City, UT.

R. Keiter, J. Ruple, H. Tanana and R. Holt. (2012, January). Conjunctive surface and groundwater management in Utah: Implications for oil shale and oil sands development. Submitted to the Department of Energy under DOE Award No. DE-FE0001243.

Tiwari, P. & Deo, M. (2012, February). Detailed kinetic analysis of oil shale pyrolysis TGA data. *AICHE Journal*, *58(2*), 505-515.

Spinti, J. (2012, February 15). Presenter/panelist - *Oil sands: How Utah can improve on the Alberta model.* Utah Governor's Energy Development Summit, Salt Lake City, UT.

Deo, M. (2012, February 15). Presenter/panelist - *Oil sands: How Utah can improve on the Alberta model.* Utah Governor's Energy Development Summit, Salt Lake City, UT.

Tiwari, P. & Deo, M. (2012, April). Compositional and kinetic analysis of oil shale pyrolysis using TGA-MS. *Fuel*, *94*, 333-341.

Rosenberg, M., Birgenheier, L. & Vanden Berg, M. (2012, April) Outcrop examination and sequence stratigraphy of the lacustrine Green River Formation, Uinta Basin, Utah: Implications for conventional and unconventional oil and gas development. Poster presented

at the annual meeting of the American Association of Petroleum Geologists Annual Convention, Long Beach, CA, April 22-25, 2012.

Eby, D., Chidsey, T., Vanden Berg, M. & Laine, M. (2012, April). Microbial carbonates from core and outcrop, Tertiary (Eocene) Green River Formation, Uinta Basin, Utah. Paper presented at the American Association of Petroleum Geologists Annual Convention, Long Beach, CA, April 22-25, 2012.

Badu, S., Pimienta, I. S. O., Orendt, A. M. Facelli, J. C. & Pugmire, R. J. (2012). Modeling of asphaltenes: Assessment of sensitivity of ^{13}C SSNMR to molecular structure. Submitted to *Energy & Fuels, 26(4),* 2161-2167.

Fletcher, T. H., Orendt, A. M., Facelli, J. C., Solum, M. S., Mayne, C. L. & Deo, M. (2012, May 15). Kinetics of Uinta Basin oil shale pyrolysis. Presentation at the 2012 University of Utah Unconventional Fuels Conference, Salt Lake City, UT.

Ruple, J. (2012, May 15). Wilderness quality lands and unconventional fuel development. Presentation at the 2012 University of Utah Unconventional Fuels Conference, Salt Lake City, UT.

Tiwari, P. (2012). Oil shale Pyrolysis: Benchscale experimental studies and modeling. Ph.D. dissertation, Department of Chemical Engineering, University of Utah.

Lin, C. L., Miller, Hsieh, C. H., Tiwari, P. & Deo, M. D. (2012, May). Characterization of core pore structure before and after pyrolysis using X-ray micro CT. Paper submitted to *Fuel*.

Tiwari, P., Deo, M., Lin C. L. & Miller, J.D. (2012, October). Characterization of the oil shale core pore structure before and after pyrolysis. Paper accepted for presentation at the 2012 AICHE Annual Meeting in Pittsburgh, PA, October 28-November 2, 2012.

Vanden Berg, M. D., Birgenheier, L. P. & Rosenberg M. J. (2012, September). Core-based sedimentologic, stratigraphic, and geochemical analysis of the lacustrine upper Green River Formation, Uinta Basin, Utah: Implications for conventional and unconventional petroleum development. Poster presented at the 2012 AAPG-RMS Meeting in Grand Junction, CO.

Rosenberg, M.J., Birgenheier, L.P, & Vanden Berg, M.D. (2012, October). Sedimentology and Sequence Stratigraphy of the Green River Formation, eastern Uinta Basin, Utah. Paper to be presented at the 32nd Oil Shale Symposium in Golden, CO.

Burnham, A., Day, R., Switzer, L., McConaghy, J., Hradisky, M., Coates, D., Smith, P., Foulkes, J., La Brecque, D., Allix, P., Wallman, H. (2012, October). Initial results of the AMSO RD&D pilot test program. Paper to be presented at the 32nd Oil Shale Symposium in Golden, CO.

Pimienta, I. S. O., Orendt, A. M., Pugmire, R. J., Facelli, J. C., Locke, D. R., Winans, R. E., Chapman, K. W. & Chupas, P. J. (2012, October). Three-dimensional structure of the Siskin Green River oil shale kerogen model: A comparison between calculated and observed properties. Submitted to *Energy and Fuels*.

Deo, M. (2012, October). *Oil shale liquefaction: Modeling and reservoir simulation*. Short course presentation to Statoil, Trondheim, Norway.

Deo, M. (2012, October). *Oil shale conversion to liquids: Experimental aspect*. Short course presentation to Statoil, Trondheim, Norway.

Fletcher, T. H. (2012, October). *Oil shale 1: Chemical structure and pyrolysis*. Short course presentation to Statoil, Trondheim, Norway.

McLennan, J. (2012, October). *Legacy and new geomechanical measurements of oil shale*. Short course presentation to Statoil, Trondheim, Norway.

Smith, P. J. (2012, October). *Multiscale simulation*. Short course presentation to Statoil, Trondheim, Norway.

Smith, P. J. (2012, October). *A description of a UQ-predictive validation framework for application to difficult engineering problems*. Short course presentation to Statoil, Trondheim, Norway.

Birgenheier, L. & Vanden Berg, M. (n.d.). Manuscript that documents regional and stratigraphic changes in the Green River Formation, Uinta Basin, Utah. To be published in a special edition book titled *Stratigraphy and Limnogeology of the Eocene Green River Formation*.

Bauman. J. H. & Deo, M. D. (n.d.) Simulation of a conceptualized combined pyrolysis, in situ combustion, and CO_2 storage strategy for fuel production from Green River oil shale. Submitted to *Energy and Fuels*.

Orendt, A. , Pimienta, I. S. O., Badu, S., Solum, M., Pugmire, R. J., Facelli, J. C., Locke, D. R., Winans, R. E., Chapman, K. W. & Chupas, P. J. (n.d.). Three-dimensional structure of the Siskin Green River oil shale kerogen model: A comparison between calculated and observed properties. Manuscript in draft form.

REFERENCES

Advanced Resources, Int. (2008, November 10). Greenhouse gas life-cycle emissions study: Fuel life-cycle of U.S. natural gas supplies and international LNG. Available at http://www.adv-res.com/pdf/ari_lca_nov_10_08.pdf.

Argonne National Laboratory. (2012). The Greenhouse gases, Regulated Emissions, and Energy use in Transportation (GREET) Model, rev1. Accessed August 2012 at http://greet.es.anl.gov/.

Brandt, A. R., 2008. Converting oil shale to liquid fuels: energy inputs and greenhouse gas emissions of the shell in situ conversion process. *Environmental Science and Technology, 42 (19)*, 7489-7495.

Hillier, J. L. (2011). *Pyrolysis kinetics and chemical structure considerations of a Green River oil shale and its derivatives*. Ph.D. dissertation, Chemical Engineering Department, Brigham Young University.

Hillier, J., Bezzant, T. & Fletcher, T. H. (2010). Improved method for determination of kinetic parameters from non-isothermal TGA data. *Energy & Fuels, 24,* 2841-2847.

Hillier, J. L. & Fletcher, T. H. (2011). Pyrolysis kinetics of a Green River Oil Shale using a pressurized TGA. *Energy & Fuels*, *25,* 232-239.

McKellar, J.M., Charpentier, A.D., Bergerson, J.A., MacLean, H.L., 2009. A life cycle greenhouse gas emissions perspective on liquid fuels from unconventional Canadian and US fossil sources. *International Journal of Global Warming, 1(1/2/3),*160-178.

U.S. Environmental Protection Agency. (2009, May 29). *Lifecycle greenhouse gas (GHG) emissions results spreadsheets,* Docket ID: EPA-HQ-OAR-2005-0161-0938. Retrieved

November 29, 2011 from www.regulations.gov.

U.S. Department of Energy, National Energy Technology Laboratory. (2009, March 27). *An evaluation of the extraction, transport, and refining of imported crude oils and the impact on life cycle greenhouse gas emission* (DOE/NETL-2009/1362). Pittsburgh, PA: Author.

APPENDIX A. Preliminary report (see attached).

APPENDIX B. Kerogen modeling paper (see attached).

PRELIMINARY REPORT:

Flameless Oxy-gas Process Heaters for Efficient CO_2 Capture

Author: Jennifer Spinti

DOE Award No.: DE-FE0001243

Reporting Period: October 1, 2009 – September 30, 2011

Report Issued: October 2012

Submitted by:
University of Utah
Institute for Clean and Secure Energy
155 South 1452 East, Room 380
Salt Lake City, UT 84112-0190

Prepared for:
United States Department of Energy
National Energy Technology Laboratory

Introduction

With growing concern for the effect of carbon dioxide (CO_2) emissions on global climate, various methodologies have been proposed for more efficiently capturing such emissions from large, stationary combustion sources. Oxy-firing, wherein combustion takes place between the fuel and oxygen (O_2) mixed with recycled flue gas (RFG), has shown promise as a retrofit technology. Because the nitrogen diluent has been removed prior to combustion, an O_2-RFG environment produces a post-combustion gas with high CO_2 concentrations (up to 95% on a dry basis), making this stream suitable for use in enhanced oil recovery, for use as a feedstock, or for sequestration without large additional expenses for separation. However, wide-scale deployment of oxy-firing technology requires information on the impact such firing might have on the operation of the unit in question, including any changes to the heat transfer characteristics and to NO_x emissions.2

The goals of this project were to develop a Large Eddy Simulation (LES) tool for demonstrating practical oxy-gas combustion in process heaters and then to apply that technology in a formal Validation/Uncertainty Quantification (V/UQ) analysis to demonstrate predictive capability with quantified uncertainty bounds for pilot-scale (or larger) process heaters. This preliminary report summarizes the work to create a suitable LES tool and to apply a V/UQ framework to an oxy-gas pilot-scale test, including results from screening tests.

Oxy-gas Test Case

The first project task was to identify the intended use of the LES tool, e.g. the experimental data set from an oxy-fired process heater at the pilot- or commercial-scale. The project team initially selected the International Flame Research Foundation's (IFRF) OXYFLAM experiments, collected in 1995-96, as the foundation for this V/UQ analysis (Lallement et al., 1997). This tests were atypical for oxy-gas firing in that there was no RFG, leading to high temperatures and steep temperature gradients in the near burner region. Several months into the project, team members attended an IFRF conference in Glasgow, Scotland and learned of a more recent data featuring the ENEL TEA-C burner and a retrofitted FOSPER plant that allowed for oxy-combustion with RFG (Coraggio and Laiola, 2009). In these experiments, the RFG is mixed with O_2 prior to combustion with the natural gas. Measurements taken in these flames include gas temperatures; species concentrations of O_2, CO_2, NO_x, and CO; and heat flux at the furnace walls. The decision was made to focus on this data set for all subsequent work.

Development of Arches Simulation Tool

The second project task was to develop an LES tool capable of simulating the FOSPER furnace and TEA-C burner. The relatively simple furnace geometry, shown in Figure 1,

consists of a refractory-lined, 6.25 meter (m) long chamber with an internal square cross section of 2 m x 2 m. It is divided into 11 sections, each of which is independently water-cooled.

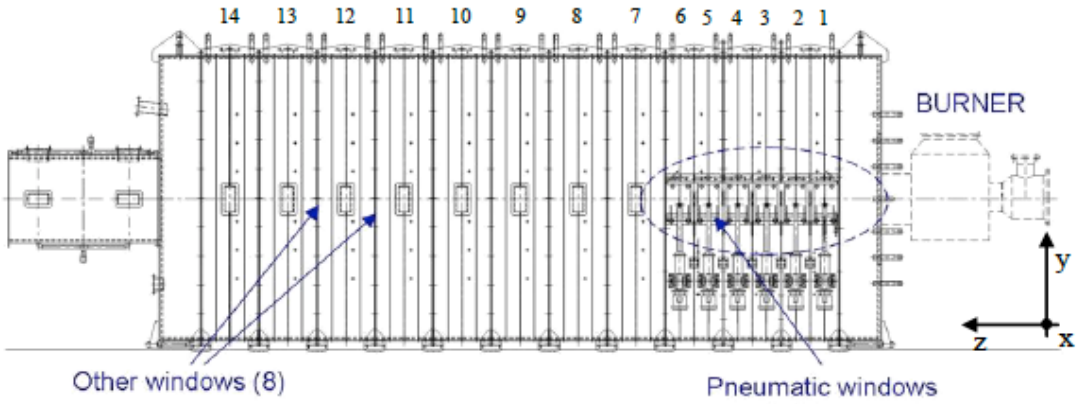

(a)

(b)

Figure 1: (a) Side view of FOSPER furnace from Coraggio and Laiola (2009); (b) view of exhaust end of FOSPER furnace from Tognotti (2007)

In contrast, the TEA-C burner, shown in Figure 2, has a very complex geometry; flows exiting the furnace have velocity components in all three directions. There are internal swirl vanes in both the secondary and tertiary oxidant inlets as indicated in Figure 2(a). The RFG stream is split prior to the burner and one stream feeds directly into the primary inlet, located along the centerline of the burner. The other RFG stream is spiked with O_2 and fed through the secondary and tertiary inlets. The secondary oxidant enters the furnace through openings behind the gas lances while the tertiary inlet is a narrow annular ring between the flared outer edge and the flared middle section, both of which

can be seen in Figure 2(b). The natural gas enters the furnace through eight lances that have two angled holes each.

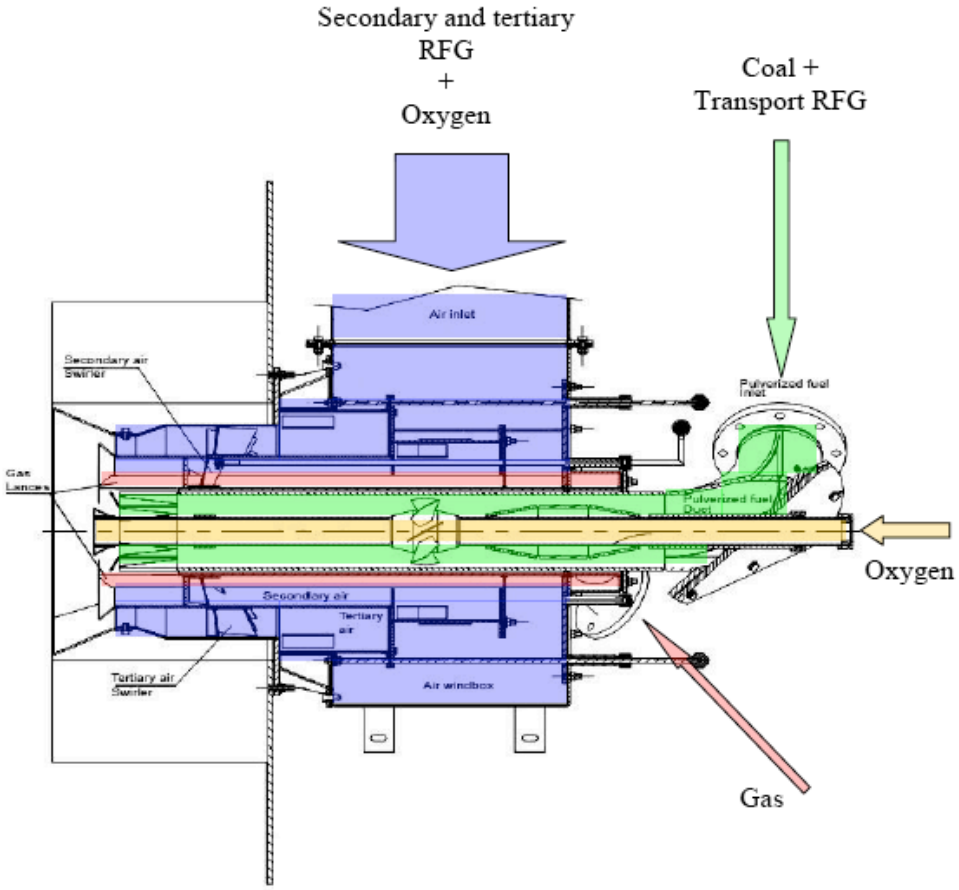

(a)

(b)

Figure 2: (a) Schematic cross-section of the TEA-C burner showing the swirl vanes and the location of various inlet stream from Coraggio and Laiola (2009); (b) view of burner exit plane from Coraggio et al. (2011).

Three challenges presented themselves for this IFRF burner/furnace configuration. First, the tool that was contemplated for this project, the Arches LES code, did not have the capability to recreate the complexities of the burner geometry. Second, due to computational limitations, it was not possible to resolve the details of the burner while at the same time extending the domain boundaries to the length and width of the FOSPER furnace. Third, preliminary simulations that included the flow constriction at the furnace exit from the 2 m x 2 m cross section to a round pipe of 0.6 m in diameter (see Figure 1) were very unstable.

To address these challenges, the project team decided to consider the burner only as an inlet boundary condition with the computational domain extending from the burner exit plane to a length of 4 m with a cross sectional area of 2 m x 2 m. The burner quarl is included in the computational mesh and the furnace walls provide the domain boundary condition. By removing the problematic constriction at the exit, the instability problem was eliminated and the resolution of the cross-sectional area could be increased. Increased resolution translates into a better-resolved burner boundary condition.

Even with this decision regarding the computational domain, Arches software development was required to provide an adequate geometric approximation of the burner inlet boundary condition (see Figure 2(b)), to allow for representative velocity fields for the swirled oxidant flows and the angled fuel jets, and to model thermal NO_x formation. While Coraggio and Laiola (2009) did not directly measure the velocity components at the burner inlet, the swirl number clearly had an effect on their flame profiles (e.g. temperature, CO_2 and O_2 concentrations, etc.). A thermal NO_x model was needed as it is the dominant NO_x formation mechanism in these types of flames and has a finite reaction rate that is not accurately reflected by an equilibrium chemistry assumption. Also, because Arches was designed for systems with open boundary conditions, additional coding was needed to run this configuration with walls. All new models underwent a thorough verification process.

The burner geometry as approximated for the Arches LES simulations is shown in Figure 3. Figure 4 is a side view of the furnace showing the quarl geometry and the overall size of the computational domain (2 m x 2 m x 4 m). The primary RFG stream enters the domain through a series of 4-square shaped inlets in the middle of the burner. The natural gas inlets consist of a series of 8 jets colocated in the secondary RFG + O_2 annular ring. The tertiary oxidant enters the domain through the outer annular ring. The mesh resolution is 228 x 468 x 228, so the cell size in the furnace cross section is 0.877 cm and in the axial direction is 0.855 cm. All cases were run on 1344 processors for approximately 72 hours.

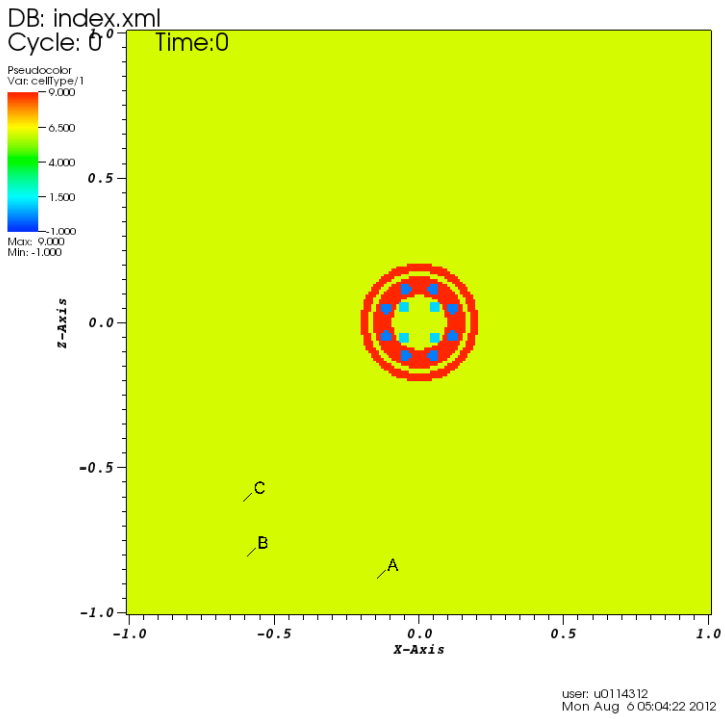

Figure 3: Burner inlet plane of IFRF furnace simulation showing the primary RFG inlet (light blue), secondary and tertiary RFG + O_2 inlets (red), and natural gas inlets (blue).

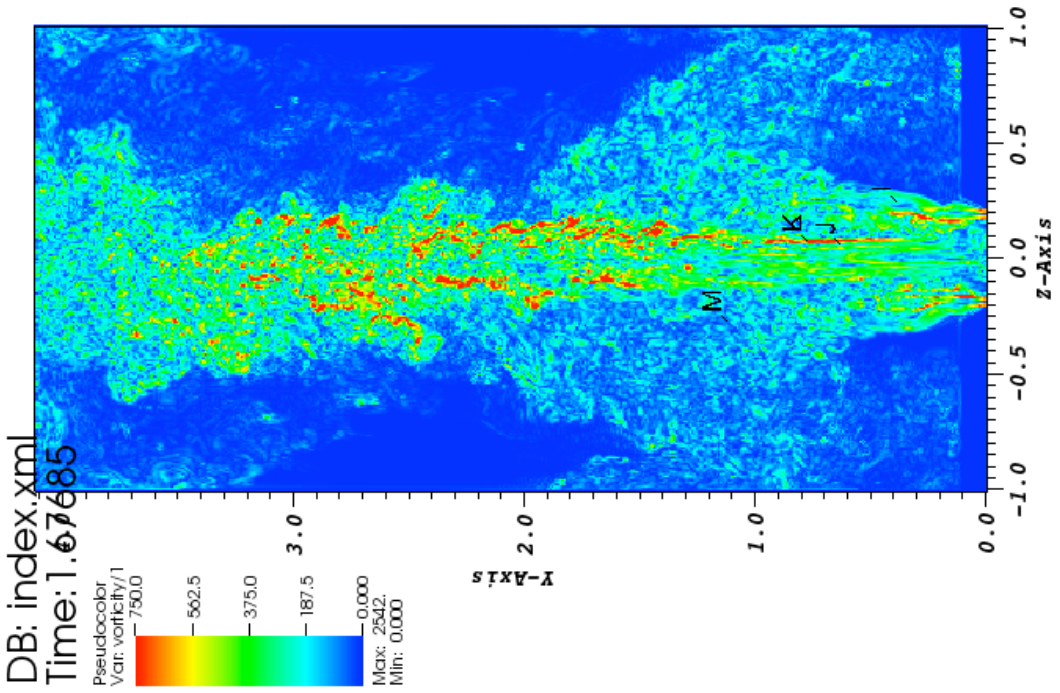

Figure 4: Side view of vorticity field at the furnace centerline showing the size of the computational domain and the burner quarl (dark blue area on right side of figure).

Additional software development was required to perform ARCHES simulations with swirl and to more accurately predict NO_x chemistry. In this quarter, Subtask 3.2 researchers added a swirl model and a thermal NO_x model to ARCHES. Some bugs with respect to the furnace wall boundary condition were also fixed. All new models underwent a thorough verification process.

V/UQ Framework

The third project task was to apply a V/UQ framework to the IFRF oxy-gas experiments and simulations. The framework proposed by Bayarri et al. (2005) was chosen for this project. This framework includes the following six steps:

- Input/uncertainty map
- Determine evaluation criteria
- Data collection
- Model approximation
- Analysis of model output
- Feedback/feed forward

The first three steps are described in detail in this preliminary report; the last three steps will be covered in the project's final report.

Input/Uncertainty Map

The first step, the input/uncertainty (I/U) map, requires the specification of model inputs and parameters with associated uncertainties of ranges. As noted by Bayarri et al. (2005), "This step requires considerable subject-matter expertise to help set priorities among a (possibly) vast number of inputs as well as specify uncertainties, often as prior distributions of inputs. As information is acquired through undertaking further steps of the validation process, the I/U map is revisited, revised and updated." The map includes a list of model, scenario, or numerical parameters of potential importance to the outputs of interest in the simulation; a ranking of the importance of each input based on prior experience and/or information provided by the experimentalists; and the uncertainty or distribution range for each input. The I/U map is dynamic; attributes such as the relative importance of a parameter and its uncertainty may change or require updating during the validation process.

The I/U map for the oxy-gas IFRF furnace simulations is shown in Table 1. The parameters are grouped by type. Parameter selection for the experimental design is focused on those model, scenario, and numerical parameters that have the potential to most influence the output variables of interest (species composition, temperatures, etc; see "Evaluation Criteria" section). For example, the composition field is affected by the choice of chemistry/mixing model (model parameter), preliminary simulations indicate the importance of burner geometry in capturing near-burner species concentration and temperature fields (scenario parameter), and the fidelity of the simulation results depend on whether or not the relevant time/length scales are captured by the resolution of the computational domain (numerical parameter). The parameter impact ranking is on a

scale of 1-5 where 1 indicates a parameter likely to have only a minor impact on the prediction error and 5 indicates a parameter with significant potential impact.

Table 1. I/U map for simulations of the oxy-gas fired IFRF furnace.

Parameter	Impact Ranking	Uncertainty	Current Status
Model			
Reaction/mixing model	1	Equilibrium, equilibrium with mixing model, flamelets, flamelets with mixing model, scale separation	Base case uses equilibrium for major species of combustion, no mixing model, no scale separation
No. of ordinate directions in DO radiation model	3	S2, S4, S6, or S8	Using S4 in base case
Thermal NO_x model	1	Unknown	Using kinetic rate derived from Bowman, 1975
Scenario			
O_2 flow rate	1	Unknown	Small fluctuation of O_2 flow rate has big influence on O_2 & CO_2 concentrations; base case uses flow rate given in input table
Air in-leakage in RFG stream	2	Estimated from mass balance at 268 kg/hr	Base case assumes rate of 199 kg/hr
Swirl no. of tertiary oxidant stream	2	Unknown	Swirl palettes inclined at 30°, located at burner exit; no way to determine swirl no. Base case uses value of 0.5

Parameter	Impact Ranking	Uncertainty	Current Status
Area of secondary & tertiary streams in burner exit plane	2	Unknown	Controlled by damper, no indication of what relative flow rates are. Base case arbitrarily chosen
Wall boundary condition	4	$\pm 10^{\circ}C$	Wall temperature along length of furnace measured by thermocouple located 1 cm in from refractory face; use average value of 1350K for base case
Natural gas flow rate	1	Unknown	Small fluctuation of nat. gas flow rate has big influence on O_2 & CO_2 concentrations
Primary inlet geometry	3	Four rectangular openings or central tube	Assumed 4 rectangular openings for base case
Numerical			
Mesh resolution	3	Unknown	Using finest mesh possible within constraints of available computers

Evaluation Criteria

The second step is to determine the evaluation criteria based on the context in which the model (e.g. simulation) is used, the feasibility of obtaining both experimental and simulation data, and the evaluation methodology. It is possible that the model may pass for some evaluation criteria and fail for others. In fact, as noted by Bayarri et al. (2005), "...initially stated criteria will typically be revisited in light of constraints and results from later analyses."

The initial evaluation criteria for the IFRF oxy-gas experiments are focused on determining how closely species concentration (specifically NO_x, CO_2, and O_2) and temperature fields computed in the simulation reproduce those same fields measured experimentally, where data have been tabulated at specific axial and cross-sectional locations in the IFRF furnace (Coraggio and Laiola, 2009). These output variables were

chosen for the evaluation criteria based on the following rationale. First, NO_x concentration is of most interest to companies who are considering alternative combustion technologies because the U.S. Environmental Protection Agency is promulgating new NO_x regulations. Second, while the interest in oxy-firing for CO_2 capture waned in the past year due to the lack of any clear direction at the federal level on CO_2 regulation, there are indications that the politics are once again shifting toward an interest in regulation. In that case, combustion efficiency and CO_2 levels in the flue gas as measured by relative concentrations of CO_2, CO, and O_2 are important. However, because of problems encountered in measuring CO as described by Coraggio and Laiola (2009), the CO data set was excluded from the evaluation criteria. Third, local temperature fields determine radiant heat transfer, which is another important consideration when applying oxy-gas firing as a retrofit technology. Also, temperatures were measured experimentally with a suction pyrometer and a detailed analysis of probable error was provided in a follow up study by Parente et al. (2010), making this a desirable output variable for V/UQ analysis.

Data Collection/Design of Experiments

Data from both simulation and physical experiments are essential for the V/UQ analysis, including assessing bias and uncertainty in model predictions and studying the sensitivity of a model to inputs. Ideally, the experiments are conducted in tandem as "...The iterative and interactive nature of the validation and development processes will result in multiple stages of computer experiments and even field experiments..." (Bayarri et al., 2005). However, in many cases such as this project, the experimental data have already been collected and published in the literature. In this situation, researchers performing the computationally-expensive simulations must utilize a careful design of experiments to maximize data collection while minimizing computational cost. This design of experiments needs to cover the ranges of key input values using space-filling strategies. Previously, experimental designs such as Box-Behnken and Face-Centered Composite Designs have been used. Recent work in the Institute for Clean and Secure Energy has instead focused on triangular-linear interpolation for low-dimensional cases (e.g. 2-3 active variables). The advantages of this design include that it is well-behaved, every point is hit, it is flexible for additional points, and queried points never go above the values of points used for interpolation.

Before this design can be employed, however, the list of parameters in Table 1 must be reduced to a set of 2-3 active variables that have a first order effect on the output variables of interest (e.g. the evaluation criteria). To determine the active variables, a suite of seven simulations of the IFRF's oxy-gas experiments has been completed. The purpose of these simulations is to test the sensitivity of output variables of interest (CO_2/O_2/NO_x concentrations and gas temperature) to various model and scenario parameters in order to identify both what the 2-3 active variables should be and the range of values that should be considered for each variable.

The base case simulation assumes a wall temperature of 1350 K, a swirl number in the burner's tertiary oxidant flow of 0.5, air leakage into the RFG stream of 199 kg/hr or

12.7% of the overall RFG stream, complete water removal in the RFG stream, and flow rates of O_2 and natural gas as reported by Coraggio and Laiola (2009). Based on uncertainties noted by the authors and/or the lack of availability of detailed burner information, the following parameters were varied for the sensitivity study:

- Air in-leakage into RFG is increased to 268 kg/hr
- Increase O_2 addition to the RFG stream by 10%
- Wall temperature increased from 1350K to 1450K
- Split of RFG + O_2 stream between the secondary and tertiary inlets is scaled by the available exit surface area
- Increase natural gas flowrate by 5%
- Decrease the swirl number to 0.1

Experimental measurements were taken from the wall to the furnace centerline at six axial locations along the length of the furnace. Five of those axial locations are within the domain size of the simulation and are used for data analysis. Coraggio and Laiola (2009) note that "...the measurements obtained with the suction pyrometer are an average of the value of the temperature (or gas composition) on a region inside the furnace centred in the measurement point. On the basis of experimental experience this region is assumed to have a radius of 2.5 cm." They consider this assumption to be very conservative. In order to compare with the measured data, simulation data from a 2.5 cm box around the measurement point was extracted and both spatially- and time-averaged in the results that are presented below. Matlab scripts were written to perform this extraction and averaging process.

In the series of figures that follows, comparisons are shown between temperature, CO_2, O_2, and NO_x simulation and experimental data at various axial locations for the base case and the six additional cases described above. Where an estimate of the measurement error was provided by the authors, experimental error bars are included on the plots. However, in most cases the authors only considered instrumental error and did not assess either bias error nor replication error, so these error bars are most likely much larger.

Figures 5-8 show temperature plots at all five axial locations. Because of scripting and/or extraction problems, some figures are missing error bars and Figure 8 is missing data from three of the cases. Nevertheless, some observations can be made. First, simulation temperatures near the wall are consistently low compared with the experimental data over the range of parameter space tested in this sensitivity study. This result indicates a need to expand the parameter space to include either a wider range of the variables tested or to include another variables. This issue is addressed in the "Future Work" section below. Second, the simulation results bracket the experimentally-measured temperature range in the middle of the furnace, so parameter space expansion is not required for these data. Third, changing the swirl number and the secondary/tertiary flow rate split has strong effects on the temperature profiles near the burner.

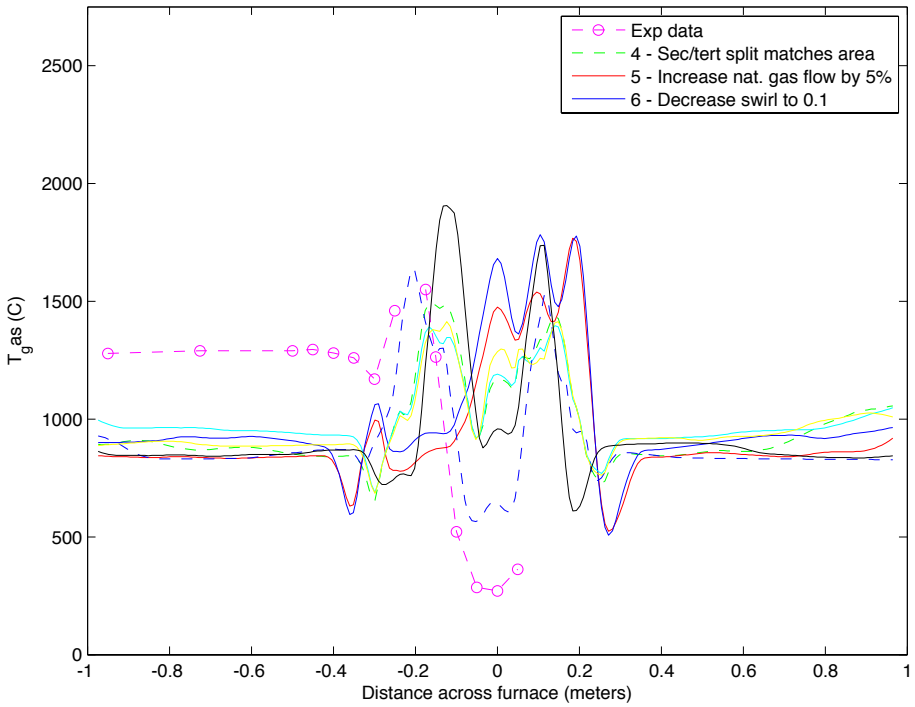

Figure 5: Temperature profile across the IFRF furnace, 0.17 m from the burner face. Error bars and complete legend are missing from this plot; see the legend for Figure 6.

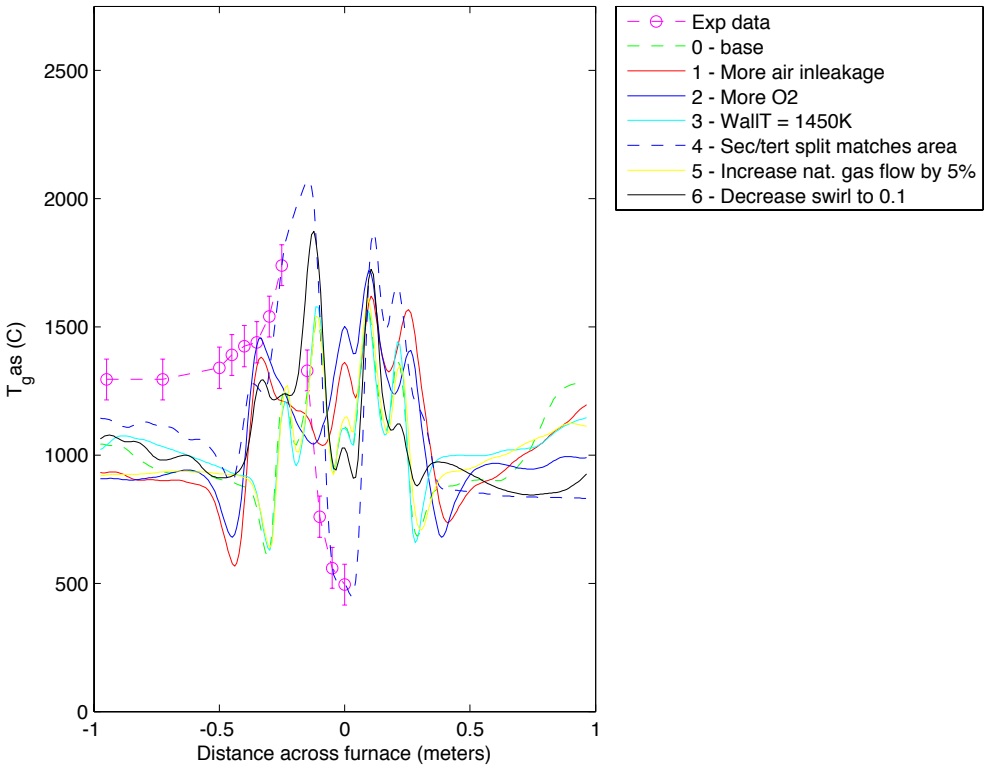

Figure 6: Temperature profile across the IFRF furnace, 0.46 m from the burner face.

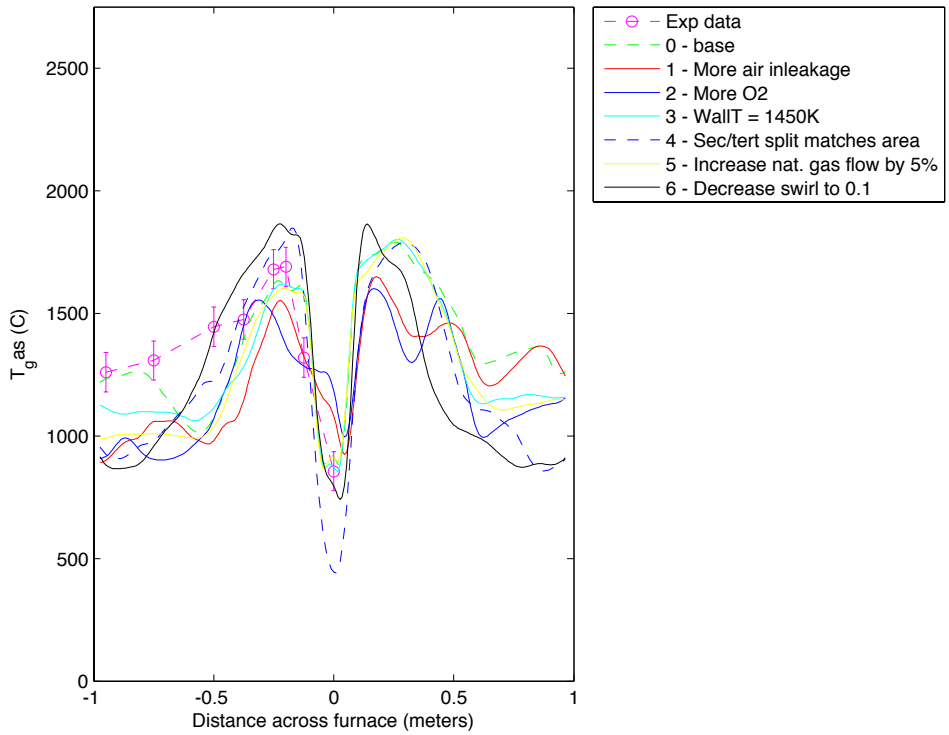

Figure 7: Temperature profile across the IFRF furnace, 1.04 m from the burner face.

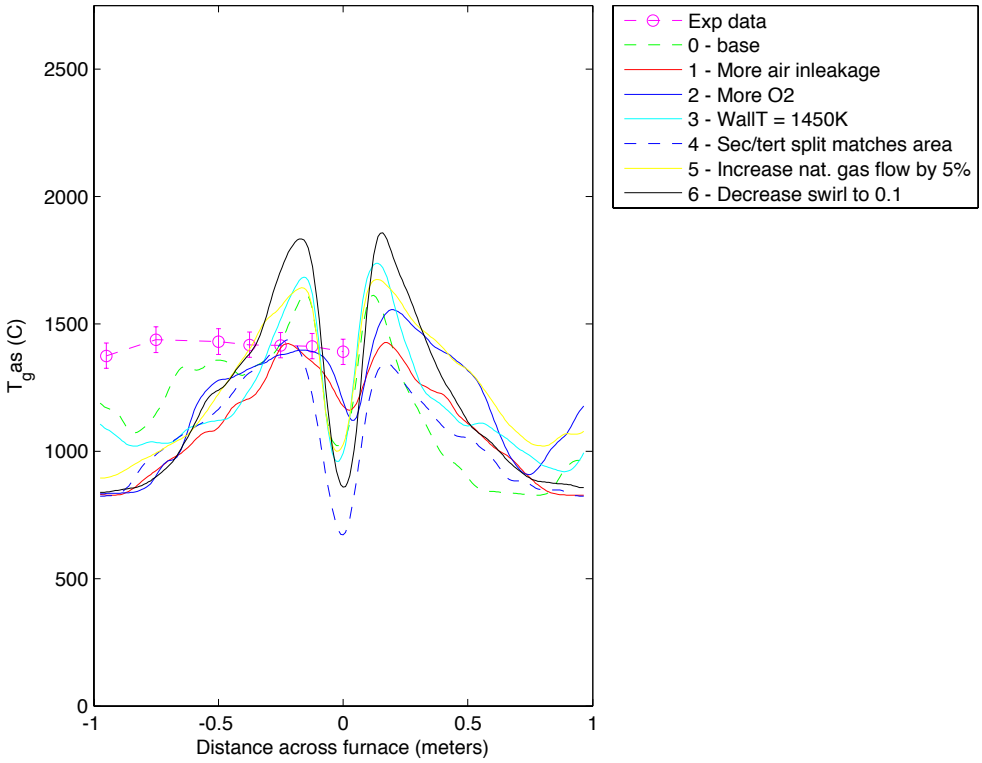

Figure 8: Temperature profile across the IFRF furnace, 1.62 m from the burner face.

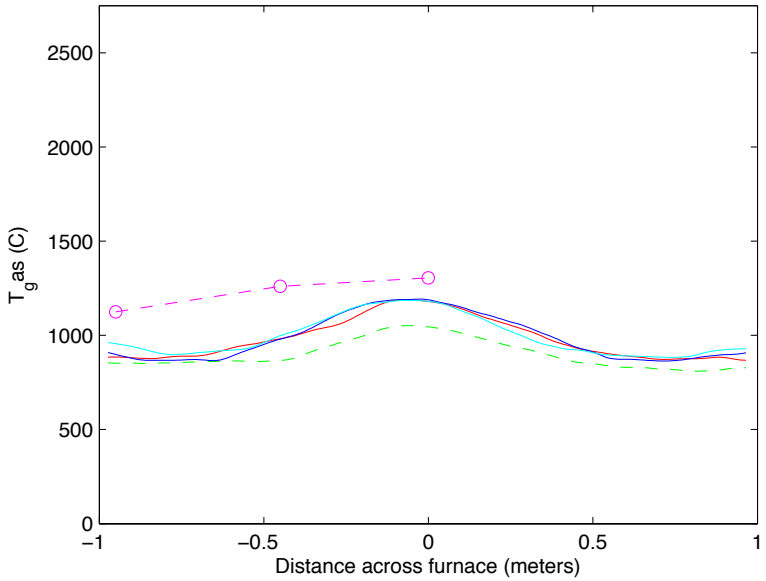

Figure 9: Temperature profile across the IFRF furnace, 3.84 m from the burner face. Error bars, a legend, and results from the last three cases are missing from this plot; see the legend for Figure 8.

Figures 10-12 show CO_2 plots at three axial locations; plots were not obtained at all axial locations due to data extraction problems. The CO_2 concentration profiles are consistently low, especially in regions near the furnace wall. These results indicate that the parameter range spanned (air in-leakage, O_2 concentration in the RFG, and/or natural gas feed rate) need to be adjusted in the V/UQ study such that a drop in CO_2 concentrations is achieved. The trends in experimentally-measured CO_2 concentration across the furnace are matched by the simulation data, giving researchers some confidence that some parameter changes will yield results in range of uncertainty of the data (assuming that the range is expanded for reasons stated previously in this report).

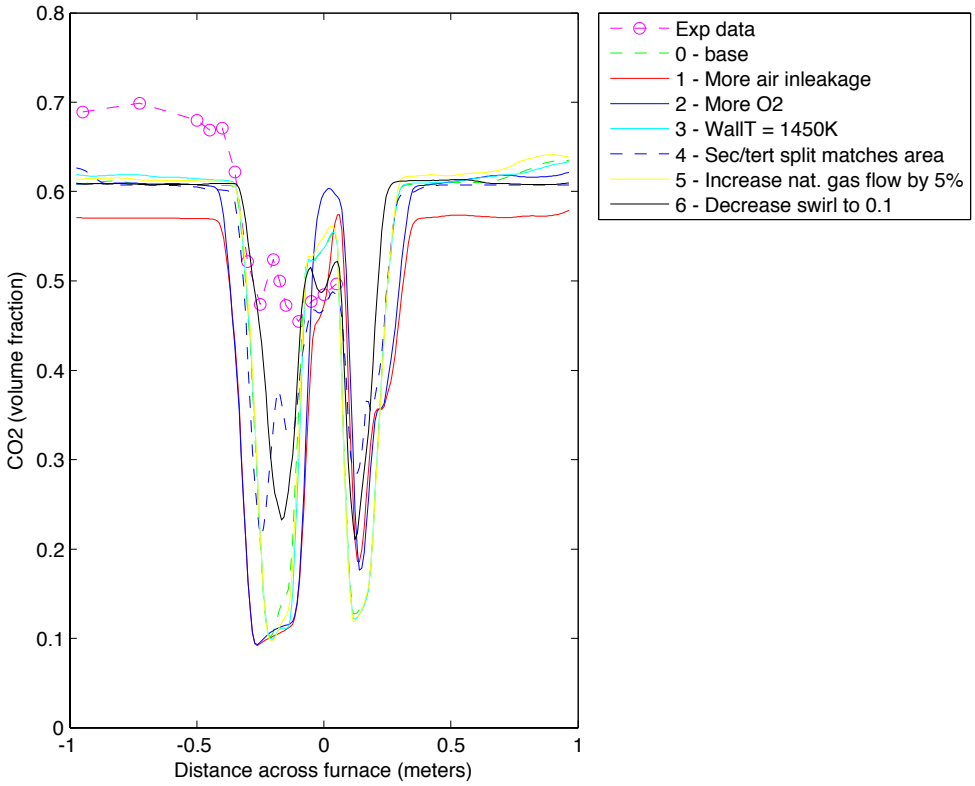

Figure 10: CO_2 profile across the IFRF furnace, 0.17 m from the burner face.

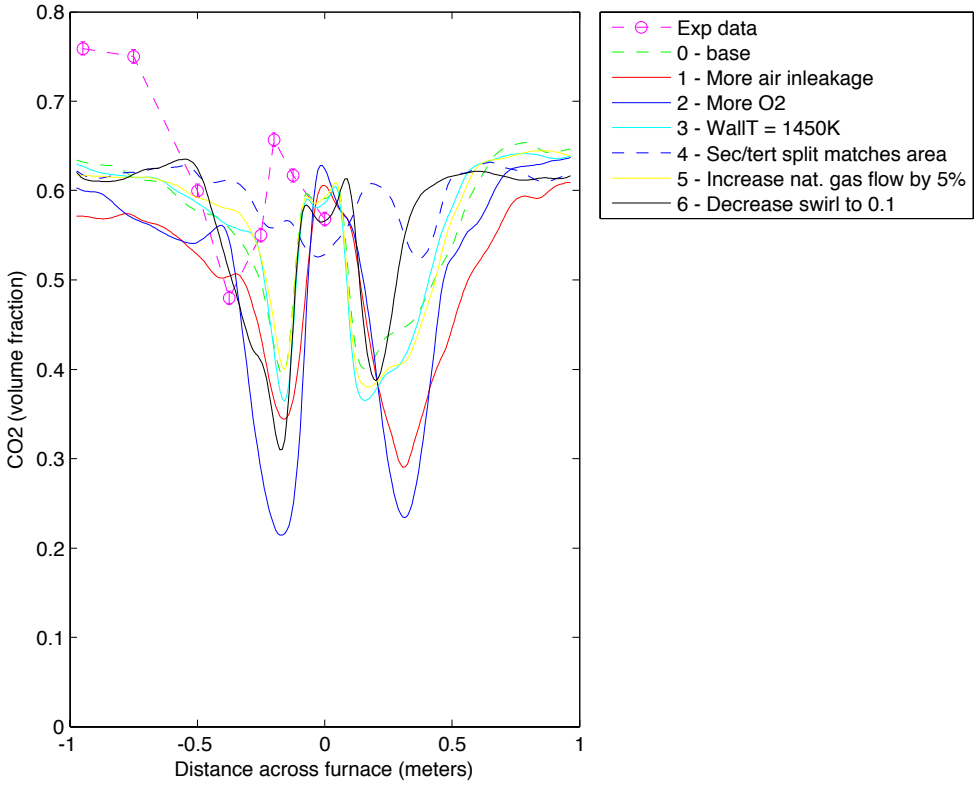

Figure 11: CO_2 profile across the IFRF furnace, 1.04 m from the burner face.

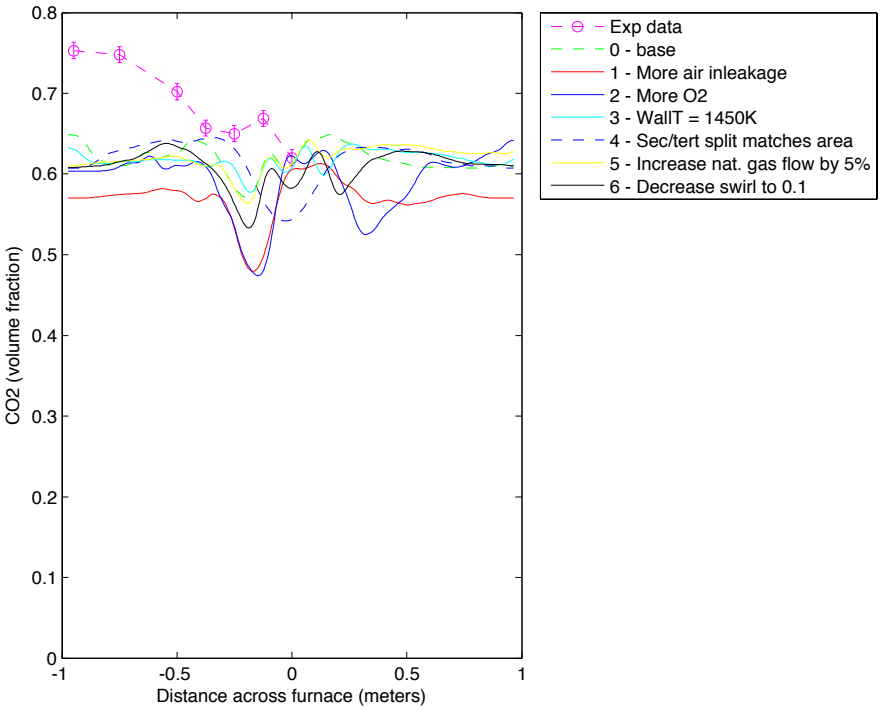

Figure 12: CO_2 profile across the IFRF furnace, 1.62 m from the burner face.

Figures 13-15 show O_2 plots at three axial locations; plots were not obtained at all axial locations due to data extraction problems. In regions near the wall where CO_2 concentration profiles are too low, the corresponding O_2 concentration profiles are consistently high, so adjustments in the parameter ranges and/or additional parameters need to be tested. However, in the center of the furnace the experimental data are spanned by the simulation results. Overall, the experimentally-measured O_2 profile across the furnace is matched by the simulation data. As with temperature, the O_2 concentration profiles in the near-burner regions are markedly different when the swirl number and secondary/tertiary flow rate split are changed.

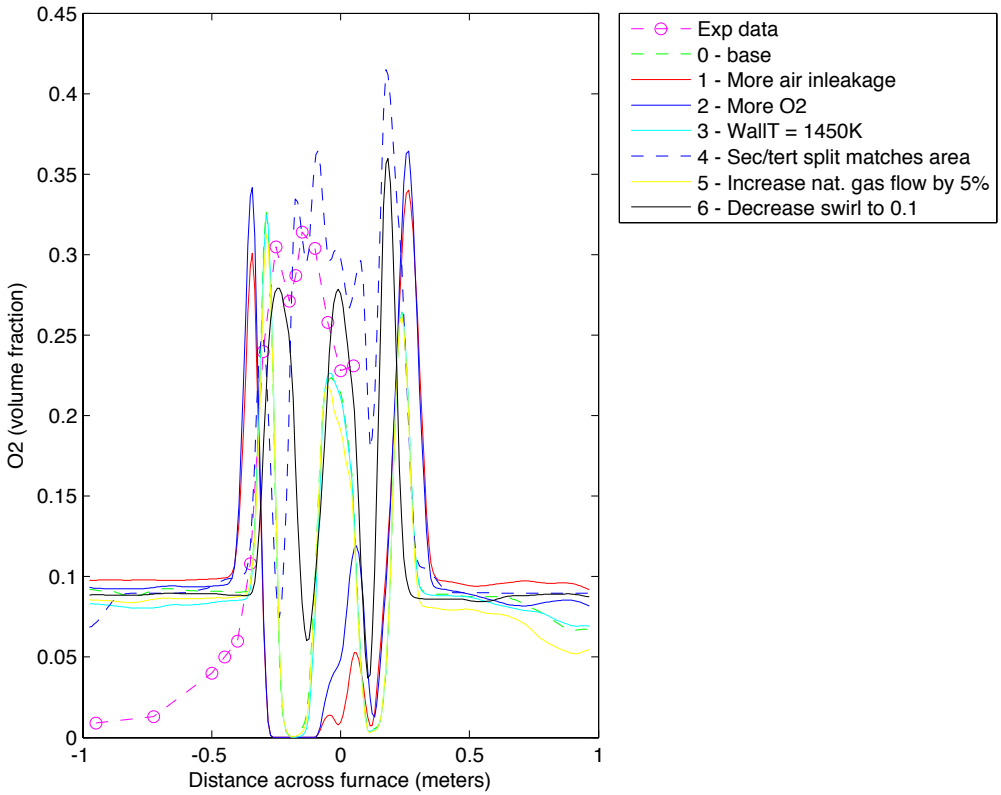

Figure 13: O_2 profile across the IFRF furnace, 0.17 m from the burner face.

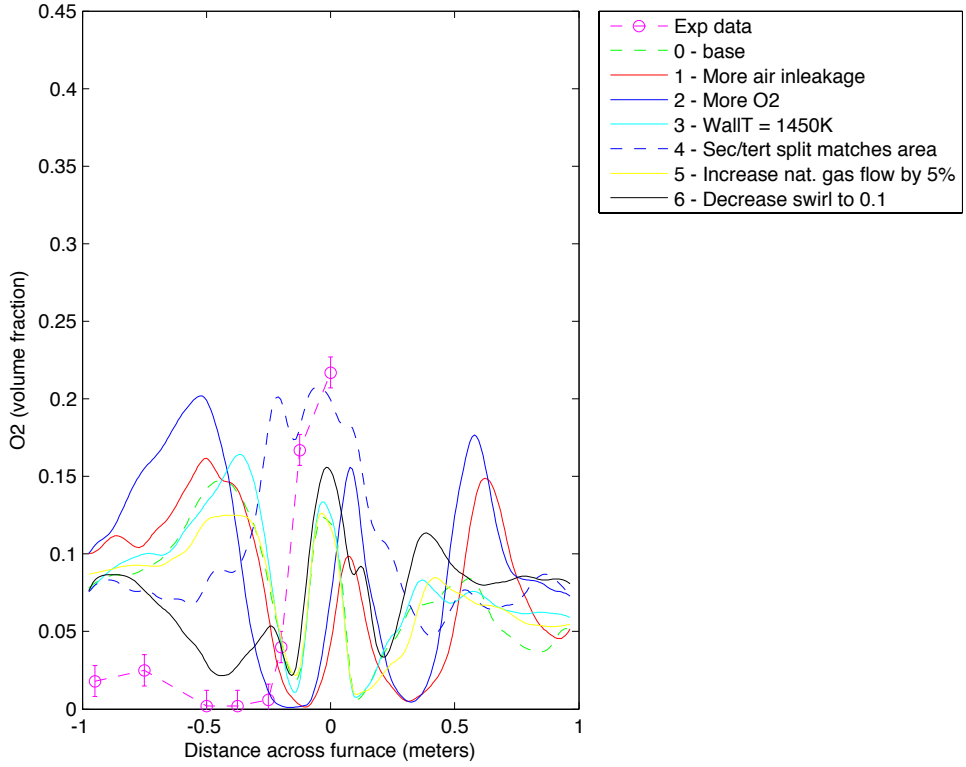

Figure 14: O_2 profile across the IFRF furnace, 1.04 m from the burner face.

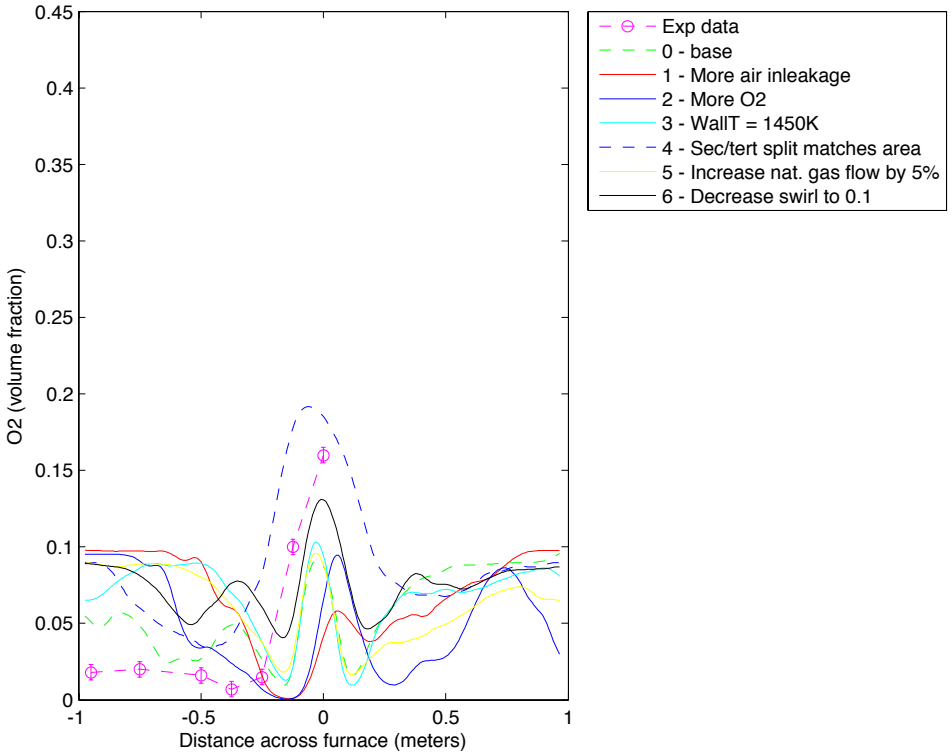

Figure 15: O_2 profile across the IFRF furnace, 1.62 m from the burner face.

Figures 16-18 show NO_x plots at three axial locations; plots were not obtained at all axial locations due to data extraction problems. The plot at an axial distance of 3.84 m shows time-averaged but not spatially-averaged data. That is, only time-averaged data at the measurement points are presented. The NO_x concentrations computed in the simulations at axial locations of 0.17 m and 1.04 m are up to an order of magnitude higher than the experimental data while at 3.84 m, simulation and experimental data are in the same range. In the simulation, thermal NO_x is the only NO_x formation mechanism, so the NO_x production rate is a function of the local N_2 and O_2 concentrations as well as the gas temperature. Availability of N_2 and O_2 in the near burner region for the cases with enhanced air in-leakage and increased O_2 feed rate appear to be driving high NO_x levels. Farther down the furnace (1.04 m), the cases with decreased swirl number and a secondary/tertiary flow rate split based on flow area show highly elevated levels of NO_x formation. Analysis is ongoing to determine the root causes of these discrepancies so that the parameter space can be adjusted for the V/UQ analysis.

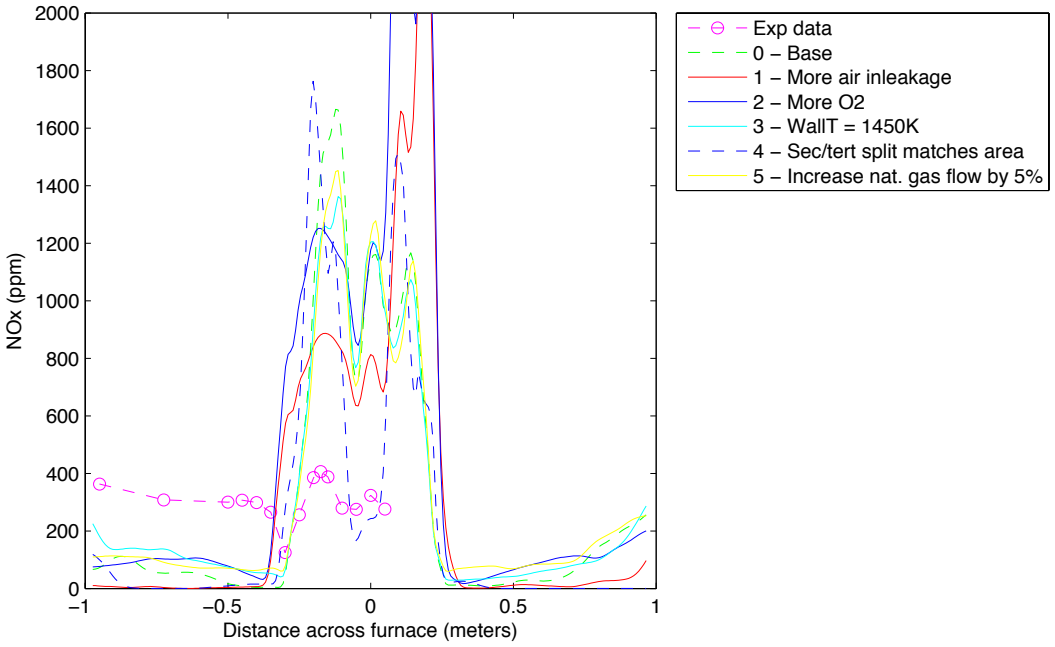

Figure 16: NO_x profile across the IFRF furnace, 0.17 m from the burner face.

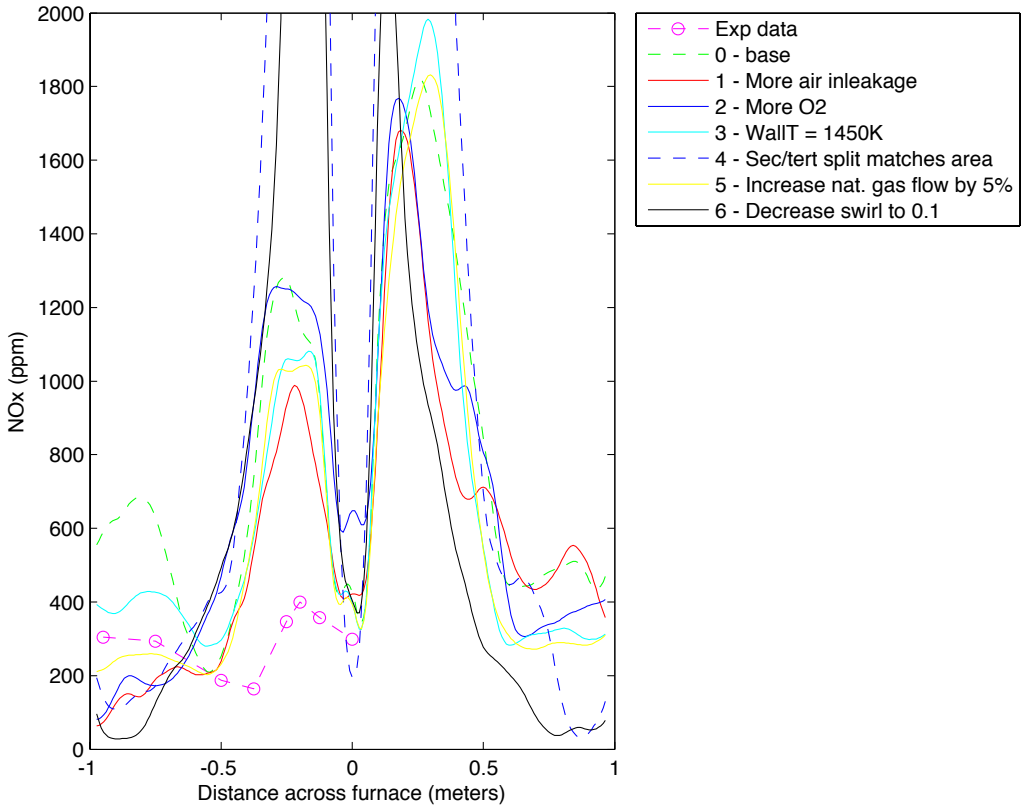

Figure 17: NO_x profile across the IFRF furnace, 1.04 m from the burner face.

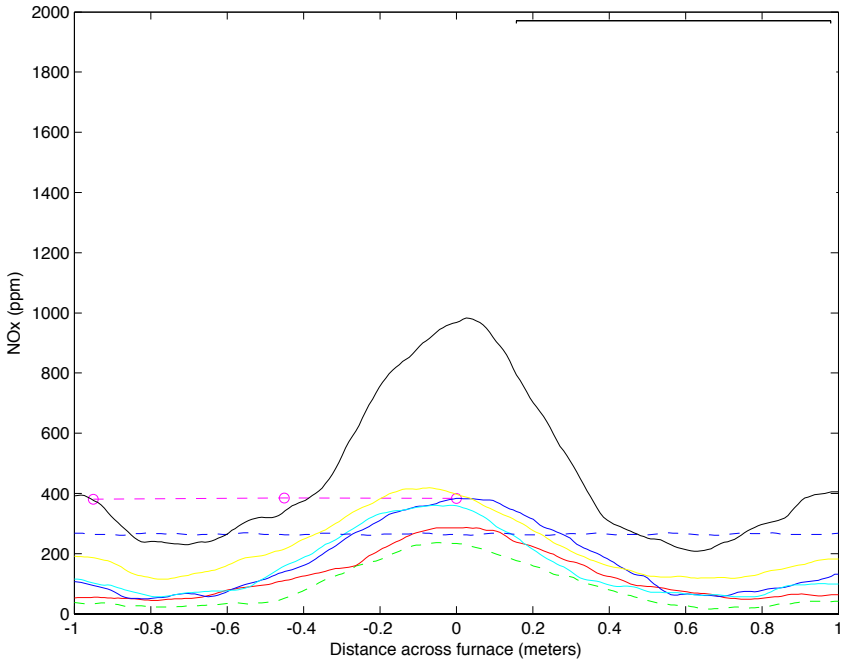

Figure 18: NO_x profile across the IFRF furnace, 3.84 m from the burner face. Simulation data is only time-averaged (not spatially-averaged). The legend is the same as in Figure 17.

Future Work

Based in this first suite of simulations, it is clear that some of the data will pass the evaluation criteria while other data will not. The project team believes that the equilibrium reaction models used to compute the oxy-gas combustion chemistry for the simulation results presented in this report are not adequate for these types of systems. Rather, scale separation of the reaction chemistry with slow reactions solved on the mesh and fast reactions solved at the subgrid scale is essential. Hence, recent Arches software development work has focused on creating a mechanism for scale separation within the simulation framework. Additional development work on a new flamelets-based mixing/reaction model for subgrid scale combustion chemistry is also nearing completion. With these tools in hand, several additional simulations will be performed so that the number of parameters can be narrowed to 2-3 active variables and the appropriate parameter space for the V/UQ analysis determined.

References

Bayarri, M. J., J. O. Berger, J. O., Paulo, R., Sacks, J., Cafeo, J. A., Cavendish, J., Lin, C. H. & Tu, J. (2005, April). A framework for validation of computer models (Technical Report Number 162. Research Triangle Park, NC: National Institute of Statistical Sciences.

Coraggio, G. & Laiola, M. (2009). *Combustion of NG and pulverized coal in a mixture of oxygen and RFG* (IFRF. Doc. No F110/y/01). Pisa, Italy: International Flame Research Foundation.

Coraggio, G., Tognotti, L., Cumbo, D., Rossi, N. & Brunetti, J. (2011). Retrofitting oxy-fuel technology in a semi-industrial plant: Flame characteristics and NO_x production from a low NO_x burner fed with natural gas. *Proceedings of the Combustion Institute*, *33*, 3423–3430.

Lallemant, N., Dugue, J. & Weber, R. (1997). Analysis of the experimental data collected during the OXYFLAM-1 and OXYFLAM-2 experiment, Phase 1: 1995-1996. IFRF Doc No F 85/y/4, International Flame Research Foundation, IJmuiden, The Netherlands.

Parente, A., Coraggio, G., Galletti, C. & Tognotti, L. (2010). *Verification, validation and uncertainty quantification in industrial combustion modelling: some practical tools* (IFRF Doc. No G25/y/01). Livorno, Italy: International Flame Research Foundation.

Tognotti, L. (2007, June). *IFRF status and planned activities*. Paper presented at the International Flame Research Foundation Members Conference, Pisa, Italy.

Three-Dimensional Structure of the Siskin Green River Oil Shale Kerogen Model: A Comparison between Calculated and Observed Properties

Anita M. Orendt,[1] Ian S.O. Pimienta,[1,2] Shyam R. Badu,[1] Mark S. Solum,[3] Ronald J. Pugmire,[4] and Julio C. Facelli[1,5]

[1]Center for High Performance Computing and [3]Departments of Chemistry, [4]Chemical and Fuels Engineering, and [5]Biomedical Informatics University of Utah, Salt Lake City, Utah 84112

[2]Department of Chemistry and Physics, Troy University, Troy, Alabama 36082

Darren R. Locke,[6] Karena W. Chapman,[6] Peter J. Chupas,[6] and Randall E. Winans[6]

[6]X-ray Science Division, Advanced Photon Source, Argonne National Laboratory, 9700 S. Cass Avenue, Lemont, Illinois 60439

Abstract

Three-dimensional (3D) structural models of the Green River kerogen based on the two-dimensional (2D) structure proposed by Siskin were generated using a combination of *ab initio* and molecular mechanics calculations. Several initial monomer conformations were generated using the simulated annealing procedure, followed by minimization via quantum mechanical calculations. ^{13}C solid state nuclear magnetic resonance (SSNMR) spectra and atomic pair distribution functions (PDFs) were calculated based on these 3D models and compared to experimental results obtained on a Green River kerogen sample. The results show reasonably good agreement between calculated and experimental results.

Introduction

Kerogen is defined as the insoluble organic component of the organic matter in sedimentary rocks. This organic matter is usually mixed with minerals during its deposition which contributes to the difficulty in its physical isolation. Kerogen is not soluble in normal organic solvents because of the large molecular weight up to several thousand Daltons.[1–4] Kerogen is found in rocks such as shale, as oil shale deposits and when heated in the Earth's crust, some types release hydrocarbons in the form of crude oil or natural gas.

As kerogen is a mixture of organic material, its chemical composition varies from one sample to another. According to the van Krevelen diagram, kerogens can be classified based on the ratios of H/C and O/C.[5] Type I kerogens have H/C ratio greater than 1.25 and O/C ratio less than 0.15. This class is derived primarily from cyanobacteria or various Chlorophyta and dinoflagellates. Type II kerogens, derived from marine planktonic organisms, have H/C ratio less than 1.25 and O/C ratio of 0.03 to 0.18. Type II kerogens can be enriched in organic sulfur; in this case they are further classified as belonging to Type IIS kerogens. Type III kerogens are derived primarily from higher plant remains in coals and coaly shales; they possess a low hydrogen count (H/C < 1, O/C ≡ 0.03–0.3) because of the extensive ring and aromatic character in these systems. Finally, type IV kerogens are comprised of mostly polycyclic aromatic hydrocarbons with H/C ratio less than 0.5.

Source rocks in the Green River formation, one of the most extensive oil shale reserves in the world, contains hydrogen-rich algal kerogen (type I) with up to ~20 wt% organic matter in the form of amorphous kerogen solid integrated in a silicate- and

carbonate-based mineral matrix.[6,7] In the past few years, investigators have employed different methods to separate organic kerogen from inorganic minerals in oil shales and to recover the unaltered kerogen for characterization studies.[8–10] Although considerable progress has been achieved from these studies, the complete isolation of kerogen from oil shales remain difficult.

In the case of these petroleum precursors, e.g., source rocks and the kerogens, little information is presently available to describe their physical behavior.[11] Only a few relevant studies utilizing both chemical and instrumental analysis to reconstruct a stochastic two-dimensional model of kerogens have been published.[12-17] The work of Durand and co-workers dealt with type I and type II kerogens.[12] More recently, two-dimensional (2D) models of kerogen have been proposed by Siskin[13] for type I Green River Oil Shale (GROS) and Lille[14] for kukersite (a type II/I kerogen). A much larger (more than 10^4 core structures with approximately 10^6 atoms), more general 2D kerogen model[17] has also been developed using the data from various solid state analyses to construct the cores; this model has been used to predict oil and gas compositional yields.

A potential solution to aid in the isolation of kerogen is the analysis of its three dimensional (3D) molecular structure using molecular modeling and simulation. Atomistic modeling is routinely used in many industries (pharmaceutical, polymers, coatings, explosives, membrane proteins, etc.) to gain insight to material properties and behavior. Faulon[15-16] reported some preliminary data on 3D structures of kerogen but there has been a lack of modeling work that utilizes the molecular modeling tools that are available today. Hence, little is known about the 3D characteristics of any of the kerogen models. The 3D characteristics of kerogen will not only define the manner in which the

kerogen folds and interacts with both the extractable bitumen and the mineral matter, but the structural information will provide a new view of the structure including information on which portions of the structure are exposed on the surface, which portions are accessible through channels, and/or which portions may be isolated in the interior of the structure. An understanding of where the various functional groups are located may serve as useful guides for developing novel processing schemes for resource recovery. In addition, the surface exposure of polar functional groups will provide new information on the interaction of the kerogen structure with the inorganic matrix that appears to bind tightly to the mineral matter.[18-21]

In this work, the 3D structure of the Green River Siskin model[13] was obtained using a combination of *ab initio* and molecular mechanics calculations. The 3D structure was then used to calculate the ^{13}C chemical shifts, from which a simulated ^{13}C spectrum can be generated, as well as to simulate the expected atomic pairwise distribution function (PDF). The PDF gives the probability of finding an atom at a given radial distance from another atom; the peaks observed correspond directly to interatomic distances within the sample and is suitable for this study as it provides local structural information independent of long-range order.[22,23] In addition, ^{13}C solid state NMR (SSNMR) is a powerful tool to obtain structural information on insoluble samples such as kerogens. Using the methodology developed by Grant and Pugmire[24,25] and used extensively on fossil fuel samples, SSNMR ^{13}C spectra can be analyzed to provide detailed structural data such as the average aromatic cluster size and the average number of substituents on the clusters.

The ^{13}C SSNMR spectrum and PDF simulated using our model are compared with their experimental counterparts on the kerogen extracted from a segment of a Green River basin shale core.[26] The comparison of the simulated and experimental properties allows for an evaluation of the quality of the 3D model as well as the underlying 2D one. The existence of a 3D model that has been validated against experimental data will allow for further computational study on the interaction between the kerogen and the mineral matrix as well as on the further processing of the kerogen for oil production.

Computational and Experimental Details

Generation of 3D Model: A 3D structure corresponding to the 2D Siskin's kerogen model[13] (chemical formula of $C_{645}H_{1017}N_{19}O_{17}S_4$; molecular weight of 9438.35 g/mol) was built using HyperChem.[27] A preliminary chemical structure was obtained via the molecular mechanics energy minimization routine in HyperChem using the MM+[28] force field. This minimized structure was further optimized using the *ab initio* software package GAMESS[29] at the restricted Hartree-Fock (RHF) level of theory using the minimal STO-3G[30] basis set.

After a minimum energy structure was identified by the above procedure, this structure was used to initiate a series of molecular mechanics calculations, using simulated annealing[31] to generate several monomer conformations. This procedure involves three steps: heat, run, and cool. The first step was completed using simulation period of heat time (0.1 ps) and a starting temperature of 10 K to set initial velocities with rescaling of velocities at temperature increments of 119 K per 0.01 ps to reach the simulation temperature of 1200 K. In the second step, the velocities are rescaled at a

constant temperature of 1200 K for a run time of 0.5 ps. The final step was the simulation period of cool time (1 ps), with rescaling of velocities at temperature increments of 9 K per 0.01 ps to reach the final temperature of 300 K. The process was repeated until four monomer conformations were obtained from the parent.

Each of these generated conformers was then locally optimized using GAMESS at the RHF/STO-3G level of theory in the same manner as the original 3D structure. The energies of these structures were compared and the structure with the overall minimum energy was then chosen as the "parent" for the next simulated annealing cycle. The lowest energy conformation obtained in the second annealing cycle was used in the simulation of the PDF and NMR spectra. Molecular images were generated using Mercury.[32]

Calculation of ^{13}C Chemical Shielding: The NMR calculations were done using the density functional theory approach with the PBE1PBE[33] exchange correlation functional and using the 4-31G basis set[34] as implemented in Gaussian09 suite of programs.[35] The calculated chemical shielding values were converted to chemical shifts on the tetramethylsilane (TMS) scale using the shielding calculation of methane at the same level of theory, 200.5 ppm, adjusted by -7 ppm which is the chemical shift of dilute methane on TMS scale.[36] Gaussian broadening of 2 ppm along with Lorentzian broadening of 1 ppm was applied on the aliphatic region, with 5 ppm Gaussian broadening used in the aromatic region to obtain the simulated SSNMR spectrum.

Calculation of Atomic PDF: The PDFs were calculated using DISCUS and plotted using KUPLOT, both part of the DIFFUSE[37] suite of packages. Atomic coordinates of the model were used to calculate a PDF using the following equation

$$G(r) = \frac{1}{r}\sum_{\nu}\sum_{\mu}\frac{f(0)_{\nu} f(0)_{\mu}}{\langle f(0)\rangle^2}\delta(r - r_{\nu\mu}) - 4\pi r\rho_o \qquad (1)$$

where r is the radius, δ is the Dirac delta function, ρ_o is the average number density of the kerogen , $f(0)_{\nu}$ and $f(0)_{\mu}$ are the x-ray atomic form factors for atoms ν and μ while $<f(0)>^2$ is the square of the average x-ray atomic form factors. The sum goes over all pairs of atoms ν and μ within the model separated by $r_{\nu\mu}$. The subtraction of $4\pi r\rho_o$ from the G(r) in the above equation leads to the function being equal to zero at large radial distances. While this equation applies for infinite materials with homogenous density confined within well-defined boundaries, kerogen models are finite with irregular shapes and cannot be bound in any way to avoid void space within the boundaries. This leads to a lower average density for the bound model which presents a problem when calculating the pair distribution function using the above equation. To correct for this effect, a modified term is used to describe the shape and size of the kerogen model. The modified equation that allows adjustments for model shape and size, which can be derived from Eq. 4 in the paper of Neder and Korsunskiy,[38] is as follows:

$$G(r) = \frac{1}{r}\sum_{\nu}\sum_{\mu}\frac{f(0)_{\nu} f(0)_{\mu}}{\langle f(0)\rangle^2}\delta(r - r_{\nu\mu}) - 4\pi r\rho_o \tanh(S(R-r)) \qquad (2)$$

where S is related to the model shape and R the model diameter.

Sample Details: As mentioned in the introduction, experimental data was obtained on a kerogen extracted from a segment of a Green River basin shale core.[26] An elemental analysis of the kerogen sample used gave an approximately 5% mineral matter content and an atomic composition of $C_{100}H_{150}N_3O_8S_1$ for the organic content. This can be compared to the atomic composition of the Sisken model ($C_{645}H_{1017}N_{19}O_{17}S_4$ or

$C_{100}H_{157.7}N_{2.9}O_{2.6}S_{0.6}$); the only large difference is that the kerogen sample used has a higher oxygen content.

Measurement of Atomic PDF: Measurement of the atomic pair distribution function for a powdered (100 mesh) demineralized Green River kerogen sample[26] was made on instrument 11-ID-B at the Advanced Photon Source (APS), Argonne National Laboratory. High-energy X-rays (60 KeV, λ=0.2128Å) were used with a Perkin Elmer amorphous silicon based detector[40] to collect diffraction data to high values of momentum transfer, Q (Qmax~18Å^{-1}; $Q=4\pi Sin\theta/\lambda$). The 2D diffraction images were processed in Fit2D[37] software to perform x-ray polarization correction and radial integration for peak intensity. Extraction of the experimental pair distribution function from these data was made with PDFgetX2.[41] This software applies corrections to the scattering data for oblique incidence of the x-rays on the image plate, background subtraction, and Compton scattering to produce a structure function, S(Q). The reduced pair distribution function, F(Q) [F(Q)=Q(S(Q)-1)] is Sine-Fourier transformed to yield the atomic pair distribution function, G(r):

$$G(r) = \frac{1}{2\pi}\int_0^\infty Q[S(Q)-1]Sin(Qr)dr \qquad (3)$$

where the transform is truncated at Qmax=18 Å^{-1} due to experimental limitations. The resulting experimental G(r) function yields information on the average bond distances in the kerogen material and can be compared to calculated PDFs of kerogen models. Previously, this approach was shown to provide a reasonable comparison and validation on a coal model.[42,43]

Measurement of ^{13}C solid state NMR: The ^{13}C spectrum of the same Green River kerogen sample used in the PDF measurement was obtained on a Varian Direct

Drive (Oversampled) NMR spectrometer operating at a carbon frequency of 25.152 MHz and a proton frequency of 100.02 MHz. The probe was a Chemagnetics 7.5 mm with a ceramic housing for reduced carbon background. The spinning speed was set at 4100 Hz. The pulse delay was 1 s, which is significantly longer than five times the longest T_1 for the protons. The data was collected using the cross-polarization (CP) method and TPPM[44] decoupling. The contact time was 3 ms which was also more than five times the longest T_{CH} of the aromatic region, as determined from a variable contact time fit[45] of the data. Within the signal to noise ratio differences, the CP spectrum was identical to a single pulse (SP) spectrum. No line broadening was used in this CP spectrum and a total of 146,200 scans were taken.

Results and Discussion

3D Modeling: Our work began with the assumption that the Siskin 2D model of the Green River oil shale kerogen, shown in Figure 1, was the most complete and reliable structural model that was available. This structure was incorporated into the molecular modeling scheme using the general procedure described above. The initial starting point was the 3D structure designated as S1 in Figure 2; this represents the starting point for the folded structure used to begin the search for lower local energy minima structures. The RHF single point energy of this local structure, designated as S1, is –28569.2846 Hartree (1 Hartree = 627.509 kcal/mol).

Following the annealing/optimization process described above using the S1 structure, four additional low energy structures, shown in Figure 3, were identified: S2 (E_{RHF} = –28569.7319 Hartree), S3 (E_{RHF} = –28569.6691 Hartree), S4 (E_{RHF} =

–28570.3721 Hartree), and S5 (E_{RHF} = –28569.9504 Hartree). The lowest energy of these initial five structures, S4, was then used as the parent for another annealing/optimization cycle, generating structures S4-1 through S4-5. These structures are shown in Figure 4. These ten structures were all optimized at the RHF level to relax the geometries obtained from the MM+ calculations. It should be noted that due to the size of these systems, it is not feasible to obtain a completely optimized structure. The initial and final RHF energies are listed in Table 1. This shows that the structures obtained from MM+ are, on the average, 1 Hartree higher than those calculated from RHF. The lowest energy structure after the optimization is S4-5 (E_{RHF} = -28571.4952 Hartree). This S4-5 structure was the one used to obtain the simulations of ^{13}C NMR and PDF measurements, used to validate the model.

NMR: In order to explore the sensitivity of the simulated ^{13}C NMR spectrum to the structure of the model, calculations of the chemical shielding were completed on structures S4-1 through S4-5 and these calculations were used to simulate the spectra shown in Figure 5. As can be seen in this figure, the spectra obtained from any of these models are very similar, with only slight differences in the aliphatic chemical shift region. This is not unexpected, as nearly all the structural changes in the models are occurring in the flexible aliphatic chains while the aromatic structures are very rigid and fixed.

A comparison can also be made between the spectrum simulated for model S4-5 and an experimental ^{13}C SSNMR spectrum of a Green River kerogen, as shown in Figure 6. The agreement between the simulation and the experimental spectrum is quite good in terms of the agreement of the line shape for both the aliphatic and aromatic regions as

well as in the relative intensities of the two regions. The agreement of the relative intensities is a reflection that the model and the experiment have the same ratios between aromatic and aliphatic (28% aromatic/olefinic/carbonyl for the model and 24% from the experimental NMR). Both the experimental and theory show the same tail to higher chemical shifts, due to the presence of the carbonyl carbons.

PDF: A similar analysis was completed with the atomic pairwise distribution functions in order to obtain a second independent validation of the model. The PDF simulated based on the S4-5 monomer model is shown in Figure 7, along with the decomposition to the pairings between different atom types. The plot shows that the atom-atom correlations are consistent with the separations expected based on typical carbon bond lengths and angles: C–H (1.12 Å), C–C (1.52 Å), ∠ C–C–H (2.18 Å), ∠ C–C–C (2.56 Å), and dihedral C–C–C–C (3.90 Å). The features above 3 Å are a function of the 3D structure and should show sensitivity to changes in the model. A comparison of the PDFs of the structures S4-1 to S4-5 is shown in Figure 8. The plots do not show any significant deviation from each other which indicates that in general the average of various geometrical parameters such as bond lengths, bond angles, and torsional angles are the same for all structures.

To gauge the sensitivity of the PDF analysis to the structural model a stoichiometric equivalent 2D model of the kerogen Siskin model using only aliphatic groups was built and its PDF was generated. As shown in Figure 8, the PDF of the aliphatic model is clearly different from the PDF obtained from the other models in the region above 3 Å. Hence, the PDF approach provides unique plots for different chemical structures and can be used for our analysis.

The ultimate test, of course, is how well the PDF of the models correlate with the experimental PDF. A preliminary comparison of the model and experimental PDFs suggested that both have the same features in the short range region ($r < 3$ Å) but deviates heavily at longer distances. There are two possible reasons for this discrepancy: (1) the model is considerably smaller than the experimental structure and (2) a correction term as discussed in the experimental section which accounts for the shape and size of the model is necessary for comparison with experiment.

To explore the effect of the size of the model, a much larger model was built by confining twelve of the unoptimized Siskin model structures (S1) in a bounding box just large enough to accommodate the model. This last point is crucial as the correction term mentioned in point two above, assumes a totally filled rectangular box with no void spaces. The PDF of the 12-unit kerogen model and the experimental PDF for the Green River kerogen are shown in Figure 10. The PDF of the model is corrected accordingly for size and shape. The first peak in the PDFs corresponds to C-H distances whereas the second corresponds to the C-C distance between directly bonded carbons. This distance is approximately 1.5 Å for aliphatic carbons and 1.4 Å for aromatic ones. The second peak at approximately at 2.5 Å corresponds to the geminal distance between carbons two bonds apart. This distance is approximately 2.4 Å and 2.6 Å for aromatic and aliphatic carbons, respectively. The peak at approximately 3 Å corresponds to the distance between carbons separated by four bonds in a *cis* configuration and the one at approximately 3.8 Å to carbons in a *trans* configuration. For these peaks there is good agreement in terms of peak position. The comparison of the peak intensities does show differences, especially in the intensity of the C-H peak. This does suggest that there may

be a greater proportion of aromatic carbons or heteroatoms in the sample compared to the model, consistent with the results of the elemental analysis discussed earlier.

Conclusion

Several 3D models based on Siskin's 2D model for a Green River kerogen were constructed by the geometry optimization of different conformations provided by simulated annealing techniques. These models were used to obtain simulated PDF plots and ^{13}C NMR spectra which were compared with experimental data obtained on a Green River kerogen sample. This process allowed for the exploration of both the sensitivity of these experimental methods to the 3D structure as well as for the validation of the use of the models for subsequent modeling work.

Using different single unit models, simulations of the expected ^{13}C NMR spectrum were completed. These simulated spectra are all similar, but do show differences in the line shape in the aliphatic region. The comparison between the experimental and simulated spectra is quite good, in terms of the lineshapes of both the aromatic and aliphatic region as well as in the relative signal intensity between the two peaks.

The initial models consisting of a single kerogen unit were not sufficient to mimic the bulk kerogen as can be seen in their respective PDF plots. A larger 12-unit model was therefore constructed in a manner which minimized the amount of "dead" spaces around the corners of our confining box, as the calculation of the PDF is based on a rectangular box with no void spaces around the molecule. Overall there is good agreement between the model and experimental PDFs especially at shorter distances,

however less accurate for distances between 4 Å and 6 Å. For distances above 6 Å the PDF provides very poor resolution and while there is overall agreement between the model and experimental one, this does not provide any apparent structural information.

Acknowledgments: This work is supported by a grant from the U.S. Department of Energy, National Energy Technology Laboratory. Use of the Advanced Photon Source was supported by the U. S. Department of Energy, Office of Science, Office of Basic Energy Sciences, under Contract No. DE-AC02-06CH11357. An allocation of computer time from the Center for High Performance Computing at the University of Utah is acknowledged. A.M.O. acknowledges a beam time award on beam 11-ID-B at the Advanced Photon Source at Argonne National Laboratory. D.R.L. acknowledges support by the Chevron Energy Technology Company through a contract with University of Utah.

References

(1) Vandenbroucke, M.; Largeau, C. Kerogen origin, evolution and structure. *Org. Geochem.* **2007**, *38*, 719.

(2) Rullkötter, J.; Michaelis, W. The structure of kerogen and related materials. A review of recent progress and future trends. *Org Geochem* **1990**, *16*, 829.

(3) Siskin, M.; Katritksy, A. R. Aqueous Organic Chemistry: Geochemical Aspects. In *Composition, Geochemistry and Conversion of Oil Shales*; Snape, C., Ed., Kluwer Academic Publishers: Boston **1995**, p. 313.

(4) Nomura, M.; Artok, L.; Murata, S.; Yamamoto, A.; Hama, A.; Gao, H.; Kidena, K. Structural Evaluation of Zao Zhuang Coal. *Energy Fuels* **1998**, *12*, 512.

(5) van Krevelen, D. W. *Coal: Typology – Chemistry – Physics – Constitution*. Netherlands: Elsevier; **1961**.

(6) Brons, G.; Siskin, M.; Botto, R. I.; Guven, N. Quantitative mineral distribution in Green River and Rundle oil shales. *Energy Fuels* **1989**, *3*, 85.

(7) Siskin, M.; Katritzky, A. R. Reactivity of Organic Compounds in Hot Water: Geochemical and Technological Implications. *Science* **1991**, *254*, 231.

(8) Smith, J. W.; Higby, L. W. Preparation of organic concentrate from Green River oil shale. *Anal. Chem.* **1960**, *32*, 1718.

(9) Reisberg, J. The Beneficiation of Green River Oil Shale by Pelletization. In *Oil Shale, Tar Sands, and Related Materials*; Stauffer, H. C., Ed.; American Chemical Society:Washington, DC, 1981; p. 155.

(10) Ibrahimov, R. A. Bissada, K. K. (Adry) Comparative analysis and geological significance of kerogen isolated using open-system (palynological) versus chemically and volumetrically conservative closed-system methods. *Org. Geochem.* **2010**, *41*, 800.

(11) Vandenbroucke, M. Kerogen: from Types to Models of Chemical Structure. *Oil & Gas Science and Technology-Rev. IFP* **2003**, *58*, 243.

(12) Durand, B; Vandenbroucke, M. As cited in *Kerogen, Insoluble Organic Matter From Rocks*; B. Durand, Ed.; Technip: Paris, 1980; p. 218 and 319.

(13) Siskin, M.; Scouten, C. G.; Rose, K. D.; Aczel, D.; Colgrove, S. G.; Pabst, R. E. Detailed Structural Characterization of the Organic Material in Rundle Ramsay Crossing and Green River Oil Shales. In *Composition, geochemistry and conversion of oil shales*; Snape, C., Ed.; Kluwer Academic: Boston, 1995; p. 143.

(14) Lille, U.; Heinmaa, I.; Pehk, T. Molecular model of Estonian kukersite kerogen evaluated by ^{13}C MAS NMR spectra. *Fuel* **2003**, *82*, 799.

(15) Faulon, J. L.; Vandenbroucke, M.; Drappier, J. M.; Behar, F.; Romero, M. 3D Chemical Model for Geological Macromolecules. *Org. Geochem.* **1990**, *6*, 981

(16) Faulon, J.L. *Prediction, Elucidation, and Molecular Modeling. Algorithms and Applications in Geochemistry*. **1991,** Ph. D. Thesis.

(17) Freund, H.; Walters, C. C.; Kelemen, S. R.; Siskin, M.; Gorbaty, M. L.; Curry, D. J.; Bence, A. E. Predicting oil and gas compositional yields via chemical structure-chemical yield modeling (CS-CYM): Part 1- Concepts and implementation. *Org. Geochem.* **2007**, *38*, 288.

(18) Vandergrift, G. F.; Winans, R. E.; Horwitz, E. P. Quantitative study of the carboxylic acids in Green River oil shale bitumen. *Fuel* **1980**, *59*, 627.

(19) Jeong, K. M.; Patzer II, J. F. Indigenous Mineral Matter Effects in Pyrolysis of Green River Oil Shale. In *Geochemistry and Chemistry of Oil Shales*; Minkis, F. P., McKay, J. F., Ed.; American Chemical Society: Washington DC, 1983; pp. 529 - 542.

(20) Jeong K. M.; Kobylinski, T. P. Organic-Mineral Matter Interactions in Green River Oil Shale. *Prepr. Pap.-Am. Chem. Soc., Div. Fuel Chem.* **1983**, p. 493.

(21) Sheu, E.Y. Self-Association of Asphaltenes; Structure and Molecular Packing. In *Structure and Dynamics of Asphaltenes*; Mullins, O. C.; Sheu, E.Y., Ed.; Plenum Press: New York, 1998; pp.115-144.

(22) Egami, T.; Billinge, S.J. L. *Underneath the Bragg Peaks: Structure Analysis of Complex Materials*; Oxford/Pergamon Press: New York, 2003.

(23) Nield, V.; Keen, D. A. *Diffuse Neutron Scattering from Crystalline Materials*; Oxford/Clarendon Press: Oxford, 2001.

(24) Solum, M. S.; Pugmire, R. J.; Grant, D. M. ^{13}C Solid-State NMR of Argonne Premium Coals. *Energy Fuels* **1989**, *3*, 187-193.

(25) Solum, M. S., Sarofim, A. F., Pugmire, R. J., Fletcher, T. F., Zhang, H. ^{13}C NMR Analysis of Soot Produced from Model Compounds and a Coal. *Energy Fuels* **2001**, 15, 961.

(26) Solid state ^{13}C NMR and PDF measurements were completed on a sample of kerogen isolated following the process outlined by Vandergrift, G. F.; Winans, R. E.; Scott, R. G.; Horwitz, E. P., in Fuel 1980, 59(9), 627, on a one foot section from the peak organic content of the Mahogany zone of a core drilled in the Green River Formation of the Uinta Basin in Utah in spring 2010. The experimental results will be discussed further in a separate publication.

(27) HyperChem(TM) Professional 7, Hypercube, Inc., 1115 NW 4th Street, Gainesville, Florida 32601, USA.

(28) Allinger, N. L. Conformational Analysis 130. MM2. A Hydrocarbon Force Field Utilizing V1 and V2 Torsional Terms. *J. Am. Chem. Soc.*, **1977**, *99*, 8127.

(29) Schmidt, M. W.; Baldridge, K.K.; Boatz, J. A.; Elbert, S. T.; Gordon, M. S.; Jensen, J. J.; Koseki, S.; Matsunaga, N.; Nguyen, K. A.; Su, S.; Windus, T. L.; Dupuis, M.; Montgomery, J. A. General Atomic and Molecular Electronic Structure System. *J. Comput. Chem.* **1993**, *14*, 1347.

(30) Hehre, W.J.; Stewart, R. F.; Pople, J. A. Self-Consistent Molecular Orbital Methods I. Use of Gaussian Expansions of Slater Type Atomic Orbitals. *J. Chem. Phys.* **1969**, *51*, 2657.

(31) Kirkpatrick, S.; Gelatt, C. D.; Vecchi, M. P. Optimization by Simulated Annealing. *Science* **1983**, *220*, 671.

(32) Macrae, C. F.; Bruno, I.J.; Chisholm, J. A.; Edgington, P. R.; McCabe, P.; Pidcock, E.; Rodriguez-Monge, L.; Taylor, R.; van de Streek, J.; Wood, P. A. Mercury CSD 2.0 – new features for the visualization and investigation of crystal structures. *J. Appl. Cryst.* **2008**, *41*, 466.

(33) Adamo, C; Barone, V. Toward reliable density functional methods without adjustable parameters: The PBE0 model. *J. Chem. Phys.*, **1999**, *110*, 6158-69.

(34) Ditchfield, R.; Hehre, W. J.; Pople, J. A. Self-Consistent Molecular Orbital Methods. 9. Extended Gaussian-type basis for molecular-orbital studies of organic molecules. *J. Chem. Phys.*, **1971**, *54*, 724; Hehre, W. J.; Ditchfield, R.; Pople, J. A. Self-Consistent

Molecular Orbital Methods. 12. Further extensions of Gaussian-type basis sets for use in molecular-orbital studies of organic molecules. *J. Chem. Phys.*, **1972**, *56*, 2257.

(35) Gaussian 09, Revision B.01, Frisch, M. J.; Trucks, G. W.; Schlegel, H. B.; Scuseria, G. E.; Robb, M. A.; Cheeseman, J. R.; Scalmani, G.; Barone, V.; Mennucci, B.; Petersson, G. A.; Nakatsuji, H.; Caricato, M.; Li, X.; Hratchian, H. P.; Izmaylov, A. F.; Bloino, J.; Zheng, G.; Sonnenberg, J. L.; Hada, M.; Ehara, M.; Toyota, K.; Fukuda, R.; Hasegawa, J.; Ishida, M.; Nakajima, T.; Honda, Y.; Kitao, O.; Nakai, H.; Vreven, T.; Montgomery, Jr., J. A.; Peralta, J. E.; Ogliaro, F.; Bearpark, M.; Heyd, J. J.; Brothers, E.; Kudin, K. N.; Staroverov, V. N.; Kobayashi, R.; Normand, J.; Raghavachari, K.; Rendell, A.; Burant, J. C.; Iyengar, S. S.; Tomasi, J.; Cossi, M.; Rega, N.; Millam, N. J.; Klene, M.; Knox, J. E.; Cross, J. B.; Bakken, V.; Adamo, C.; Jaramillo, J.; Gomperts, R.; Stratmann, R. E.; Yazyev, O.; Austin, A. J.; Cammi, R.; Pomelli, C.; Ochterski, J. W.; Martin, R. L.; Morokuma, K.; Zakrzewski, V. G.; Voth, G. A.; Salvador, P.; Dannenberg, J. J.; Dapprich, S.; Daniels, A. D.; Farkas, Ö.; Foresman, J. B.; Ortiz, J. V.; Cioslowski, J.; Fox, D. J. Gaussian, Inc., Wallingford CT, 2009.

(36) Jameson, A. K.; Jameson, C. J. Gas-phase ^{13}C chemical shifts in the zero-pressure limit: refinements to the absolute shielding scale for ^{13}C. *Chem. Phys. Lett.* 1987, *134*, 461.

(37) Proffen, T.; Neder, R. B. DISCUS: a program for diffuse scattering and defect-structure simulation. *J. Appl. Crystallogr.* **1997**, *30*, 171.

(38) Neder, R. B.; Korsunskiy, V. I. Structure of nanoparticles from powder diffraction data using the pair distribution function. *J. Phys.: Condens. Matter*, **2005**, *17*, S125.

(39) Hammersley, A. P.; Svensson, S. O.; Hanfland, M.; Fitch, A. N.; Hausermann, D. Two-dimensional Detector Software: From Real Detector to Idealized Image or Two-theta Scan. *High Pressure Research*, **1996**, *14*, 235.

(40) Chupas, P. J.; Chapman, K. W.; Lee, P. L. Applications of an amorphous silicon-based area detector for high-resolution, high-sensitivity and fast time-resolved pair distribution function measurements. *J. Appl. Cryst.*, **2007**, *40*, 463.

(41) Qiu, X.; Thompson, J. W.; Billinge, S. J. L. PDFgetX2: a GUI-driven program to obtain the pair distribution function from X-ray powder diffraction data. *J. Appl. Cryst.*, **2004**, *37*, 678.

(42) Winans, R. E.; Chapman, K.W.; Chupas, P. J.; Seifert, S.; Clemens, A. H.; Calo, J.; Bain, E.; Mathews, J. P.; Narkiewicz, M.R. In situ studies of coal pressurized with CO_2 by small angle and high energy, wide angle X-ray scattering. *Prep. Pap. - Am. Chem. Soc., Div Fuel Chem.*, **2008**, *53(1)*, 283.

(43) Castro-Marcano, F.; Winans, R. E.; Chupas, P.; Chapman, K.; Calo, J. M.; Watson, J. K.; Mathews, J. P. Fine Structure Evaluation of the Pair Distribution Function with Molecular Models of the Argonne Premium Coals. *Energy Fuels* **2012**, *26*, 4336.

(44) Bennett, A. E., Rienstra, C. M., Auger, M., Lakshmi, K. V., Griffin, R. G. Heteronuclear decoupling in rotating solids. *J. Chem. Phys.* **1995**, *103*, 6951.

(45) Kolodziejski, W., Klinowski, J. Kinetics of Cross-Polarization in Solid-State NMR: A Guide for Chemists. *Chem. Rev.* **2002**, *102*, 613.

Table 1: RHF/STO-3G initial and final energies (in Hartree) of the different monomer kerogen models. The S2 to S5 structures were obtained from the simulated annealing procedure on S1. Structures S4-1 through S4-5 were derived from the lowest energy conformer (S4) from the first annealing step.

	Energy (Hartree)	
	Initial Structure	Final Structure
S1	–28569.2846	-28570.5355
S2	–28569.7319	-28570.5929
S3	–28569.6691	-28570.4581
S4	–28570.3721	-28571.1721
S5	–28569.9504	-28570.4481
S4-1	–28569.8771	-28571.4328
S4-2	–28569.8316	-28571.3913
S4-3	–28569.9410	-28571.4887
S4-4	–28569.8622	-28571.4575
S4-5	–28569.9061	-28571.4952

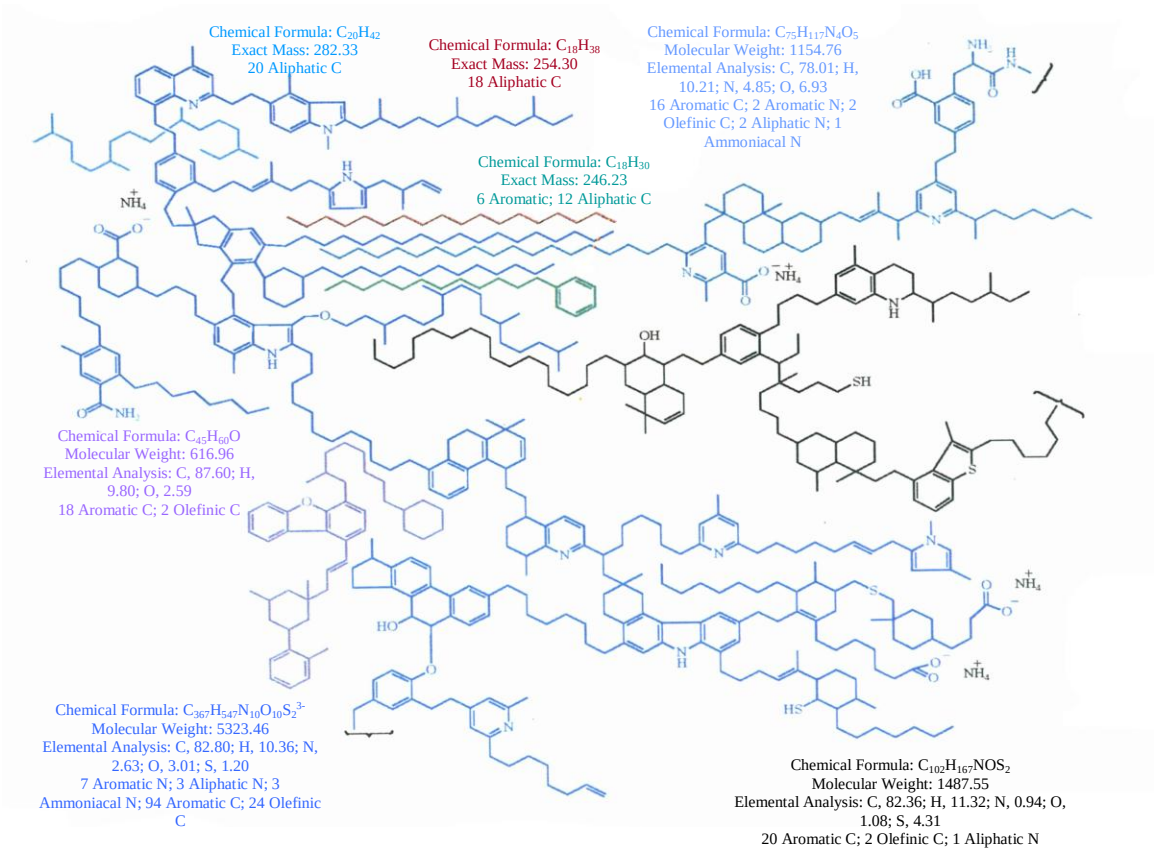

Fig. 1: The 2D Siskin model of Green River kerogen, taken from ref 13.

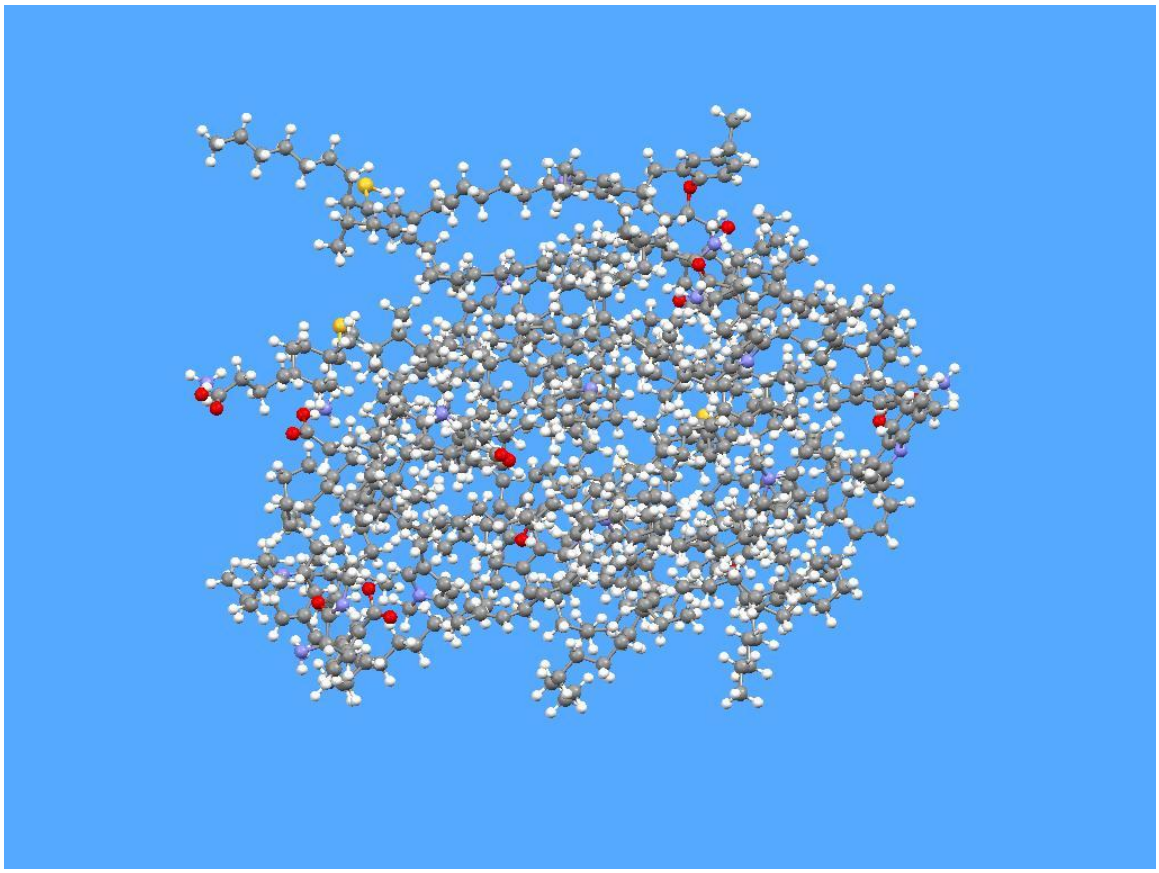

Fig. 2: Initial 3D model (S1) of the Green River kerogen Siskin model (1702 atoms). The atom colors are as follows: C - gray, O - red, N - blue, S - yellow, H - white. The tubes represent the molecule's backbone and the spheres represent the atoms.

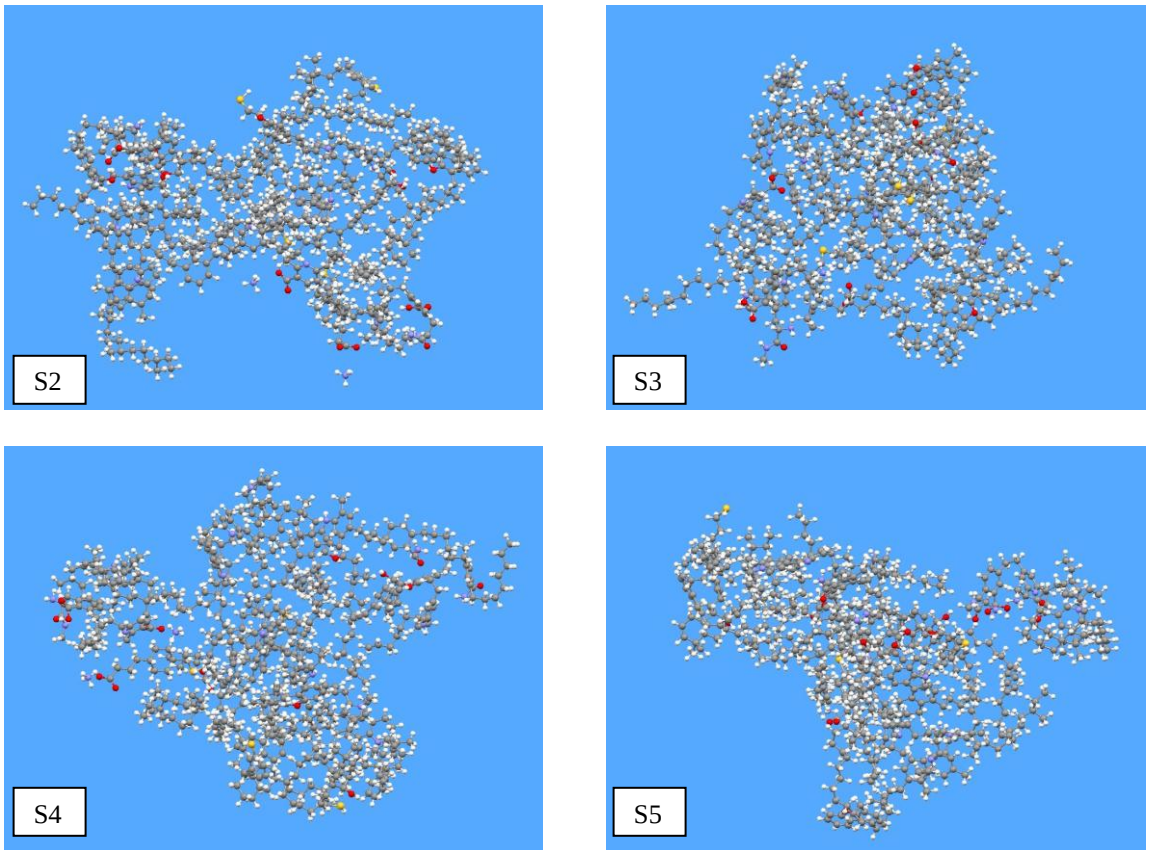

Fig. 3: Local structures generated by applying the simulated annealing procedure described on the initial 3D kerogen model S1. The atom colors and molecule description are the same as in Fig. 2.

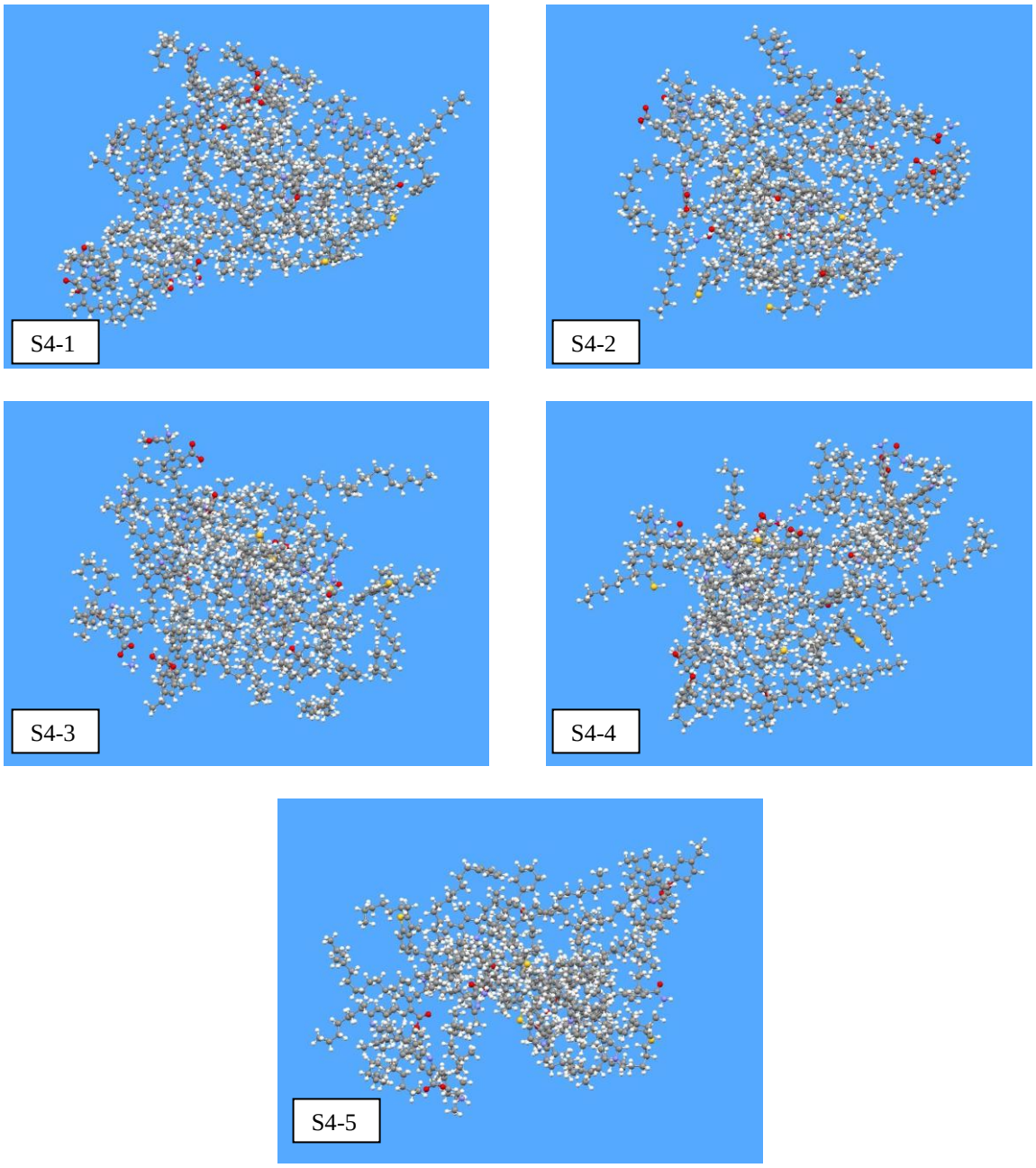

Fig. 4: Local structures generated by subjection kerogen structure S4 to the simulated annealing procedure. The atom colors and molecule description are the same as in Fig. 2.

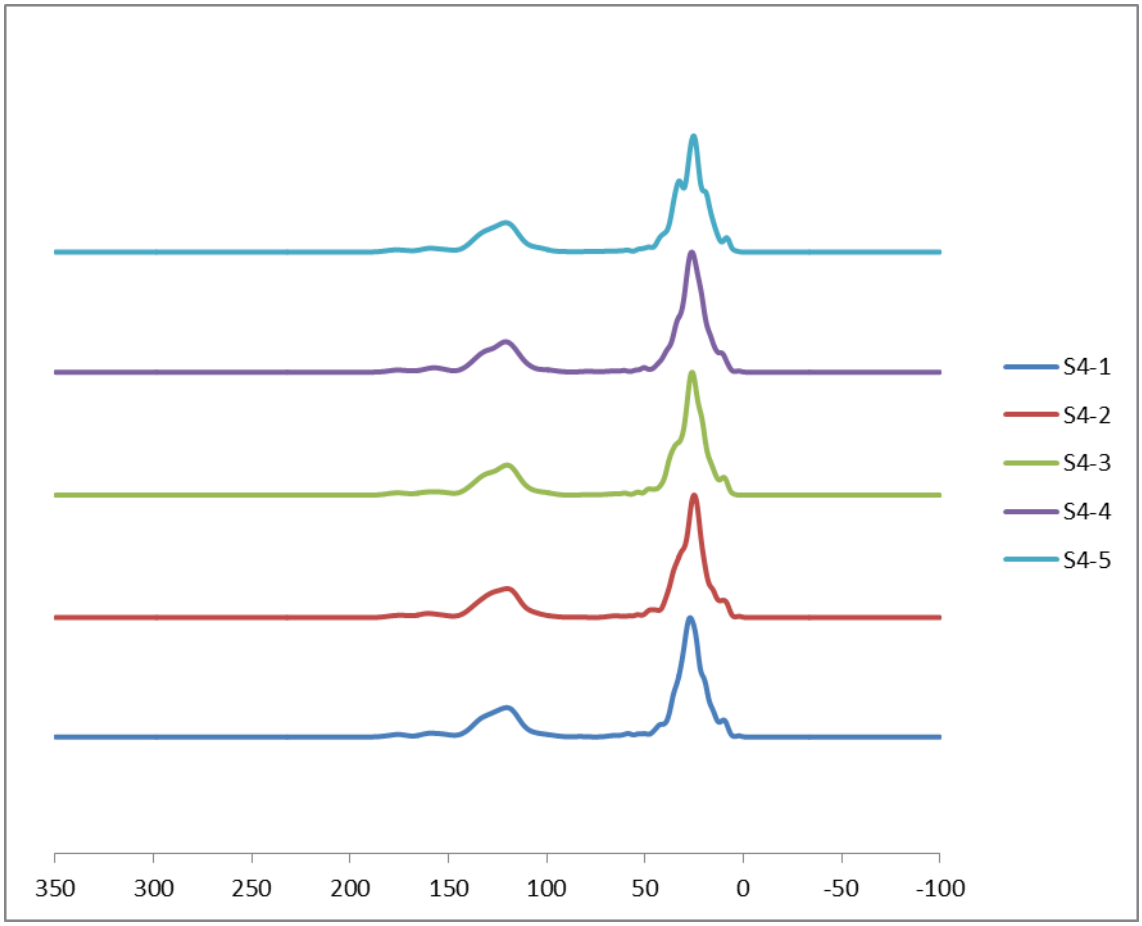

Fig 5: Simulated ^{13}C NMR spectra for models S4-1 thorough S4-5

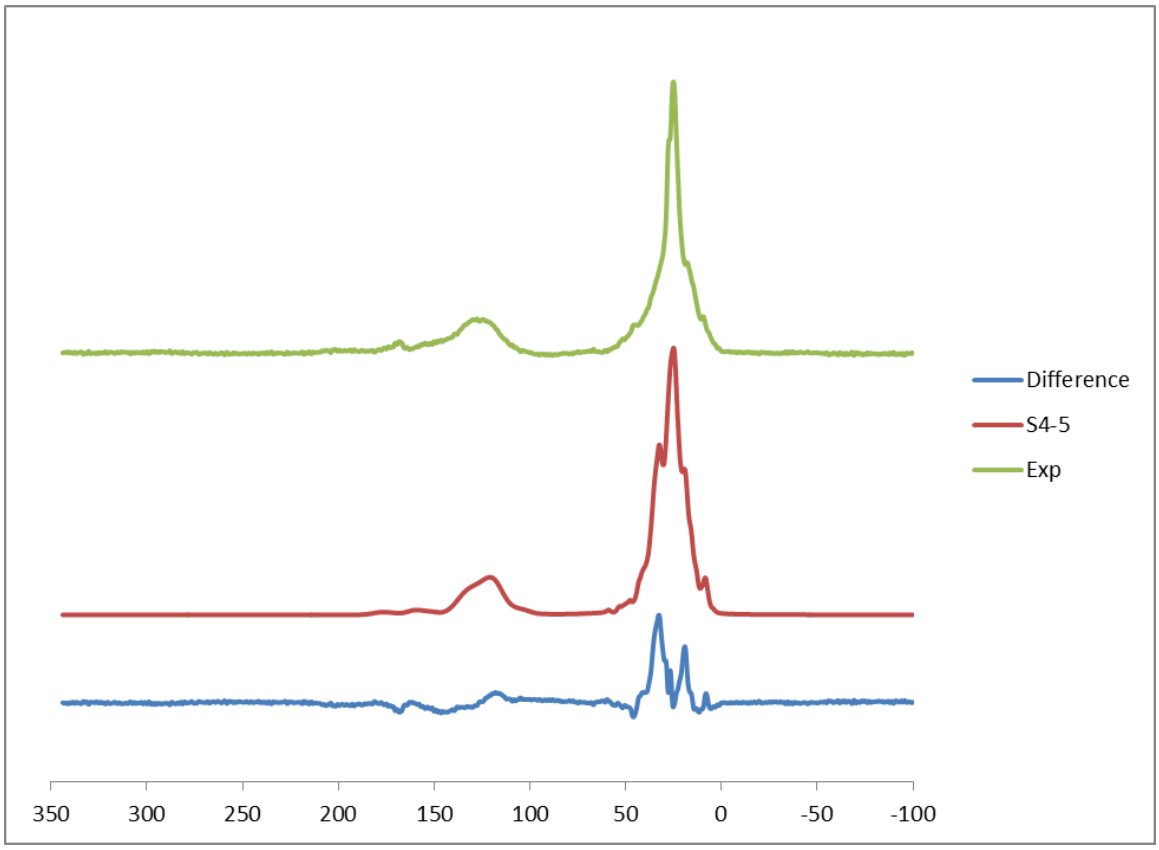

Fig 6: Comparison between simulated ^{13}C NMR spectrum from model S4-5 and the experimental solid state ^{13}C NMR spectrum obtained on a Green River oil shale kerogen. The RMS difference between S4-5 and experimental spectrum is 8 ppm.

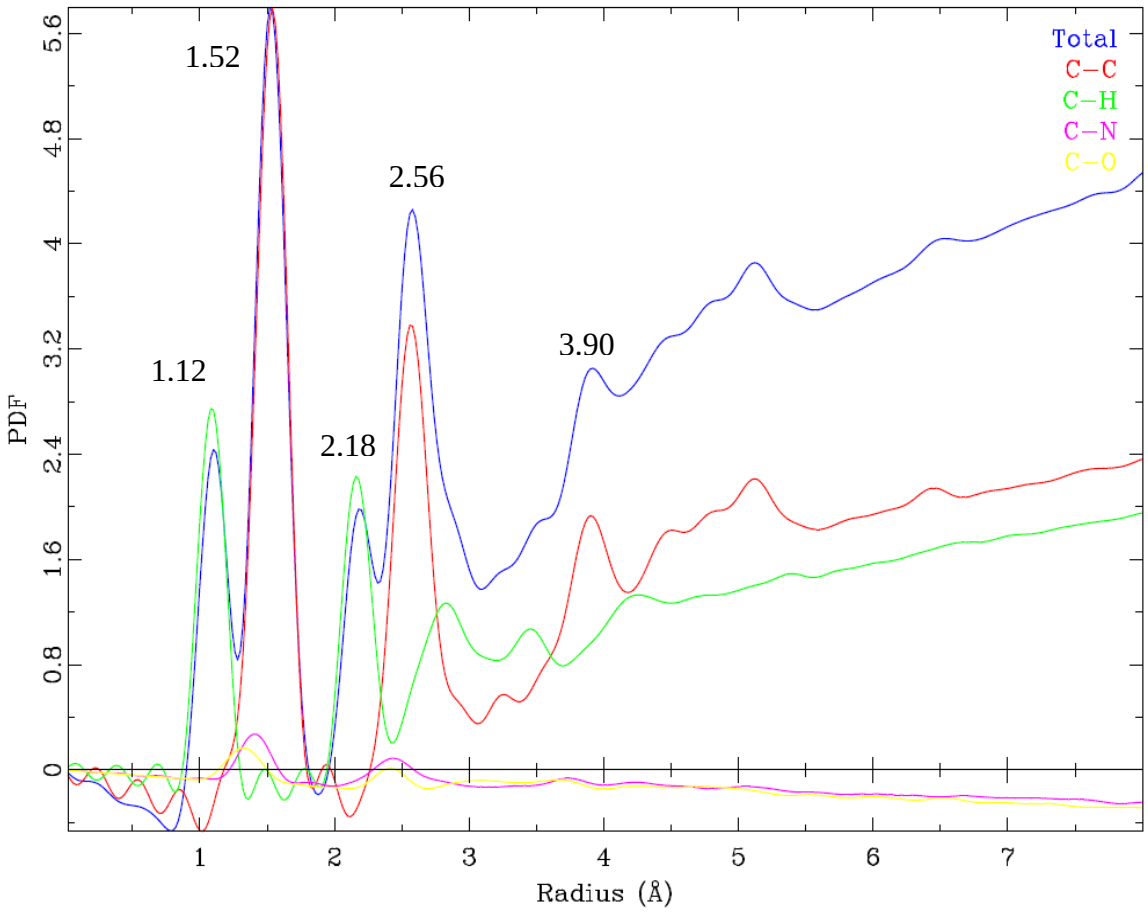

Fig. 7: Pair distribution functions (PDFs) of atom-atom correlations in the kerogen monomer model S4-5. The correlation is decomposed to the contributions from different atomic pairings.

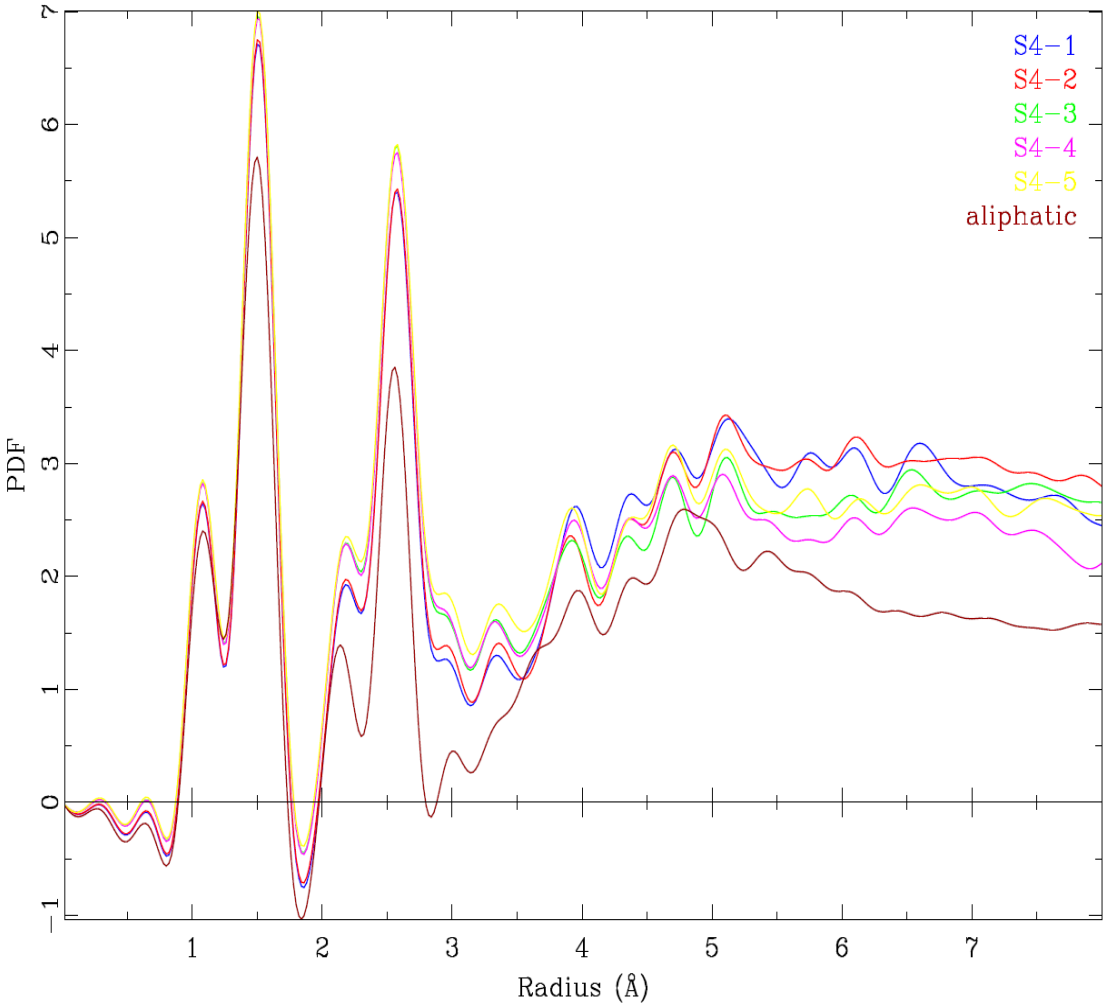

Fig. 8: PDFs of the five monomer conformations of kerogen obtained from the lowest energy structure S4. A stoichiometric equivalent aliphatic structure is included to show that the PDF method is sensitive to variations in the model.

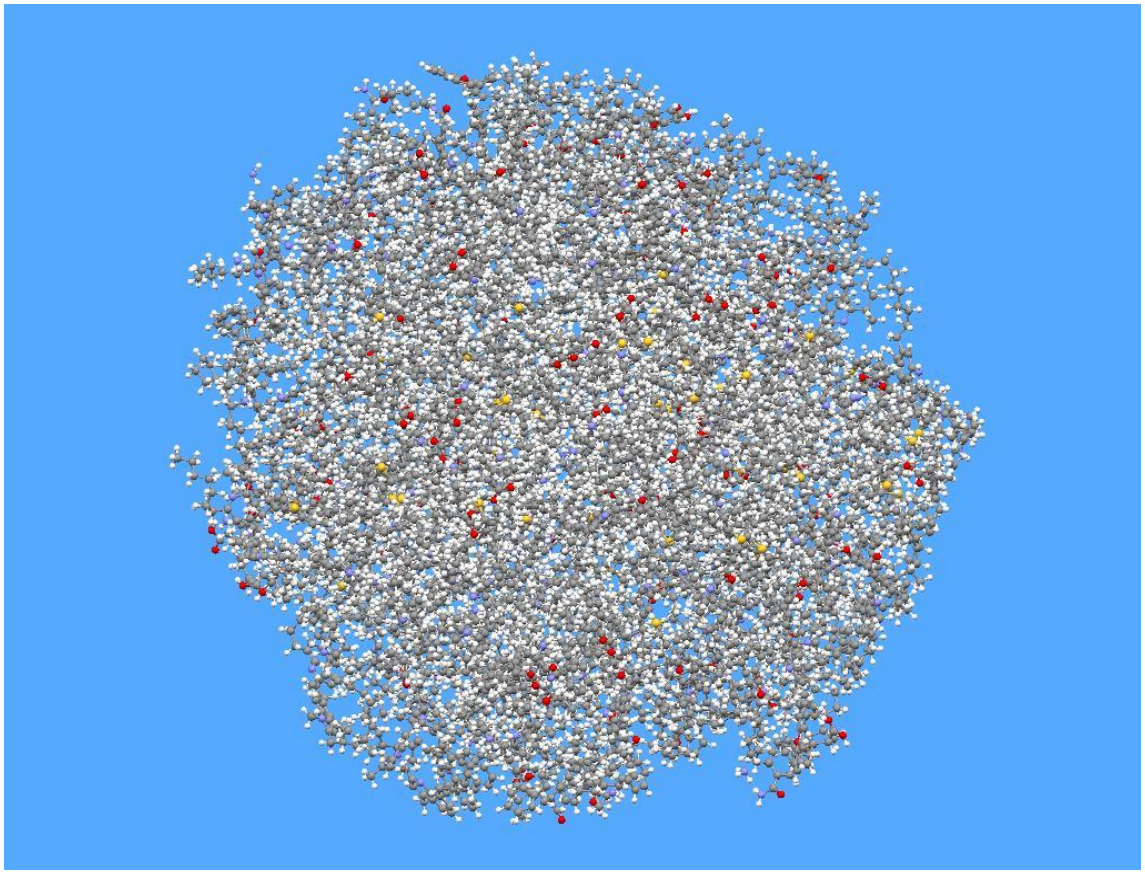

Fig. 9: Three-dimensional structures of the 12-unit kerogen models. The atom colors and molecule description are the same as in Fig. 2.

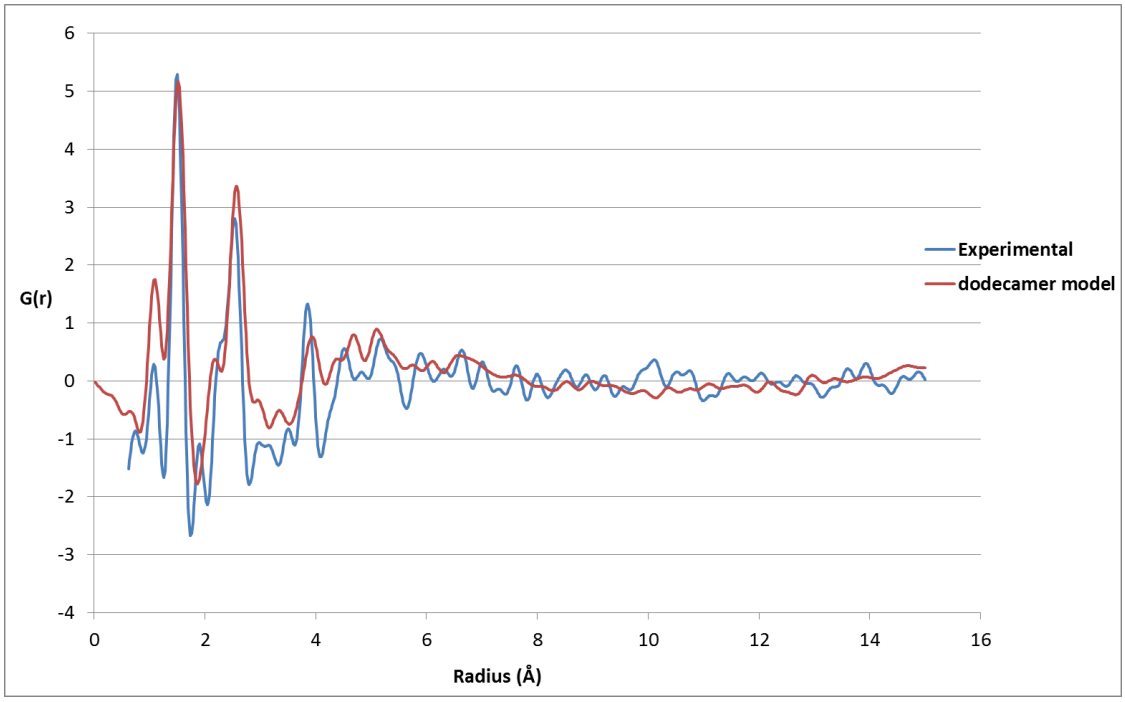

Fig. 10: Comparison of experimentally determined PDF for Green River kerogen and the 12-unit model. The dodecamer model was shape and size corrected using the modified function $-4\pi r\rho_o \tanh(S(R-r))$ with S=0.05 and R=19.3 Å.

National Energy Technology Laboratory

626 Cochrans Mill Road
P.O. Box 10940
Pittsburgh, PA 15236-0940

3610 Collins Ferry Road
P.O. Box 880
Morgantown, WV 26507-0880

13131 Dairy Ashford, Suite 225
Sugarland, TX 77478

1450 Queen Avenue SW
Albany, OR 97321-2198

2175 University Ave. South
Suite 201
Fairbanks, AK 99709

Visit the NETL website at:
www.netl.doe.gov

Customer Service:
1-800-553-7681